UNIVERSITY OF OKLAHOMA

GRADUATE COLLEGE

CORRECTION OF KINEMATIC DATA FROM A SELF-INITIATED PRONE POSITION CRAWLER TRAINER FOR INFANTS WITH CEREBRAL PALSY

A THESIS

SUBMITTED TO THE GRADUATE FACULTY

in partial fulfillment of the requirements for the

Degree of

MASTER OF SCIENCE

By

LEONARD W. WILSON JR.
Norman, Oklahoma
2017

CORRECTION OF KINEMATIC DATA FROM A SELF-INITIATED PRONE PROGRESSION CRAWLER TRAINER FOR INFANTS WITH CEREBRAL PALSY

A THESIS APPROVED FOR THE
STEPHENSON SCHOOL OF BIOMEDICAL ENGINEERING

BY

_____
Dr. Andrew H. Fagg, Chair

_____
Dr. David P. Miller

_____
Dr. Lei Ding

_____
Dr. Thubi H.-A. Kolobe

Acknowledgements

I would like to acknowledge Joshua Southerland who developed the Inertial Measurement Unit (IMU) sensor system used to measure an infant's movements while learning to crawl on the SIPPC assistive robot. In addition, I would like to thank my friend and fellow student, now Dr. Thomas Palmer, for helping me understand some of the MATLAB functions I used in the algorithm to correct for IMU misalignment and drift.

I would like to thank my committee members and principle investigators on the SIPPC project Drs. Andrew Fagg, Thubi Kolobe, David Miller, and Lei Ding for allowing me to work on the project as well as other students on the SIPPC team. In particular I would like to thank my advisor Dr. Andrew Fagg for his guidance in the development of this thesis.

Lastly, I would like to thank my wife, Jana, for her patience and for providing me with emotional support during my time as a biomedical engineering graduate student at the University of Oklahoma.

Table of Contents

List of Tables

List of Figures

Abstract

In recent years small, inexpensive inertial measurement units (IMUs) have been used clinically to monitor human body joint angles in order to assess the progression of, or recovery from, various diseases affecting movement, including Cerebral Palsy, Parkinson's Disease, and stroke. A representation of kinematic movement of a joint can be calculated by changes in the orientations of a pair IMUs placed on a limb above and below the joint. However, errors in the kinematic representation can occur if the IMUs are not correctly aligned with the kinematic model or if the initial position of the joint is not precisely known. In addition, due to the sensitivity of the IMUs to magnetic field distortions caused by nearby metal structures and electrical cables, the sensor coordinate frames can drift over time.

This thesis describes a new approach, the Anatomical Constraint Method (ACM), for reducing the effect of alignment and calibration errors using an algorithm to find a three degree of freedom correction for each IMU that minimizes the average extent to which the calculated joint angles exceed the expected anatomical range of motion. In addition, the algorithm reduces the effect of IMU drift by computing a correction for overlapping time intervals and using spherical linear interpolation to estimate continuous, time-dependent corrections. When the algorithm is applied to data from a network of IMUs designed to track the crawling movement of infants, results show a substantial improvement in the correlation of the kinematic representation of movement with recorded video images.

Chapter 1

1. Introduction

Small, inexpensive IMUs containing three axis gyroscopes, accelerometers, and magnetometers have been used to measure dynamic motion in a number of studies of human biomechanics (Favre, Jolles, Aissaoui, and Aminian, 2008, Cooper, Sheret, McMillian, Silverdis, Ning, Hodgins, Kenney, and Howard, 2009, Bakhshi, Mahoor, and Davidson, 2011, Southerland, 2012, Seel, Raisch, and Schauer, 2014). These studies have been used to determine the movement of individual joints and combinations of joints while performing specific tasks like walking or crawling. In the Self-Initiated Prone Position Crawler (SIPPC) study, IMUs are used to quantify the behavior of four to eight month old infants learning to crawl with and without the use of a robotic crawling assistant (Kolobe, Pidcoe, McEwen, Pollard, and Truesdell., 2007, Kolobe and Fagg, 2014, Kolobe, Fagg, and Ng, 2014, Miller, Fagg, Ding, and Kolobe, 2015). The SIPPC supports the infant in the crawling position and responds to movement of the infant's arms and legs. The study seeks to determine if the use of such a robotic crawling assistant can facilitate prone mobility and help infants with CP learn to crawl.

In order to generate an accurate kinematic representation of an infant's movements, IMUs must be placed on the limbs and torso above and below each joint, and the orientation of the IMUs relative to the joint axes must be known. In addition, prior to the collection of data, the infant's arms, legs, and head must be positioned to match their positions in the initial kinematic representation. However, due to the constraints imposed by working with infants, the IMU axes are not precisely aligned the joint axes

and the calibration of the infant's arms, legs, and head with the starting kinematic representation is often not exact. As a result, the kinematic representation of the infant generated from the uncorrected IMU data often does not reflect the actual movement of the infant.

Various methods of compensating for IMU alignment and calibration errors for individual joints have been proposed (Rivest, 2005, Müller, Bégin, Schauer, and Seel, 2017). The Rivest and Müller et al. methods where designed for the knee and elbow joints, respectively. Both of these methods assume that the range of motion of the joint is restricted to one (for the knee) or two (for the elbow) degrees of freedom. The Rivest method calculates corrections for the IMUs placed on the thigh and calf to bring their axes into alignment with the knee axes. It does this by calculating the corrections that minimize the abduction/adduction and internal/external rotation of the knee when applied to the IMU data. The method proposed by Müller et al. assumes that there should be no abduction/adduction of the elbow and, therefore, no angular acceleration around that axis. They calculate corrections for IMUs placed on the upper arm and forearm to minimize the abduction/adduction angular acceleration. The Rivest and Müller et al. methods are not, however, valid for other joints where there are three degrees of freedom.

The method I propose in this thesis can be applied to all joints and calculates a correction for each IMU that minimizes the extent to which the joint angles exceed expected anatomical joint limits and, optionally, their average distance of from the joint angular centroid derived from several independent trials. This method can, therefore, be

used to correct the joint angular data from a system of IMUs used to produce a kinematic representation of the movement of an entire individual.

IMUs also suffer from drift due to changes in the local magnetic field as the sensor moves in proximity to metal structures or electrical cables. In the SIPPC study, completely isolating the IMUs from magnetic field distortions proved to be impractical because the SIPPC is designed to be portable and was used at different locations during the study. Drift on the order of one to two degrees per second was sometimes present during recording sessions. Various schemes have been used to correct for IMU drift (Djurić-Jovîčić, Jovîčić, Popović, and Djordjević, 2012, Takeda, Lisco, Fujisawa, Gastaldi, Tohyama, and Tadano, 2014, Liu, Inoue, and Shibata, 2009). Most of these methods were used to reduce the effect of senor drift in gait analysis studies and assume that movement of the joints follows a cyclic pattern. Liu et al. used the mid-stance point in a walking gate as a calibration point and Takeda et al. used a low pass Butterworth filter to remove noise from the raw gyroscope data and then utilized the cyclic pattern of walking to remove drift. This involved correcting the joint angle so that the upper and lower flexion/extension limits remained constant over the trial. However, since the movement of an infant's arms and legs while learning to crawl does not always follow a cyclic pattern, these methods were not considered practicable for eliminating drift from the SIPPC data. The method I use involves computing correction rotation matrixes for short overlapping time segments instead of for an entire trial. These correction matrixes are then used to estimate a time-dependent correction using spherical linear interpolation. This technique allows the correction rotation matrix to shift during the trial in response to drift.

In the following chapter, I describe the kinematic sensor network and the procedure used to collect kinematic data from infants using the SIPPC, as well as methods for correction of raw kinematic data developed by others. A detailed description of my algorithm is contained in chapter 3. Chapter 4 shows the results of the algorithm when applied to kinematic data collected from SIPPC trials and chapter 5 contains my conclusion of the effectiveness of the algorithm and possible future work.

Chapter 2

2. Background

2.1. Cerebral Palsy

Cerebral Palsy (CP) is a non-progressive motor neural disorder that affects three in 1000 infants in the United States (Anderson, Doyle, and the Victorian Infant Collaborative Study Group, 2003). As a result of neurological damage, infants with CP often have difficulty learning to crawl due to decreased muscle strength and coordination. Depending on the severity of the condition, this can delay the onset of crawling from an average of seven months for typically developing infants to an average of 13 months for those with CP (Horovitz and Matson, 2011). The delay in the ability to move independently can also delay cognitive and social development by limiting the infant's ability to interact with the environment (Clearfield, 2011, Kermoian and Campos, 1988, Bertenthal and Campos, 1984).

2.2. SIPPC Project Description

The goal of the SIPPC project is to improve the outcomes for children with CP (Kolobe et al., 2007, Kolobe and Fagg, 2014, Kolobe et al., 2015, Miller et al., 2015). The approach is to support the weight of the infant and provide a means of artificial locomotion that is conditioned on the infant's behavior in order to assist the infant in learning to crawl. To evaluate the effectiveness of his approach, both typically developing infants and infants assessed to be at risk of having CP are trained using the SIPPC. Two training sessions are conducted each week, with each session composed of one to three five-minute trials. Infants are in the study from between 12 and 20 weeks or

until they learn to crawl unassisted. Data on the movement of both the infant and the SIPPC are collected electronically during the sessions. Video recordings of the sessions are also made. Developmental progress is assessed using the Movement Observation Coding System (MOCS) (Rule. 2010). MOCS provides a means of determining how the infant is progressing toward crawling by monitoring the development of precursors to crawling like holding the head upright, reaching for an object, and making coordinated movements with the arms and legs.

The MOCS data includes 40 items that are scored on a scale of 0 to 3 by a physical therapist viewing the video recordings. The items assessed include the infant's posture and support (e.g. holding the head upright) during the trial. In addition, the number movements of various types that the child makes with his/her arms and legs (e.g. child extends hip and knee bilaterally causing the foot to push against the floor) are recorded. The ability of the infant to move the SIPPC toward a desired toy and the socio-emotional responses of the child (e.g. the child cries or vocalizes pleasure) are also scored.

2.2.1 SIPPC3 Design

The SIPPC3, shown in Figure 2-1, is the third version of the Self-Initiated Prone Position Crawler (SIPPC). The SIPPC3 consists of a motorized platform suspended from a six-axis force-torque sensor that supports the infant in a prone position. The force-torque sensor measures forces applied by the infant's hands and feet against the ground. The three legs of the SIPPC3 contain linear actuator and Omni-wheel assemblies that allow the platform to move forward, turn left or right, or raise or lower the platform under the control of a central processor. During a trial, the processor

collects and forwards data from the SIPPC3 wirelessly to a laptop computer for display and recording. GoPro® video cameras are mounted to the three SIPPC legs to record movements of the infant's head, legs, and feet during sessions.

The SIPPC3 has three modes of operation. In one mode of operation, forces applied by the infant's arms and legs to the ground cause the SIPPC to move. The movement continues as long as the force is non-zero. In another mode of operation, left, right, or forward movement occurs for a fixed period of time when the applied force or torque crosses a threshold. In the third mode, movement for a fixed period of time is initiated by crawling-like movements of the infant's arms and legs detected by the kinematic sensor suit worn by the infant.

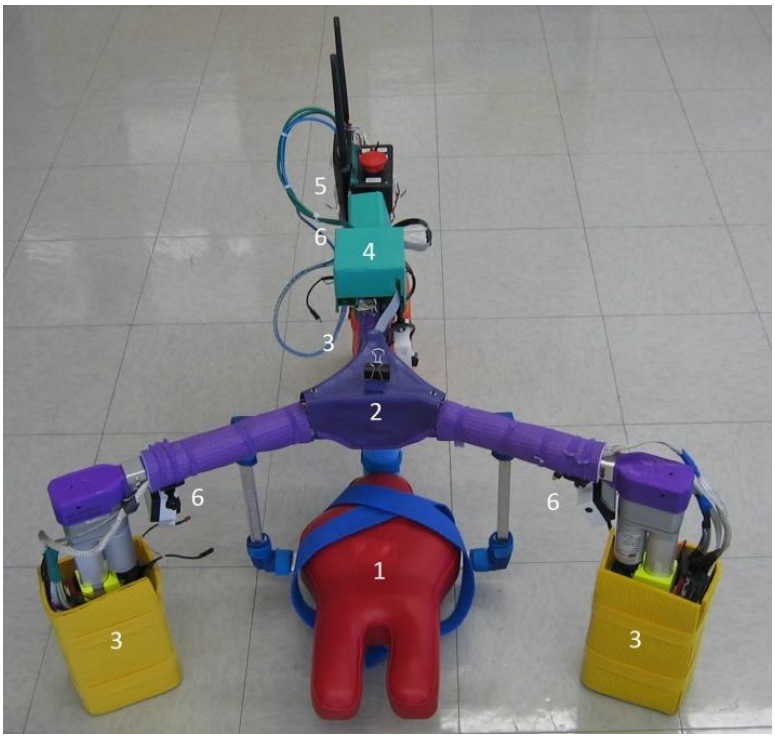

Figure 2-1. SIPPC3 front view showing locations of 1) infant support platform, 2) six-axis force-torque sensor, 3) vertical lift and Omni-wheel assemblies, 4) central processor, 5) wireless modem, and 6) GoPro video cameras.

2.2.2. Kinematic Network

The IMU sensor system used in conjunction with the SIPPC assistive robot consists of twelve (13 when the head sensor is used) CHR-UM6 miniature orientation sensors manufactured by CH Robotics (Southerland, 2012). IMUs are positioned on the lower and upper back, back of the forearms, upper arms, thighs and calves, the soles of the feet, and the back of the head, as shown in Figure 2-3. The sensors are networked to an mBed board containing an ARM7 processor, which polls the sensors at the rate of 50 samples per second. The data is transferred to a laptop computer via Wifi where the orientation data are stored. The IMUs and mBed processor are enclosed in a baby suit, as shown in Figure 2-2, that is secured to the infant's back using Velcro straps during trials.

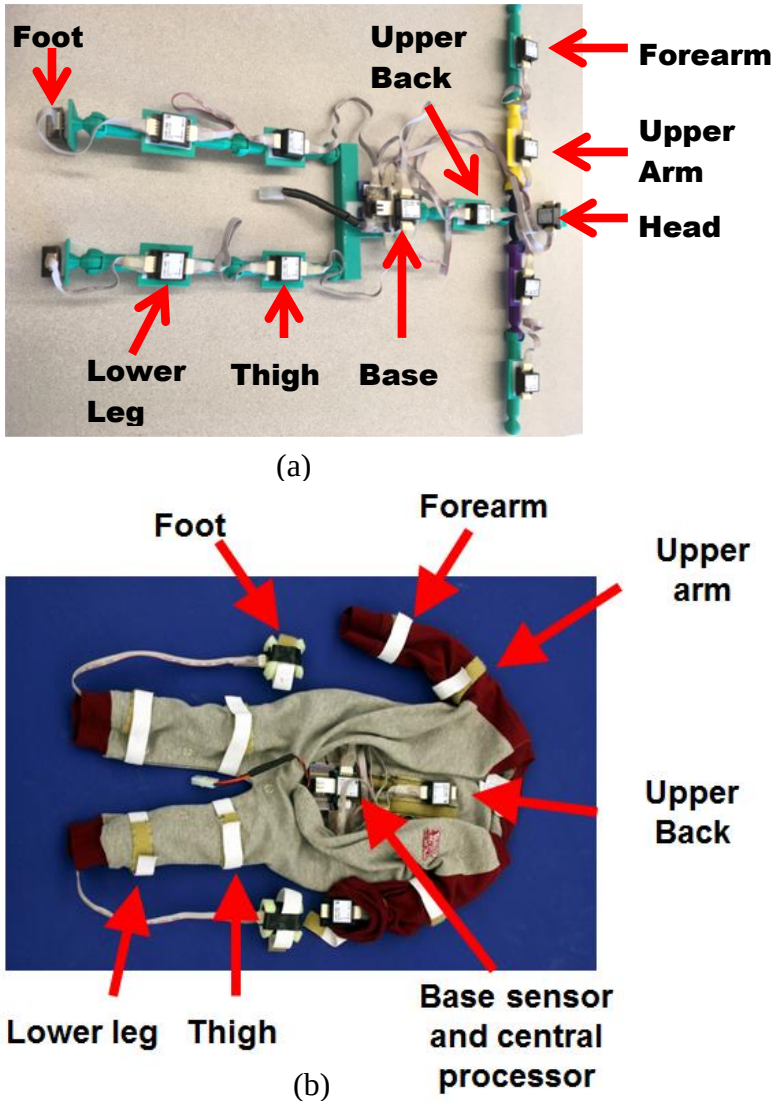

Figure 2-2. Kinematic sensor network (a) on test frame and (b) embedded in a baby suit. The baby suit is attached an infant using Velcro straps during trials.

The kinematic stick figure generated from the sensor data when the sensors are in the calibration configuration of Figure 2-2a is shown in Figure 2-3. This can be constructed from the IMU data if the limb segment lengths are known.

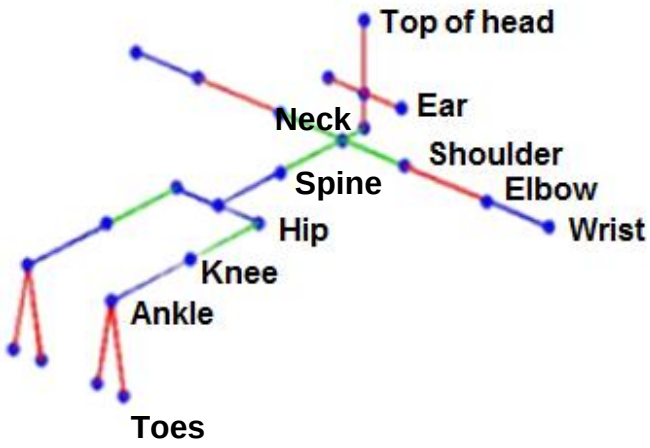

Figure 2-3. Kinematic stick figure of infant in the prone calibration position with head facing forward and arms and legs outstretched.

Although the IMUs measure the orientation of the IMUs the reference coordinate frame may differ from one IMU to another. As a result, infant's arms, legs, and head must be aligned with the calibration configuration of the kinematic stick figure at the start of each trial so that their positions are accurately reflected during the trial. This requires that the head be tilted back so that the IMU sensor on the head is perpendicular with the IMU on the upper back, the arms be fully extended to the infant's sides, with the palms facing the floor, and the legs be straight back with the toes pointed to the floor.

The arms, legs, and head are held in place by a physical therapist or assistant during calibration, but in many cases they are not perfectly aligned with the kinematic figure of Figure 2-3. Figure 2-4 shows typical orientations of the infant's extremities during calibration. In the images, it can be seen that the legs are not held straight back and the head is tilted forward from its position in Figure 2-3.

(a)

(b)

(c)

Figure 2-4. Orientation of the (a) arms, (b) legs, and (c) head during calibration

Because the IMUs attached to the infants arms and legs are embedded in the baby suit and not visible, it is difficult to determine if they are correctly orientated. Since the baby suit is attached by Velcro straps, the IMUs may also shift in position during a session. This is a particular problem for IMUs attached to the upper arm because movements of the arm tend to pull on the suit.

Typical alignment errors for the thigh and calf IMUs are shown in Figure 2-5.

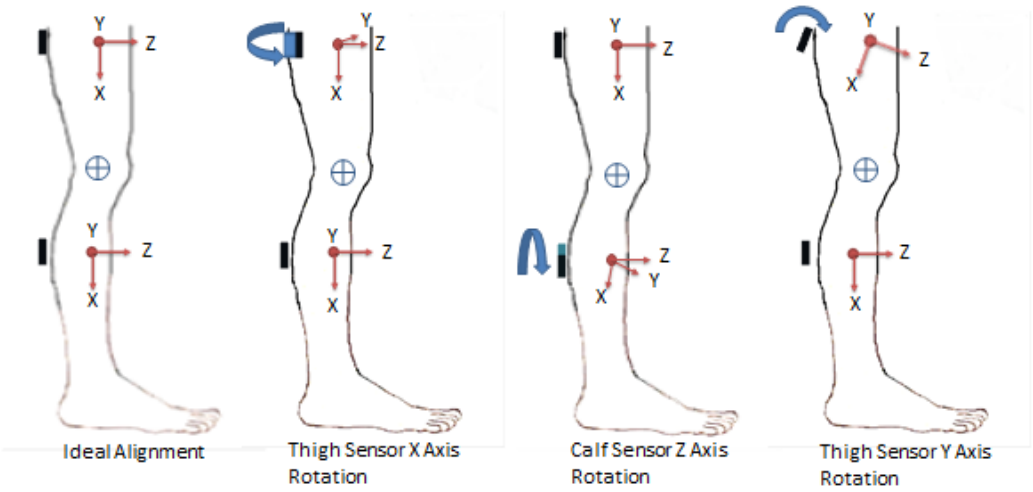

Figure 2-5. Typical IMU alignment errors

Ideally, both the thigh and calf sensors should be aligned with the axes of the knee, but typically, one or both are rotated around the X (lateral/medial rotation), Y (flexion/extension), or Z (abduction/adduction) axis. This is due to the fact the IMUs are inserted into fixed pockets within the baby suit, which both limits their placement on the infant and makes it difficult judge their alignment.

2.3 Joint Angle Calculation.

An IMU consists of three orthogonally orientated gyroscopes, accelerometers, and magnetometers. The magnetometers measure the direction of the magnetic field while the gyroscopes and accelerometers measure acceleration due to movement. These measurements can be used to determine the absolute 3-D orientation of the IMU over time. If IMUs are placed on a limb above and below a joint, aligned with the joint axis, and the initial joint orientation is known, then the joint angles can be calculated using the relationship:

$$R_{Joint} = {}^{IMU1}_{IMU2}R = ({}_{IMU1}^{G}R^{m})^{T}\,{}_{IMU2}^{G}R \tag{2.1}$$

where R_{Joint} is the rotation matrix of the joint and ${}_{IMU2}^{G}R_t$, and ${}_{RMU1}^{G}R_t$ are the rotation matrixes for the IMU sensors in the global coordinate frame. However, in most cases involving the physiological measurement of human joint angles, the initial orientation of the joint at is not precisely known and the sensors, IMU1 and IMU2, are not exactly aligned with the joint axes as illustrated in Figure 2-5.

A number of methods for correcting sensor (or marker for camera based motion capture systems) misalignment with individual joint axes have been proposed (Rivest, 2004, Müller et al., 2017, Luinge, Veltink, and Baten, 2007, Cooper, Sheret, McMillian, Silverdis, Ning, Hodgins, Kenney, and Howard, 2009, Li and Zhang, 2014, Ligorio, Zanotto, Sabatini, and Agrawal, 2017). One approach is to move the joint to its upper and lower limits about all three axes and measure the change in the orientation of the IMUs between those limits. This allows misalignments of the IMU axes relative to the joint axes to be determined. For example, movement of the joint about the X axis should not result in a change in the Y or Z axes of the IMUs if they are correctly aligned

with the joint. This allows a correction for the IMUs to be calculated to place them back into alignment. Alternately, other approaches use a characteristic of the joint. An example of this is the fact that the knee joint has only one axis of rotation, flexion/extension. This allows to a correction to be calculated that minimizes the angular motion about axes in which there should be little or no rotation. Two of these joint angle correction methods are discussed in the following paragraphs.

2.2.3. Rivest's Method for Knee Joint Angle Correction

Rivest's method to correct for misalignment of thigh and calf markers with respect to the knee joint coordinate system assumes that correction rotation matrixes (A and B) can be calculated for the thigh and calf markers to bring then into alignment as illustrated in Figure 2-6 (Rivest, 2005).

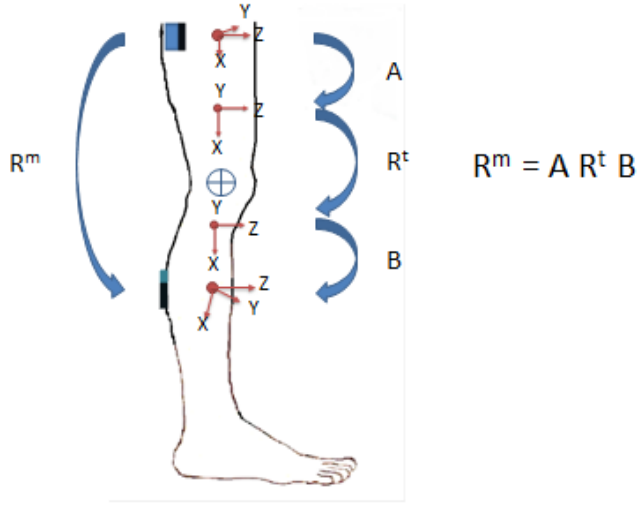

Figure 2-6. Rivest correction for thigh and calf sensor misalignment. R^m and R^t are the measured and true rotation matrixes for the knee. A and B are the correction rotation matrixes for the thigh and calf IMUs required to bring them into alignment with the knee axes.

This method assumes that the knee should have no abduction/adduction or internal/external rotation and the misalignments of the markers are small. With these

assumptions, a closed form solution for A and B can be obtained using a least squares minimization of the abduction/adduction and internal/external rotation angles.

Assuming Z - Y - X rotation, the Euler angles $[\psi, \theta, \phi]$ about the [Z,Y,X] axes may be represented by the rotation matrix, R, where:

$$R = \begin{bmatrix} \cos\psi & -\sin\psi & 0 \\ \sin\psi & \cos\psi & 0 \\ 0 & 0 & 1 \end{bmatrix} \begin{bmatrix} \cos\theta & 0 & \sin\theta \\ 0 & 1 & 0 \\ -\sin\theta & 0 & \cos\theta \end{bmatrix} \begin{bmatrix} 1 & 0 & 0 \\ 0 & \cos\phi & -\sin\phi \\ 0 & \sin\phi & \cos\phi \end{bmatrix}. \quad (2.2)$$

If R^t is the rotation matrix for the knee joint, where θ, ψ, and ϕ are the flexion/extension, abduction/adduction, and internal/external Euler angles, then equation 2.2 may be used to represent the knee joint angles. If ψ and ϕ are very small then $\sin\psi \cong \psi$, $\sin\phi \cong \phi$, $\cos\psi \cong 1$, and $\cos\psi \cong 1$. Substituting these values into equation 2.2 yields:

$$R^t \cong \begin{bmatrix} \cos\theta & -\sin\theta & 0 \\ \sin\theta & \cos\theta & 0 \\ 0 & 0 & 1 \end{bmatrix} \begin{bmatrix} 1 & 0 & \psi \\ 0 & 1 & 0 \\ -\psi & 0 & 1 \end{bmatrix} \begin{bmatrix} 1 & 0 & 0 \\ 0 & 1 & -\phi \\ 0 & \phi & 1 \end{bmatrix} \quad (2.3)$$

$$R^t \cong \begin{bmatrix} \cos\theta & -\sin\theta & \psi\cos\theta + \phi\sin\theta \\ \sin\theta & \cos\theta & \psi\sin\theta - \phi\cos\theta \\ -\psi & \phi & 1 \end{bmatrix}. \quad (2.4)$$

If *A* and *B* are rotation matrices that can correct for the difference between the true, R^t ,and measured, R^m ,systems then:

$$R^m \cong A\ R^t\ B. \quad (2.5)$$

If there is no correction for flexion-extension, θ is 0 and if the correction angles a_1 and a_2 for the abduction/adduction, and internal/external rotation angles (ψ and ϕ) are small then:

$$A \cong \begin{bmatrix} 1 & 0 & 0 \\ 0 & 1 & 0 \\ 0 & 0 & 1 \end{bmatrix} \begin{bmatrix} 1 & 0 & a_1 \\ 0 & 1 & 0 \\ -a_1 & 0 & 1 \end{bmatrix} \begin{bmatrix} 1 & 0 & 0 \\ 0 & 1 & -a_2 \\ 0 & a_2 & 1 \end{bmatrix} = \begin{bmatrix} 1 & a_1 a_2 & a_1 \\ 0 & 1 & -a_2 \\ -a_1 & a_2 & 1 \end{bmatrix}. \quad (2.6)$$

Assuming the product of the two small angles $a_1 a_2$ is approximately 0, then this reduces to:

$$A \cong \begin{bmatrix} 1 & 0 & a_1 \\ 0 & 1 & -a_2 \\ -a_1 & a_2 & 1 \end{bmatrix}. \tag{2.7}$$

Similarly:

$$B \cong \begin{bmatrix} 1 & 0 & b_1 \\ 0 & 1 & -b_2 \\ -b_1 & b_2 & 1 \end{bmatrix}. \tag{2.8}$$

Substituting (2.4), (2.7), and (2.8) into (2.5) yields:

$$\begin{bmatrix} \cos\theta^m & -\sin\theta^m & \psi^m \cos\theta^m + \phi^m \sin\theta^m \\ \sin\theta^m & \cos\theta^m & \psi^m \sin\theta^m - \phi^m \cos\theta^m \\ -\psi^m & \phi^m & 1 \end{bmatrix} \cong \begin{bmatrix} 1 & 0 & a_1 \\ 0 & 1 & -a_2 \\ -a_1 & a_2 & 1 \end{bmatrix}$$

$$\times \begin{bmatrix} \cos\theta^t & -\sin\theta^t & \psi^t \cos\theta^t + \phi^t \sin\theta^t \\ \sin\theta^t & \cos\theta^t & \psi^t \sin\theta^t - \phi^t \cos\theta^t \\ -\psi^t & \phi^t & 1 \end{bmatrix} \times \begin{bmatrix} 1 & 0 & b_1 \\ 0 & 1 & -b_2 \\ -b_1 & b_2 & 1 \end{bmatrix}. \tag{2.9}$$

If the measured flexion-extension, θ^m, is assumed to be the same as the true flexion extension, θ^t, and if, the $\psi \cos\theta + \phi \sin\theta$, and $\psi \sin\theta - \phi \cos\theta$ terms are assumed to be negligible, since ψ and ϕ small, the differences between the measured and true abduction/adduction and internal/external rotation angles can be estimated by:

$$\psi^m - \psi^t \cong b_1 + a_1 \cos\theta^m - a_2 \sin\theta^m \tag{2.10}$$

and

$$\phi^m - \phi^t \cong b_2 + a_1 \cos\theta^m + a_2 \cos\theta^m. \tag{2.11}$$

From these equations, a least squares cost function can be developed to minimize differences between ψ^t and ψ^m and $\phi^t$and ϕ^mover *n* measurements.

$$e = \sum_{i=1}^{n} (\psi_i^m - b_1 - a_1 \cos\theta_i^m + a_2 \sin\theta_i^m)^2 + \sum_{i=1}^{n} (\phi_i^m - b_2 - a_1 \sin\theta_i^m - a_2 \cos\theta_i^m)^2. \quad (2.12)$$

Rivest showed that there is a closed form least squares solution for a_1, a_2, b_1, and b_2 such that:

$$\hat{a}_1 = \frac{1}{n(1-\bar{R}_\theta^2)} \sum_{i=1}^{n} \{(\psi_i^m - \bar{\psi}^m)\cos\theta_i^m + (\phi_i^m - \bar{\phi}^m)\sin\theta_i^m\}, \quad (2.13)$$

$$\hat{a}_2 = \frac{1}{n(1-\bar{R}_\theta^2)} \sum_{i=1}^{n} \{-(\psi_i^m - \bar{\psi}^m)\sin\theta_i^m + (\phi_i^m - \bar{\phi}^m)\cos\theta_i^m\}, \quad (2.14)$$

$$\hat{b}_1 = \bar{\psi}^m - \frac{1}{n} \sum_{i=1}^{n} \{\hat{a}_1 \cos\theta_i^m - \hat{a}_2 \sin\theta_i^m\}, \text{ and} \quad (2.15)$$

$$\hat{b}_2 = \bar{\phi}^m - \frac{1}{n} \sum_{i=1}^{n} \{\hat{a}_1 \sin\theta_i^m + \hat{a}_2 \cos\theta_i^m\}, \quad (2.16)$$

where,

$$\bar{\phi}^m = \sum_{i=1}^{n} \frac{\phi_i^m}{n}, \quad (2.17)$$

$$\bar{\psi}^m = \sum_{i=1}^{n} \frac{\psi_i^m}{n}, \text{ and} \quad (2.18)$$

$$\bar{R}_\theta^2 = \sqrt{\left(\sum_{i=1}^{n} \frac{\cos\phi_i^m}{n}\right)^2 + \left(\sum_{i=1}^{n} \frac{\sin\theta_i^m}{n}\right)^2}. \quad (2.19)$$

The Rivest method has the advantage of not requiring that the initial position of the joint be known. It is also relatively fast computationally, because it offers a closed form solution. It does not, however, correct errors in flexion/extension due to IMU misalignment. It is also only valid for joints in which there is a single axis of rotation and the corrections required to align the IMUs are small.

2.3.2. Müller et al. Method for Elbow Joint Angle Correction

The Müller et al. method was developed to eliminate the requirement that IMUs, placed on the upper arm and forearm to measure the elbow joint angles, be aligned with the elbow joint axes. It assumes that there is no abduction/adduction of the elbow and that it can, therefore, be modeled as a two dimensional joint. If IMUs 1 and 2 are placed on the upper arm and forearm, then angular the velocity, $\omega_{r,k}^{A}$, of the elbow relative to the upper arm IMU is given by:

$$\omega_{r,k}^{A} = -\omega_{IMU1,k}^{A} + \left(R_{A,k}^{B}\right)^{T} \omega_{IMU2,k}^{B}, \tag{2.20}$$

where *A* is the frame of reference for IMU 1, *B* is the frame of reference for IMU2 and $R_{A,k}^{B}$ is a rotation matrix which rotates *B* into *A*. If a^{A} and b^{B} are unit axes of rotation in the *A* and *B* frames of reference and α^{A} and β^{B} are scalers, (2.20) can be expressed as:

$$\omega_{r,k}^{A} = \alpha_k \mathrm{a}^{A} + \left(R_{A,k}^{B}\right)^{T} \beta_k \mathrm{b}^{B} + e_k, \tag{2.21}$$

where e_k is the error given that the true rotation axes of the upper arm and forearm are not precisely known. The normalized error, $e_{n,k}$,with respect to $\omega_{r,k}^{A}$ is:

$$e_{n,k} = \begin{cases} \dfrac{\alpha_k \mathrm{a}^{A} + \left(R_{A,k}^{B}\right)^{T} \beta_k \mathrm{b}^{B} - \omega_{r,k}^{A}}{\left\|\omega_{r,k}^{A}\right\|_2} & if \ \left\|\omega_{r,k}^{A}\right\|_2 > 0 \\ 0 & if \ \left\|\omega_{r,k}^{A}\right\|_2 = 0, \end{cases} \tag{2.22}$$

where $\left\|\omega_{r,k}^{A}\right\|_2$ is the normalized magnitude of $\omega_{r,k}^{A}$.

Given that a^{A} and b^{B} are known and assuming that $a^{A} \neq \pm\left(R_{A,k}^{B}\right)^{T} \mathrm{b}^{B}$, the problem is linear and the Moore-Penrose pseudoinverse can be used to compute a solution that expresses α_k, and β_k in terms of a^{A}, b^{B}, $R_{A,k}^{B}$, and $\omega_{r,k}^{A}$:

$$\alpha_k = \frac{(a^A)^T - (a^A)^T R^B_{A,k} \mathrm{b}^B (\mathrm{b}^B)^T (R^B_{A,k})^T}{1 - (a^A)^T R^B_{A,k} \mathrm{b}^B (\mathrm{b}^B)^T (R^B_{A,k})^T a^A}\ \omega^A_{r,k}, \text{ and} \tag{2.23}$$

$$\beta_k = \frac{\left(R^B_{A,k} \mathrm{b}^B\right)^T - (a^A)^T R^B_{A,k} \mathrm{b}^B (a^A)^T}{1 - (a^A)^T R^B_{A,k} \mathrm{b}^B (\mathrm{b}^B)^T \left(R^B_{A,k}\right)^T a^A}\ \omega^A_{r,k}. \tag{2.24}$$

Given the estimated rotation matrix, $R^B_{A,k}$, a cost function, *J*, for the normalized error for N samples can be expressed in terms of the unit axes $a^A$and b^B

$$J(a^A, \mathrm{b}^B) = \frac{1}{N} \sum_{k=1}^{N} \frac{(e_k)^T e_k}{\left(\omega^A_{r,k}\right)^T \omega^A_{r,k}} \tag{2.25}$$

for $\left\|\omega^A_{r,k}\right\|_2 > 0$.

Since a^A and b^B are unit axes they can be reduced to 4 dimensions. If they are expressed in terms of spherical coordinates, θ and ρ, then the axis estimate can be represented by:

$$\Phi = [\theta_a \ \ \rho_a \ \ \theta_b \ \ \rho_b \ ], \tag{2.26}$$

and the gradient of *J* with respect to Φ by:

$$\frac{\partial J(a^A, \mathrm{b}^B)}{\partial \Phi} = \frac{2}{N} \sum_{k=1}^{N} \frac{e_k^T \frac{\partial}{\partial \Phi} e_k}{\left(\omega^A_{r,k}\right)^T \omega^A_{r,k}}. \tag{2.27}$$

By reinserting (2.21) this becomes:

$$\frac{\partial J(a^A, \mathrm{b}^B)}{\partial \Phi} = \frac{2}{N} \sum_{k=1}^{N} \left(\frac{\partial \alpha_k}{\partial \Phi}\ e_k^T a^A + \alpha_k e_k^T \frac{\partial a^A}{\partial \Phi} + \frac{\partial \beta_k}{\partial \Phi} e_k^T \left(R^B_{A,k}\right)^T \mathrm{b}^B \right.$$

$$\left. + \beta_k e_k^T \left(R^B_{A,k}\right)^T \frac{\partial b^B}{\partial \Phi} \right) \frac{1}{\left(\omega^A_{r,k}\right)^T \omega^A_{r,k}} \tag{2.28}$$

Since the error is perpendicular to the plane of $e_k^T a^A$ and $e_k^T \left(R_{A,k}^B\right)^T \mathrm{b}^B$, the $e_k^T a^A$and $e_k^T R_{A,k}^B \mathrm{b}^B$ terms are zero, and (2.28) becomes:

$$\frac{\partial J(a^A, \mathrm{b}^B)}{\partial \Phi} = -\frac{2}{N} \sum_{k=1}^{N} \frac{\alpha_k e_k^T \frac{\partial a^A}{\partial \Phi} e_k + \beta_k e_k^T \left(R_{A,k}^B\right)^T \frac{\partial a^B}{\partial \Phi}}{\left(\omega_{r,k}^A\right)^T \omega_{r,k}^A}. \tag{2.29}$$

If Φ is represented by the spherical coordinates of (2.29), then the partial derivatives of a^A and b^B are:

$$\frac{\partial a^A}{\partial \theta_a} = \begin{bmatrix} \cos\theta_a \cos\rho_a \\ \cos\theta_a \sin\rho_a \\ -\sin\theta_a \end{bmatrix}, \quad \frac{\partial a^A}{\partial \rho_a} = \begin{bmatrix} -\sin\theta_a \cos\rho_a \\ \sin\theta_a \cos\rho_a \\ 0 \end{bmatrix}, \tag{2.30}$$

$$\frac{\partial b^B}{\partial \theta_b} = \begin{bmatrix} \cos\theta_b \cos\rho_b \\ \cos\theta_b \sin\rho_b \\ -\sin\theta_b \end{bmatrix}, \quad \frac{\partial b^B}{\partial \rho_b} = \begin{bmatrix} -\sin\theta_b \cos\rho_b \\ \sin\theta_b \cos\rho_b \\ 0 \end{bmatrix}, \text{ and} \tag{2.31}$$

$$\frac{\partial a^A}{\partial \theta_b} = \frac{\partial a^A}{\partial \rho_b} = \frac{\partial b^B}{\partial \theta_a} = \frac{\partial b^B}{\partial \rho_a} = 0. \tag{2.32}$$

The joint axes a^A and b^B can be estimated using a gradient descent algorithm by incrementally changing θ_a , ρ_a , θ_b , and ρ_b until a minimum for the cost function of equation 2.25 is reached. The elbow joint angles can then be calculated by inserting the values of a^A, b^B,and $\left(R_{A,k}^B\right)^T$into equations 2.23 and 2.24 to find α_k and β_k and then finding $\omega_{r,k}^A$ using equation 2.21.

The Müller et al. (2017) method can compensate for fairly large misalignments of the IMUs with the joint axes. But it works only for joints where there is no movement in at least one axis of rotation. Since it relies on gradient descent, it is also computationally slower the Rivest method.

Chapter 3

3. Algorithm Development

The Rivest (2004) and Müller et al. (2017). methods work only for joints where freedom of movement is very limited about at least one axis of rotation. The Rivest method also makes the assumption that the misalignments of the IMUs with respect to the joint are small. This makes these methods unsuitable for correcting alignment errors in IMUs placed around some of the joints measured by the SIPPC kinematic suit that have large ranges of motion about all three rotational axes. This necessitates the development of a new method capable of correcting for IMU misalignment about any joint.

3.1. Correction of Alignment and Calibration Errors

The proposed Anatomical Constraint Method (ACM) is designed to be applicable to all joints. It computes corrections for IMU sensors which minimize excursions of joint angles beyond normal anatomical limits. For joints which have a large range of motion in 3-dimensions, it also corrects the IMUs to minimize the differences in the mean orientations of the joints for an individual trial the mean orientations established from many trials.

3.1.1. Basic Anatomical Constraint Method (ACM)

The ACM is somewhat similar to the Rivest and Müller et al. methods in that it utilizes the anatomical constraints of the intervening joint to calculate corrections for the adjoining IMUs. The constraints on joint movement that I use are based on the anatomical limits of joint movement published in Luttgens and Hamilton (1997) and Soucie, Wang, Forsyth, Funk, Demmy, Roach, and Boone (2011). These limits were

modified because, in the SIPPC3 trials, the infant is strapped to a support platform close to the ground that limits flexion of the back and neck and a platform brace between the infant's legs limits abduction of the hips. The modified joint limits are shown Table 4-1. The joint angles are measured with respect to the kinematic figure shown in Figure 2-3.

Table 3-1. Modified Joint Limits from Luttgens and Hamiltion (1997). Joint angles are measured relative to the position of the joints in Figure 2.3

Joint	Movement	Rotation Axis	Upper Limit (deg.)	Lower Limit (deg.)
Back	rotation	X	30	-30
	flexion/extension	Y	10	-30
	lateral bending	Z	35	-35
Neck	rotation	X	75	-75
	flexion/extension	Y	90	0
	lateral bending	Z	60	-60
Shoulder	flexion/extension	X	135	-45
	Internal/external rotation	Y	60	-60
	abduction/adduction	Z	90	-90
Elbow	flexion/extension	X	160	0
	abduction/adduction	Y	5	-5
	pronation/supination	Z	30	-30
Hip	Internal/external rotation	X	40	-50
	flexion/extension	Y	100	-30
	abduction/adduction	Z	50	-20
Knee	lateral/medial rotation	X	5	-5
	flexion/extension	Y	130	0
	abduction/adduction	Z	5	-5
Ankle	lateral/medial rotation	X	20	-30
	dorsiflexion/ plantar flexion	Y	45	-20
	eversion/inversion	Z	10	-10

As in the Rivest method, I assume that there are correction matrixes *A* and *B* for the IMUs placed on a limb above and below a joint such that the relationship between the true and measured joint angle described by equation 2-5 holds. But, if the first IMU is assumed to be correctly aligned with the joint, the relationship can be reduced to:

$$R^t = R^m\, C, \tag{3.1}$$

where *C* is a correction rotation matrix for the second IMU. This relationship is illustrated for the knee in Figure 3-1.

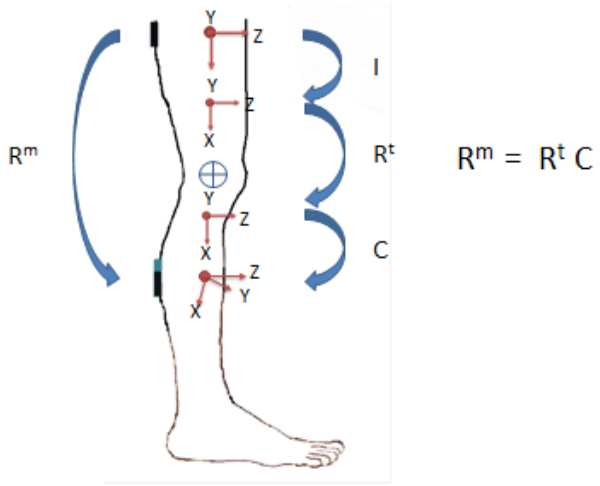

Figure 3-1. Correction for calf sensor misalignment. R^m and R^t are the measured and true rotation matrixes for the knee. I is the identity matrix. C is the correction matrix for the calf sensor.

Figure 3-2 shows the IMU locations on the kinematic figure. IMUs are placed on the base of the spine, upper back, back of the head, back of the upper arms, back of the forearms, back of the thighs, calf, and the bottoms of the feet. Since the infant is strapped to the SIPPC platform, the base IMU has very little movement relative to the SIPPC.

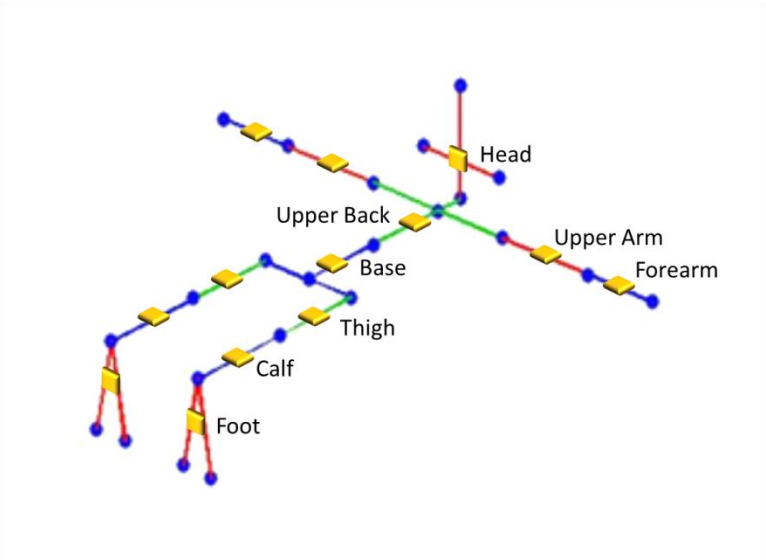

Figure 3-2. IMU positions relative to the kinematic stick figure.

The rotation matrix representation, R, of the IMUs can be calculated from their Z-Y-X orientation using equation 2.2. If the base IMU is assumed to be correctly aligned with the coordinate system of the SIPPC platform, then the corrected orientation of the upper back IMU, ${}_{Upper\ back}^{Base}R^{t}$, can be calculated by:

$$ {}_{Base}^{G}R^{t} = {}_{Base}^{G}R^{m}, \tag{3.2} $$

$$ {}_{Upper\ back}^{Base}R^{m} = ({}_{Base}^{G}R^{m})^{T}\ {}_{Upper\ back}^{G}R^{m}, \tag{3.3} $$

$$ {}_{Upper\ back}^{Base}R^{t} = C_{Upper\ back}\left({}_{Upper\ back}^{Base}R^{m}\right), \text{ and} \tag{3.4} $$

$$ {}_{Upper\ back}^{G}R^{t} = {}_{Base}^{G}R^{t}\left({}_{Upper\ back}^{Base}R^{t}\right), \tag{3.5} $$

where G is the platform frame of reference, ${}_{Upper\ back}^{Base}R^{m}$ is the measured rotation matrix for the spine relative to the base IMU, ${}_{Upper\ back}^{Base}R^{t}$ is the true rotation matrix for the spine, and $C_{Upper\ back}$ is the correction for the upper back IMU.

Knowing ${}_{Upper\ back}^{G}R^{t}$, ${}_{Left\ shoulder}^{G}R^{t}$ can calculated in similar fashion and the process can be extended to IMUs more distal from the base IMU. The general form of equations 3.3 through 3.5 is:

$$ {}_{IMU2}^{IMU1}R^{m} = ({}_{IMU1}^{G}R^{m})^{T}\,{}_{IMU2}^{G}R^{m}, \tag{3.6} $$

$$ {}_{RMU2}^{RMU1}R^{t} = C_{IMU2}({}_{IMU2}^{IMU1}R^{m}), \text{ and} \tag{3.7} $$

$$ {}_{RMU2}^{G}R^{t} = {}_{IMU1}^{G}R^{t}({}_{IMU2}^{IMU1}R^{t}). \tag{3.8} $$

The correction rotation matrix, *C*, is calculated using a gradient descent algorithm that minimizes the cost function $e(C)$. In the basic algorithm this function is:

$$ e(C) = \frac{1}{3n}\sum_{i=1}^{n}(E_{X_i} + E_{Y_i} + E_{Z_i}) + \lambda_1\varphi_C, \tag{3.9} $$

where:

$$ E_X = \begin{cases} X_{R^t} - X_{upper\ limit} & \text{if } X_{R^t} > X_{upper\ limit} \\ X_{lower\ limit} - X_{R^t} & \text{if } X_{R^t} < X_{lower\ limit} \\ 0 & \text{otherwise,} \end{cases} \tag{3.10} $$

$$ E_Y = \begin{cases} Y_{R^t} - Y_{upper\ limit} & \text{if } Y_{R^t} > Y_{upper\ limit} \\ Y_{lower\ limit} - Y_{R^t} & \text{if } Y_{R^t} < Y_{lower\ limit} \\ 0 & \text{otherwise,} \end{cases} \tag{3.11} $$

$$ E_Z = \begin{cases} Z_{R^t} - Z_{upper\ limit} & \text{if } Z_{R^t} > Z_{upper\ limit} \\ Z_{lower\ limit} - Z_{R^t} & \text{if } Z_{R^t} < Z_{lower\ limit} \\ 0 & \text{otherwise.} \end{cases} \tag{3.12} $$

φ_C is the axis angle for the correction, C, such that:

$$ \varphi_C = 2\cos^{-1}(\cos\phi_C \cos\theta_C \cos\psi_C - \sin\phi_C \sin\theta_C \sin\psi_C), \tag{3.13} $$

where ϕ_C, θ_C, and ψ_C are the corrections about the *X*, *Y*, and *Z* axes (Baker, 1999a). The λ_1 regularization coefficient applied to the φ_C term is set to 0.05 to add a small fraction of the angular correction to the cost function so that small angular corrections are favored over large ones. The algorithm iteratively changes the correction angles to

minimize $e(C)$. In essence, this adjusts the IMU_2 axes to minimize the extent to which the averages of the joint angles exceed the anatomical joint limits.

3.1.2. Adjustments to Joint Limits

As seen in Table 3-1, the back, neck, shoulder, and hip joints have non-trivial ranges of motion in all three dimensions. To determine if these ranges are reasonable for infants being tested on the SIPPC3, I analyzed data from 16 trials for different infants, where there was no obvious drift in the raw kinematic data. Data from the first 30 seconds of each five minute trial were combined to produce the joint angle histograms shown in Figures 3-3 through 3-6. These histograms show the distribution of joint angles (blue) around each of the three axis of rotation. The upper and lower joint limits from Table 3-1 are indicated by black vertical dashed limes. The mean angle is of rotation is indicated by a grey vertical dashed line. The red vertical dashed lines show the joint angles that enclose the 90% of the samples on either side of the mean with joint angles closest to the mean.

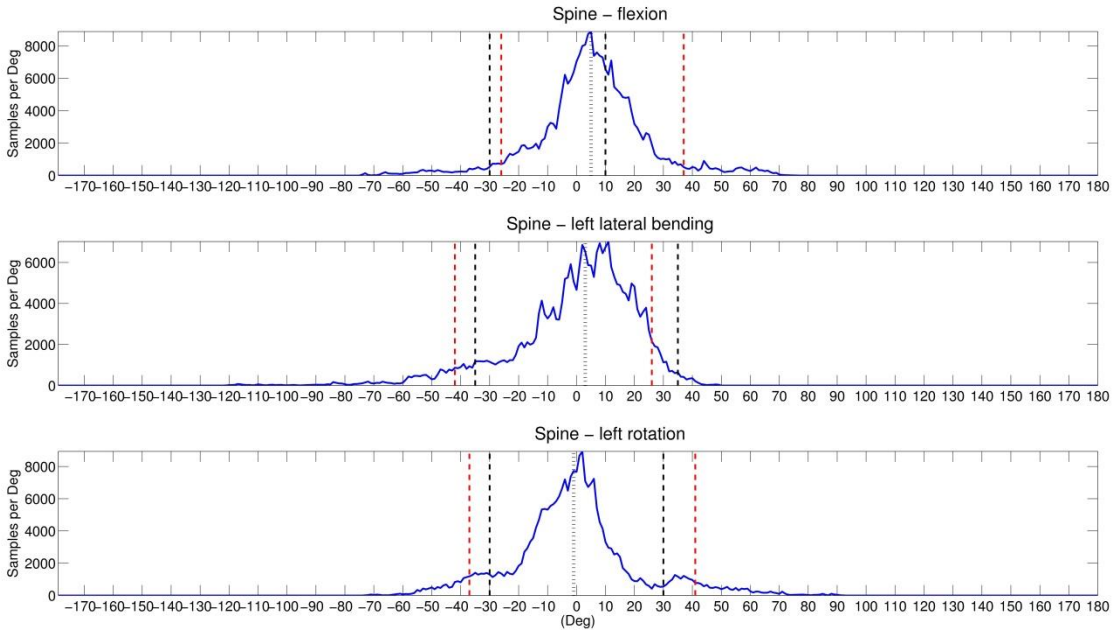

Figure 3-3. Histogram of spine joint angles from the first 30 seconds of 16 trials. Black vertical dashed lines are original joint limits from Table 3-1. Grey dashed line is sample mean. Red vertical dashed lines enclose 90% of samples above and below the mean. Sample bin size is 1 degree.

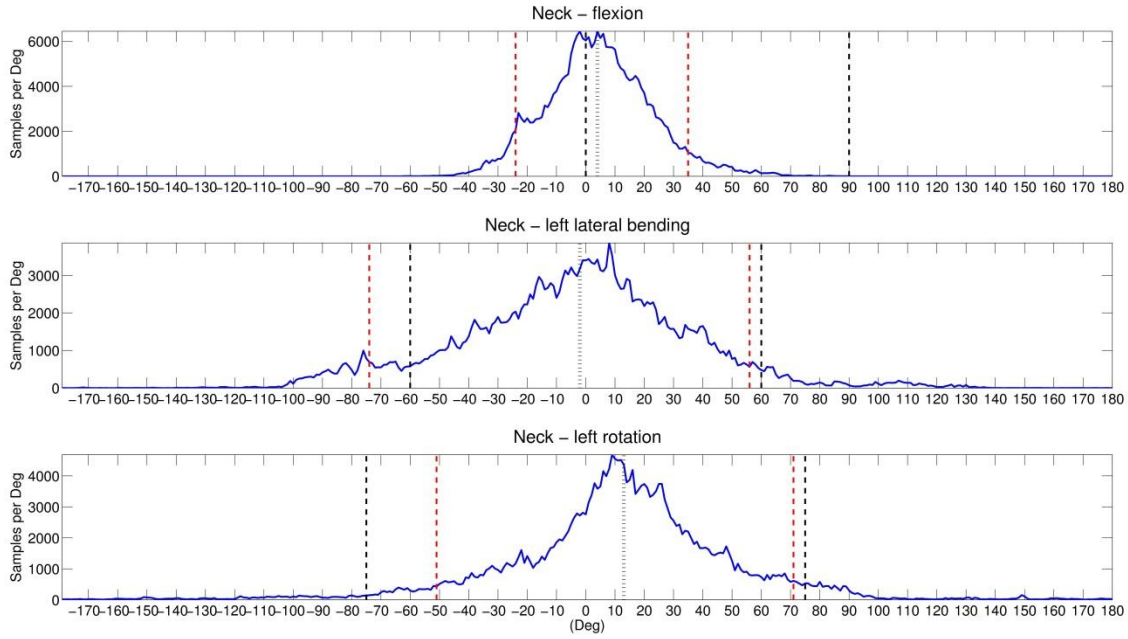

Figure 3-4. Histogram of neck joint angles from the first 30 seconds of 16 trials. Black vertical dashed lines are original joint limits from Table 3-1. Grey dashed line is sample mean. Red vertical dashed lines enclose 90% of samples above and below the mean. Sample bin size is 1 degree.

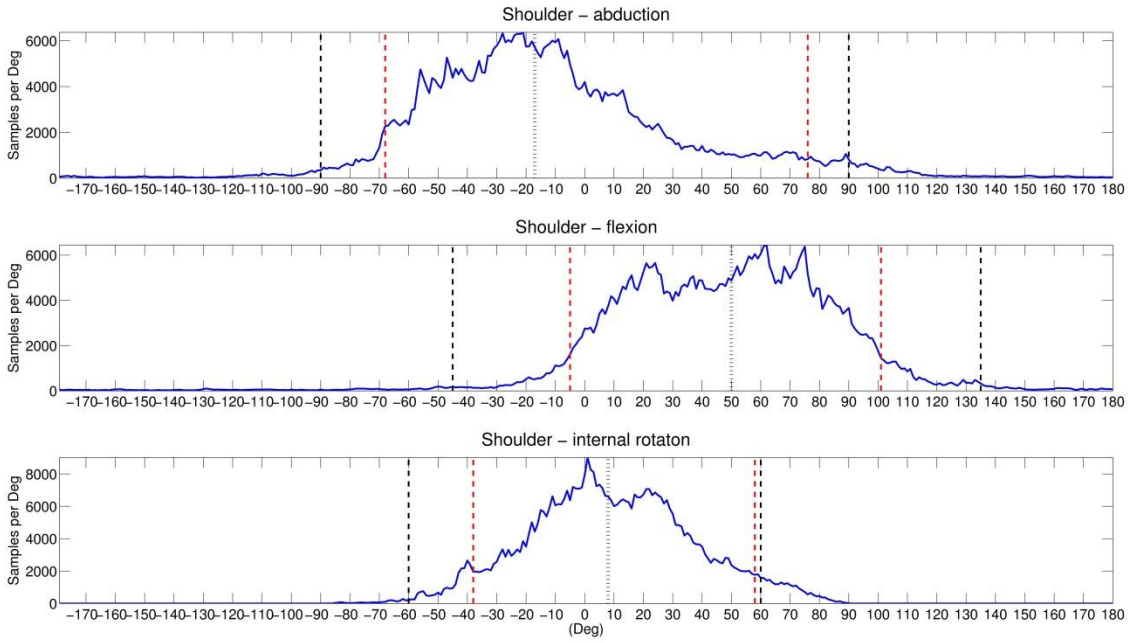

Figure 3-5. Histogram of combined left and right shoulder joint angles from the first 30 seconds of 16 trials. Black vertical dashed lines are original joint limits from Table 3-1. Grey dashed line is sample mean. Red vertical dashed lines enclose 90% of samples above and below the mean. Sample bin size is 1 degree.

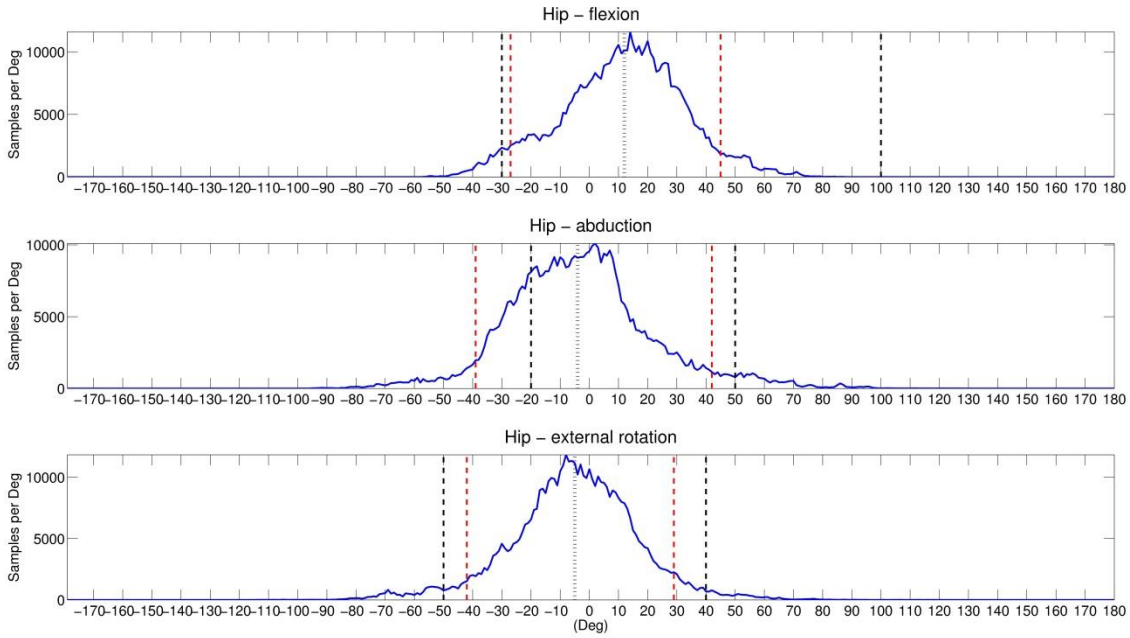

Figure 3-6. Histogram of combined left and right hip joint angles from the first 30 seconds of 16 trials. Black vertical dashed lines are original joint limits from Table 3-1. Grey dashed line is sample mean. Red vertical dashed lines enclose 90% of samples above and below the mean. Sample bin size is 1 degree.

Figures 3-3 through 3-6 show that the average ranges of motion exhibited by the infants during the trials are at variance with the limits specified in Table 3-1 for some of the back, neck, shoulder and hip joint angles. The upper limit for flexion of the spine is about 35 degrees rather than the expected 10 degrees. Flexion of the shoulder in both the positive and negative directions is considerably less than listed in Table 3-1. The upper limit of hip flexion is much less that the 100 degrees of Table 3-1. Finally, the lower limit for flexion of the head is about -30 degrees instead of the expected 0 degrees. This means that the flexion angle of the head IMU relative to the upper back IMU during calibration is closer to 60 degrees than the 90 degree angle shown in Figure 3-2. As a result of these measurements, the joint limits for the back, neck, shoulders and hips were adjusted as shown in Table 3-2.

Table 3-2. Adjusted Joint Limits

Joint	Movement	Rotation Axis	Upper Limit (deg)	Lower Limit (deg)
Back	rotation	X	30	-30
	flexion/extension	Y	30	-25
	lateral bending	Z	35	-35
Neck	rotation	X	75	-75
	flexion/extension	Y	50	-30
	lateral bending	Z	60	-60
Shoulder	flexion/extension	X	100	-10
	Internal/external rotation	Y	60	-40
	abduction/adduction	Z	70	-70
Elbow	flexion/extension	X	160	0
	abduction/adduction	Y	5	-5
	pronation/supination	Z	30	-30
Hip	Internal/external rotation	X	40	-50
	flexion/extension	Y	100	-30
	abduction/adduction	Z	50	-20
Knee	lateral/medial rotation	X	5	-5
	flexion/extension	Y	130	0
	abduction/adduction	Z	5	-5
Ankle	lateral/medial rotation	X	20	-30
	dorsiflexion/ plantar flexion	Y	45	-20
	eversion/inversion	Z	10	-10

3.2. Correction of Sensor Drift

Sensor drift was apparent in more than 20% of the kinematic data collected from the SIPPC3 trials. Sensor drift manifests itself as a slow shift in the positions of the infant's arms, legs, head, and/or back during a trial, unrelated to the movements of the infant. This was found to be caused magnetic field distortions affecting the IMUs' magnetometers when the SIPPC was in the proximity of metal structures and power cables. These magnetic field distortions typically resulted in a slow drift (of less than 2 degrees per second) about one or more axes of rotation of one or more IMUs. An example of sensor drift about the abduction/adduction axis of the left hip is shown in Figure 3-7.

To correct for sensor drift, I calculate correction rotation matrixes for 1 minute segments with 30 second overlaps instead over the entire trial to produce a series of correction rotation matrixes, $\{C_1 \cdots C_n\}$. I then convert this correction series to quaternions, $\{q_1 \cdots q_n\}$, and generate a time dependent correction using spherical linear interpolation (Slerp) (Shoemake, 1985):

$$q_t = \begin{cases} q_1 & \text{if } t < 30\,sec \\ Slerp\,(q_{n-1}, q_n, t') & \text{if } 30\,\text{sec} > t > T - 30\,sec \\ q_{n-1} & \text{if } t > T - 30\,sec\ , \end{cases} \tag{3.14}$$

where t is the time in seconds, T is the trial length in seconds, q_t is the correction in quaternion form at time t, q_n is the correction quaternion calculated for segment n, and t' is the time between q_{n-1} and q_n such that $n = \left\lceil \frac{t}{30} \right\rceil$, and $t' = \frac{t-30(n-1)}{30}$.

The quaternion correction, q_t, is then converted back to rotation matrix format, C_t. The Slerp function is defined by:

$$Slerp(q_{n-1}, q_n, t') = \frac{\sin[(1-t')\Omega]}{\sin\Omega} q_{n-1} + \frac{\sin[\Omega t']}{\sin\Omega} q_n, \tag{3.15}$$

where Ω is the angle subtended by an arc such that $\cos\Omega = (q_{n-1})^T q_n$. If q_{n-1} and q_n are very close, linear interpolation is used.

Figure 3-7 illustrates the process (in one dimension) for drift in the left thigh IMU sensor affecting the hip abduction angle, ψ. In this example a 300 second trial is subdivided into nine 60-second segments which overlap by 30 seconds. For each of these segments a correction matrix, C_n, is calculated using the basic ACM described in section 3.1. For the first and last 30 seconds of the trial, the corrections used are those calculated for the first and last segments respectively. For the rest of the trial the applied

correction is a value obtained by interpolating between the previous and next segment's correction matrixes.

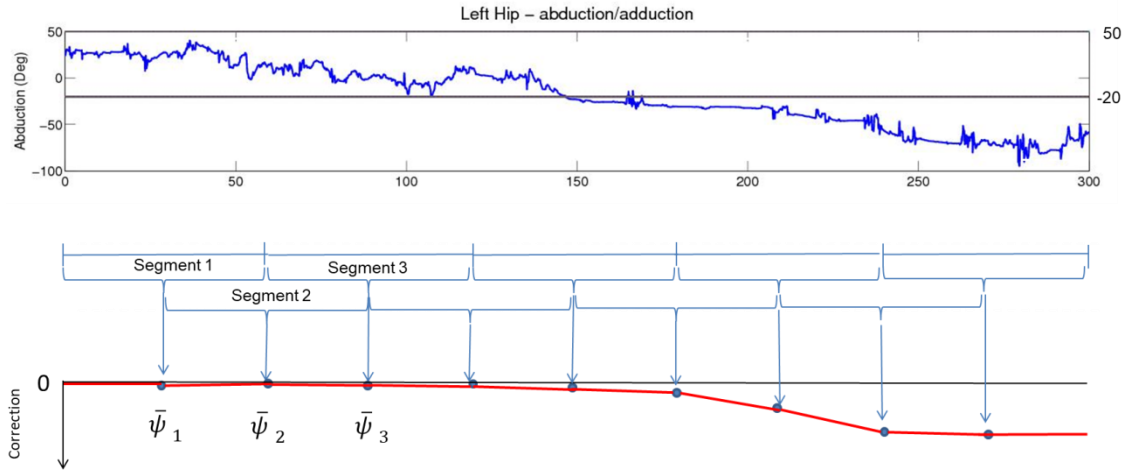

Figure 3-7. Correction for sensor drift. Upper panel shows uncorrected abduction/adduction of left hip. Lower panel shows applied correction (red line).

This method acts like a high pass filter and is effective as long as the drift rate is low.

3.3. Average Centroid Correction

For complex joints with a large range of motion about all three axes like the back, neck, shoulder, and hip, the ACM approach is too ill-constrained to compensate for sensor misalignment if the majority of the uncorrected joint movements are within the anatomical joint limits. In order to address this issue, I added an additional term to the cost function of equation 3-9 to adjust the joint angles toward the average angular centroids. This term minimizes the least squares distance of the mean of the joint angles from the average centroid of the joint angles for multiple trials. With the addition of this term, the cost function becomes:

$$e(C) = \frac{1}{3n}\sum_{i=1}^{n}(E_{X_i} + E_{Y_i} + E_{Z_i}), + \lambda_2 RMSq_i) + \ + \lambda_1 \varphi_C, \tag{3.16}$$

where:

$$RMSq_i = \sqrt{\left(q_{0_i} - q_{c0}\right)^2 + \left(q_{1_i} - q_{c1}\right)^2 + \left(q_{2_i} - q_{c2}\right)^2 + \left(q_{3_i} - q_{c3}\right)^2}, \tag{3.17}$$

and q and q_c are the quaternions for the joint angle and centroid angle respectively, and are related to the joint angles ϕ, θ, and ψ about the X , Y, and Z axes by:

$$q_0 = \cos\frac{\phi}{2}\cos\frac{\theta}{2}\cos\frac{\psi}{2} + \sin\frac{\phi}{2}\sin\frac{\theta}{2}\sin\frac{\psi}{2}, \tag{3.18}$$

$$q_1 = \sin\frac{\phi}{2}\cos\frac{\theta}{2}\cos\frac{\psi}{2} - \cos\frac{\phi}{2}\sin\frac{\theta}{2}\sin\frac{\psi}{2}, \tag{3.19}$$

$$q_2 = \cos\frac{\phi}{2}\sin\frac{\theta}{2}\cos\frac{\psi}{2} + \sin\frac{\phi}{2}\cos\frac{\theta}{2}\sin\frac{\psi}{2}, \text{and} \tag{3.20}$$

$$q_3 = \cos\frac{\phi}{2}\cos\frac{\theta}{2}\sin\frac{\psi}{2} - \sin\frac{\phi}{2}\sin\frac{\theta}{2}\cos\frac{\psi}{2} \tag{3.22}$$

(Baker, 1999b). A regularization coefficient, λ_2, is used to adjust the amount of correction produced by the $RMSq_i$ term relative to the correction produced by the average magnitude of excursions beyond the anatomical limits. The best value for λ_2 was found, experimentally, to be 30 for the spine, neck, shoulder and hip joints and 0 for the elbow, knee, and ankle joints.

To determine the centroid values I computed the mean joint angles from the first 30 seconds of 10 trials that had little apparent drift and a small number of samples that exceeded joint limits. These values are shown in Table 3-3.

Table 3-3. Average Angular Centroid

Joint	Movement	Rotation Axis	Mean (deg)
Back	left rotation	X	0
	flexion	Y	5
	left lateral bending	Z	0
Neck	left rotation	X	0
	flexion	Y	5
	left lateral bending	Z	0
Shoulder	flexion	X	47
	external rotation	Y	-1
	abduction	Z	-31
Hip	external rotation	X	-5
	flexion	Y	12
	abduction	Z	-5

I considered that the joint limits might not be independent and that the distribution of joint angles might not be symmetric about the centroid. For example, the amount of flexion of the shoulder affects the abduction/adduction limits (Engin and Chen, 1989). To investigate this, I produced 3-D scatter plots of the uncorrected joint angles from the spine, neck, shoulders, and hips from the first 30 seconds of ten trials. Figure 3-8 shows the scatter plot for the shoulder.

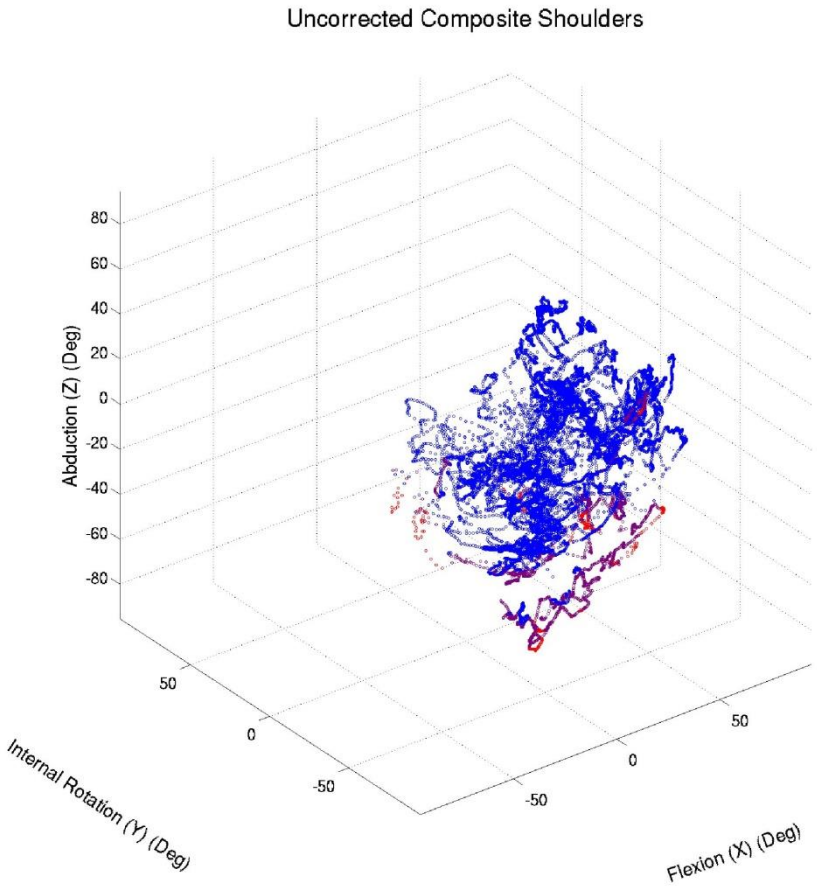

Figure 3-8. Composite 3-D scatter plot of shoulder joint angles. Blue points are within joint limits, purple are within 10 degrees of limits, and red exceed one or more limits by more than 10 degrees.

I found the distributions were approximately spherical in shape around the centroids for the spine, neck, shoulders, and hips. This symmetry about the mean can also be seen in the histograms of Figures 3-3 through 3-6. This does not imply that the joint limits are independent, but since the distributions are symmetric, minimizing the root mean square distance of the samples to the average centroid should work in most cases to minimize the alignment error.

3.4. Algorithm Implementation

Corrected rotation matrixes are calculated for each IMU with the exception of the base IMU in the following order: upper back, head, left upper arm, right upper arm, left forearm, right forearm, left thigh, right thigh, left calf, right calf, left foot, and right foot. The order is significant only in that corrections must be calculated for IMUs proximal to the base IMU before more distal ones. The procedure is as follows:

1. For each sample, compute the uncorrected rotation matrix for the joint between two IMUs relative to the IMU more proximal to the base IMU using equation 3.6.
2. Divide the samples into 60 second segments, overlapping by 30 seconds, and compute a correction rotation matrix, C_i, for each segment using a gradient descent algorithm to minimize cost the function in equation 3.17.
3. Use spherical linear interpolation (equation 3.14) to convert the rotation matrix series, $\{C_1 \cdots C_n\}$, calculated for each segment into a time dependent function.
4. Compute the corrected joint rotation matrixes for each sample using equation 3.7.
5. Compute the corrected rotation matrixes for more the distal IMU relative to the base IMU using equation 3.8.
6. Update the IMU rotation matrixes with the corrected values and move on to the next IMU.
7. After the rotation matrixes for all IMUs have been corrected, a kinematic figure is generated using a separate program.

The algorithm was written in Matlab and executed on a PC with a 2.67 GHz 24x Intel ® Xeon ® CPU.

Chapter 4

4. Results

4.1. Basic Anatomical Constraint Method (ACM)

The basic Anatomical Constraint Method (ACM) described in section 3.1.1 was tested *in silica* by simulating 0 to 30 degree misalignments of the calf or thigh IMUs about the X (lateral/medial) or Z (abduction/adduction) axis. A sinusoidal function was used to simulate rotation of the calf IMU about its Y (flexion/extension) axis between 15 and 75 degrees at a rate of five cycles per minute over a five minute period. Figure 4-1 shows the knee flexion/extension, abduction/adduction, and lateral/medial rotation as a function of time, calculated from changes in the calf and thigh IMUs when both IMUs are correctly aligned with the knee. The knee shows a cyclic flexion/extension between 15 and 75 degrees with no lateral/medial or abduction/adduction.

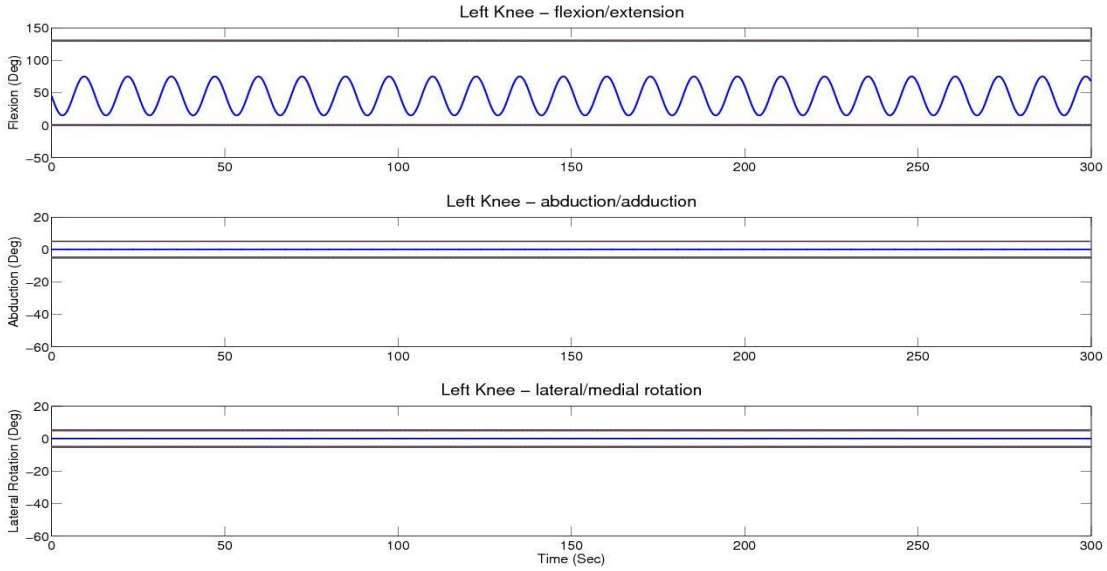

Figure 4-1. Left knee flexion/extension, abduction/adduction, and lateral/medial rotation. Joint angle movement in indicated by the blue plot. Black horizontal lines indicate joint upper and lower limits.

Figure 4-2 shows a comparison of the uncorrected (blue), corrected using the Rivest method (green), and corrected using the basic ACM (red), knee joint angles for the same calf IMU movement simulated in Figure 4-1 but with a simulated 15 degree misalignment of the thigh sensor about the Z axis..

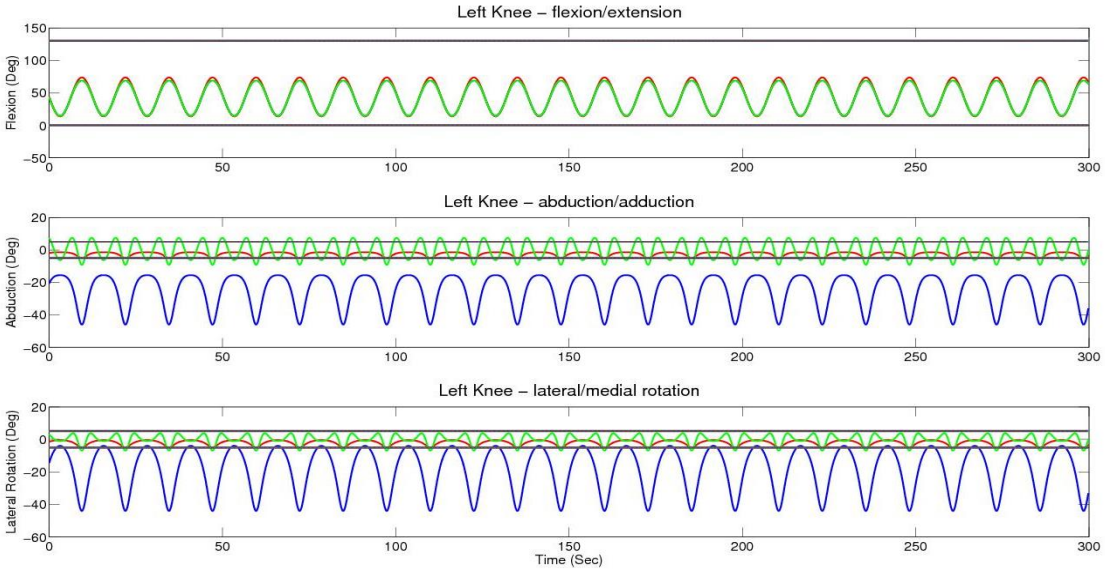

Figure 4-2. Apparent left knee flexion/extension, abduction/adduction, and lateral/medial rotation resulting from a simulated flexion of 15 to 75 degrees with a 15 degree Z axis thigh IMU misalignment. Black horizontal lines indicate joint upper and lower limits. Blue indicates uncorrected joint movement. Green indicates corrected joint movement using the Rivest method. Red indicates corrected joint movement using the ACM.

Misalignment of the thigh sensor causes a slight decrease in the uncorrected flexion/extension, but a large increase in the apparent abduction/adduction and lateral/medial rotation. The large effect on abduction/adduction and lateral/medial rotation is due to the fact that the Euler (Z-Y-X) angle computation approaches a singularity as the flexion angle approaches 90 degrees about the Y axis. As a result, small deviations manifest themselves as large apparent shifts about the other two axes. The Rivest method (green) reduces the amount of abduction/adduction and lateral/medial rotation to almost +/- 5 degrees but does not restore the flexion/extension to +15 to +75 degrees. The ACM (red) decreases the abduction/adduction and

lateral/medial rotation to within 0 to -5 degree and restores the flexion/extension to almost the full +15 to +75 degree range.

Figure 4-3 shows the results for a 15 degree misalignment of the calf IMU about the X axis.

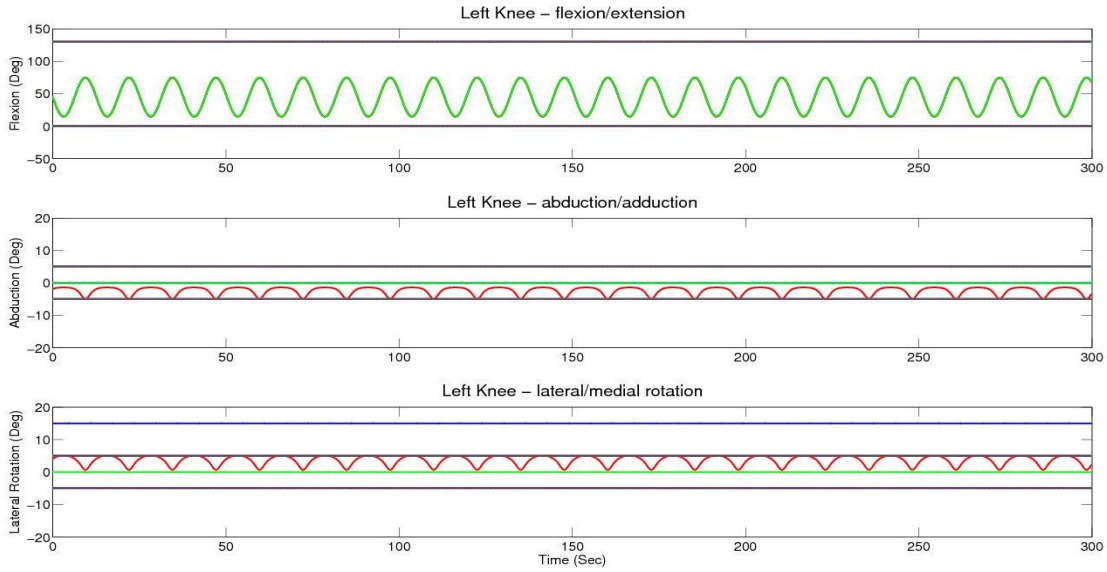

Figure 4-3. Apparent left knee flexion/extension, abduction/adduction, and lateral/medial rotation resulting from a simulated flexion of 15 to 75 degrees with a 15 degree Z axis thigh IMU misalignment. Blue indicates uncorrected, green indicates Rivest correction, and red indicates ACM correction.

Rotation of the calf IMU about its X axis induces a constant 15 degree shift in the knee internal/external rotation but does not affect flexion/extension or abduction/adduction. In this case, the Rivest method eliminates the shift in the internal/external rotation. The ACM reduces the internal/external rotation to between 0 to 5 degrees, while inducing an apparent abduction/adduction to less than 0 to -5 degrees. The flexion/extension of the knee is not affected the Z axis rotation of the thigh IMU.

In all *in silica* simulations, the abduction/adduction and internal/external rotation of the knee is reduced to within the allowed +/- 5 degree limits specified in Table 3-2. The tests also show that the ACM corrects for the error in flexion/extension caused by the sensor misalignment, whereas, the Rivest method does not.

In addition to the *in silica* simulations, the ACM and Rivest methods were also tested using the test frame shown in Figure 2-2(a) by rotating the thigh IMU approximately 30 degrees around the X (lateral/medial) axis and manually flexing the knee between 0 and 60 degrees. The results shown in Figure 4-4 are similar to those obtained by the *in silica* simulation for rotation of the thigh IMU about the Z axis. Both the ACM and Rivest methods reduce the apparent abduction/adduction and lateral/medial movement of the knee to about +/-5 degrees, although the ACM appears to be slightly better than the Rivest method at keeping joint angles within the limits. The ACM also increases the peak flexion/extension slightly, while the Rivest method does not change the flexion/extension.

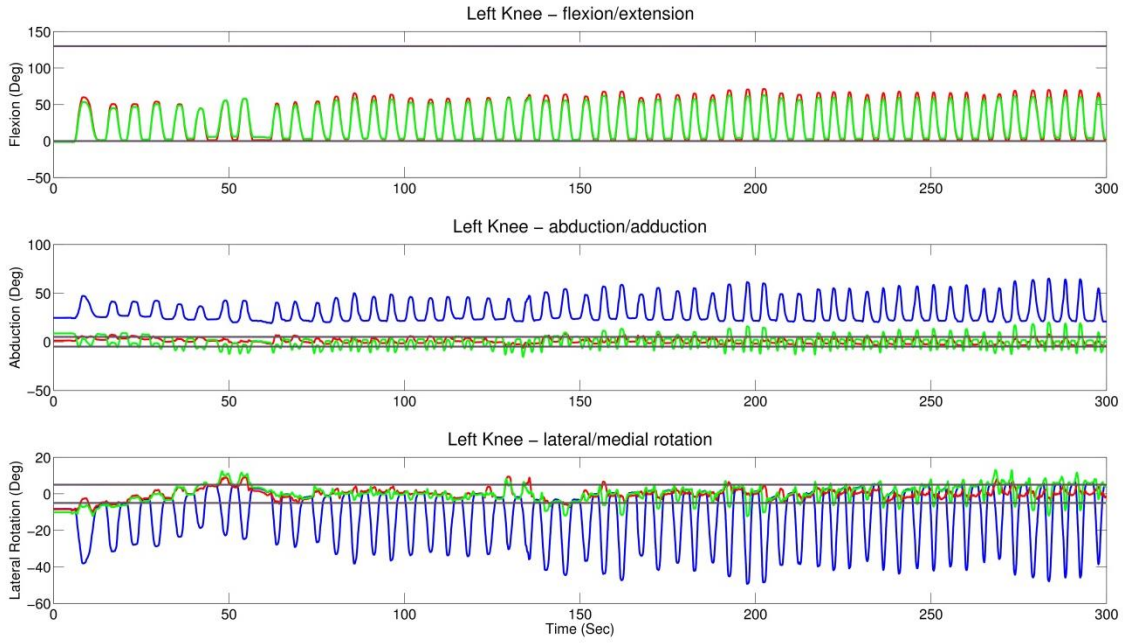

Figure 4-4. Apparent left knee flexion/extension, abduction/adduction, and internal/external rotation resulting from an actual flexion of approximately 0 to 60 degrees with a 30 degree X axis thigh IMU misalignment. Blue indicates uncorrected, green indicates Rivest correction, and red indicates ACM correction.

Figure 4-5 shows a globographic representation of the data used to produce Figure 4-4 (Baker, 2011). Here, the left knee is located at the center of the sphere and the position of the left ankle is represented by points on the surface of the sphere. In this representation, lateral/medial rotation of the knee does not affect the position of the ankle on the sphere's surface, however, it does factor into the color of the points. Blue points indicate that the sample is within all three sets of knee joint limits. Purple indicates that at least one of the joint limits is exceeded by not more than ten degrees. Red indicates that at least one joint limit is exceeded by more than ten degrees. The yellow band indicates the joint limits for flexion/extension and abduction/adduction. The fact that most points in the corrected plot are within the yellow band and colored

either blue or purple shows the effectiveness of the ACM at compensating for IMU misalignment and bringing ankle positon back into alignment with the flexion/extension axis of the knee.

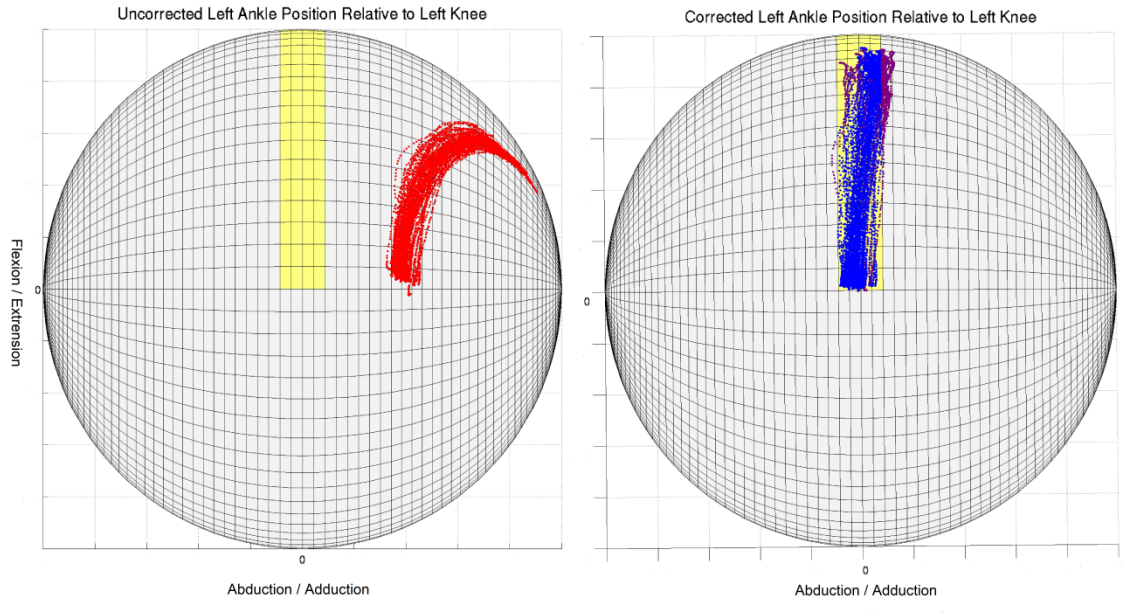

Figure 4-5. Globographic comparison of uncorrected and ACM corrected manual test data. Yellow indicates joint limits. Blue indicates samples within limits. Purple indicates samples within 10 degrees of limits. Red indicates samples more than 10 degrees beyond limits. Grid lines are spaced at 2.5 degree intervals left to right and 5.0 degree intervals top to bottom.

4.2. Drift Correction

I used data from actual trials to test the effectiveness of the senor drift correction algorithm described section 3.2. Figure 4-6 shows a plot of kinematic data from a trial in which sensor drift was apparent in the left thigh IMU. The uncorrected data (blue) shows the drift primarily affecting the abduction/adduction angle. Appling the ACM without drift correction (green) applies a constant positive correction to the abduction angle over the entire trial. This, however, still leaves the abduction/adduction angle outside the anatomical limits for the last 100 seconds of the trial. Adding drift

correction, as described in section 3.3, brings the abduction angle for the later portion of the trial back within anatomical limits and decreases the correction for the first portion. For comparison, a drift correction algorithm using 5^{th} order polynomial curve fitting (black) instead of Slerp is shown. Both drift correction methods give similar results in that the joint angles stay within upper and lower joint limits throughout the trial. However, in some cases, polynomial curve fitting can give degenerate solutions at the edges, so Slerp was the method selected for use.

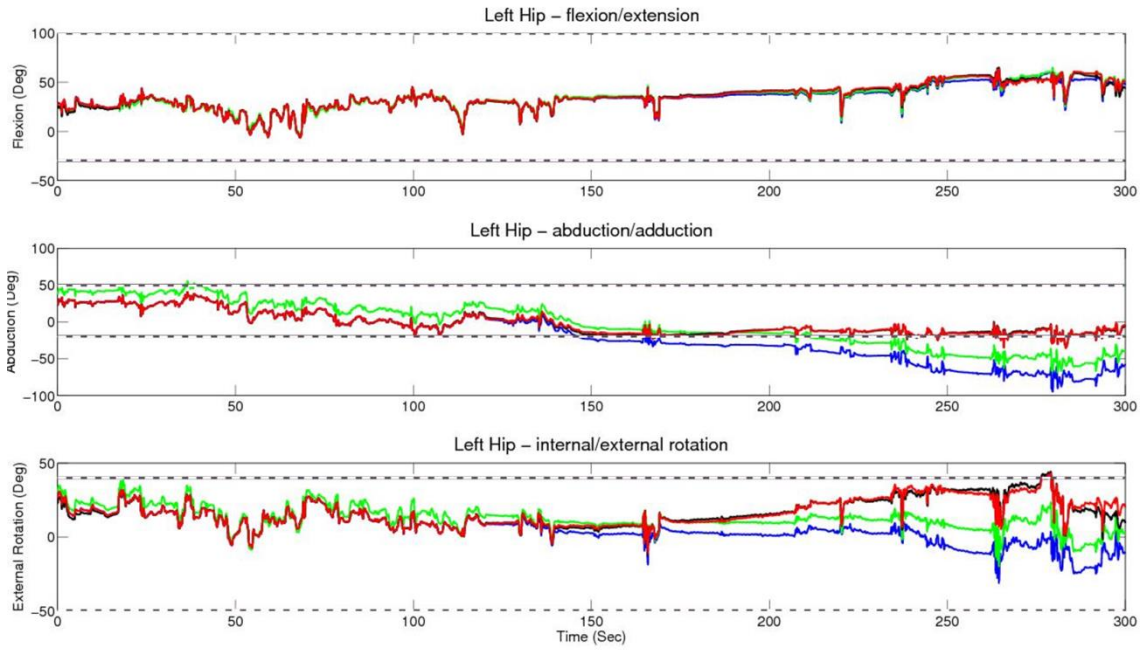

Figure 4-6. Left hip flexion/extension, abduction/adduction, and internal/external rotation showing uncorrected (blue), corrected using ACM without drift correction (green), with drift correction using 5th order polynomial curve fitting (black), and with drift correction using Slerp (red). Dashed lines indicate upper and lower joint limits.

Figure 4-7 shows time-coded 3D scatter plots of corrected and uncorrected joint angles for the left hip. These plots show the effect of left thigh sensor drift on both the abduction/adduction and internal/external rotation joint angles over time.

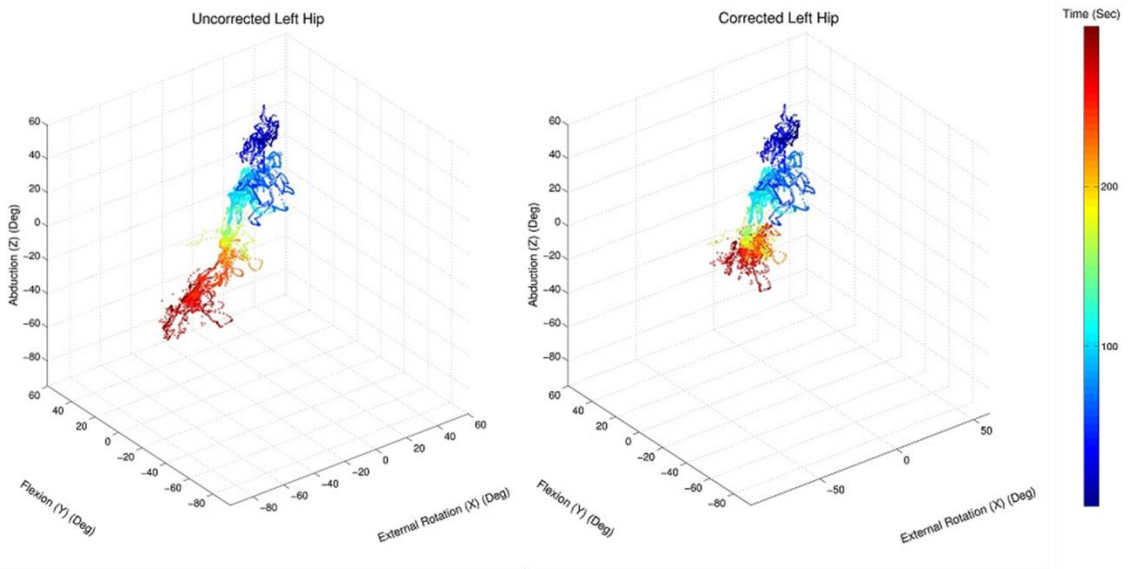

Figure 4-7. Time-coded 3D scatter plot of left hip joint angles corresponding to uncorrected (left) and corrected (right) trial data shown in Figure 4-6. Colors indicate the sample time.

The effect of the drift correction can be seen in that the samples at the end of the trial (red) are shifted toward more positive values of abduction and external rotation. This shift brings the abduction/adduction of the hip at the end of the trial back to within the joint limits.

Figure 4-8 shows time-coded 3D scatter plots of corrected and uncorrected joint angles for the left knee from the same trial. Figures 4-7 and 4-8 indicate that the drift in the left thigh IMU affects the joint angles for both the left hip and knee. The abduction/adduction and lateral/medial rotation knee should be no more than +/- 5 degrees. Applying the ACM with drift correction greatly reduces the extent to which samples exceed these limits.

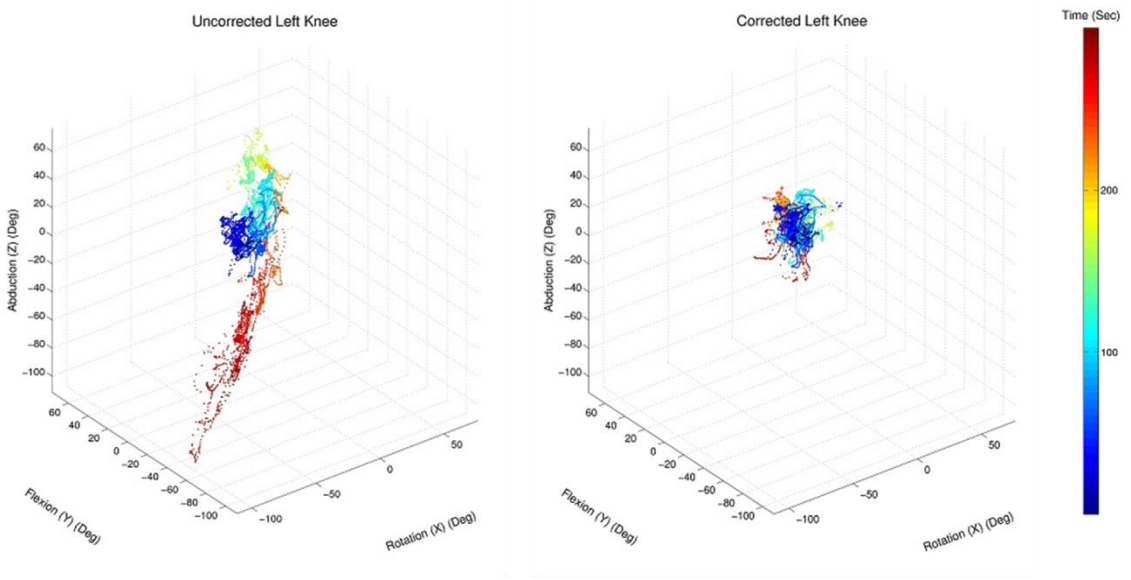

Figure 4-8. Time-coded 3D scatter plot of left knee joint angles for uncorrected (left) and corrected (right) data for the same trial shown in Figures 4-6 and 4-7. Colors indicate the sample time.

4.3. Average Centroid Correction

The anatomical correction method works well for the knee, elbow, and ankle, where rotation around at least one axis is limited. But, since the ACM generates a correction only when one or more joint angles exceeds the anatomical limits for the joint, the results are less conclusive for the spine, neck, shoulders, and hips, which have large ranges of motion about all three axes. This can be seen in Figure 4-6, where there is an apparent constant drift in the left thigh sensor, but drift correction is applied only for the last half of the trial after the lower abduction/adduction limit is exceeded. In an attempt to overcome this shortcoming, I added another term to the cost function of equation 3-16 to adjust the joint angles toward an average centroid of the spine, neck, shoulders, and hips. Different λ_2 regulation coefficients were tested to determine the how much weigh this new term should have.

Figure 4-9 shows the effect of different values of λ_2 on the distribution of joint angles for the data shown in Figure 4-7. As the value of λ_2 is increased from 0 to 30, the abduction of the hip at the start of the trial (top of scatter plot as seen in Figure 4-7) is reduced. This reduction indicates a correction in the joint angles at the start of the trial toward the average centroid to correct for drift that has not yet caused the joint limits to be exceeded. Values of λ_2 larger than 30 did not result in a further reduction in the abduction of the hip at the start of the trial.

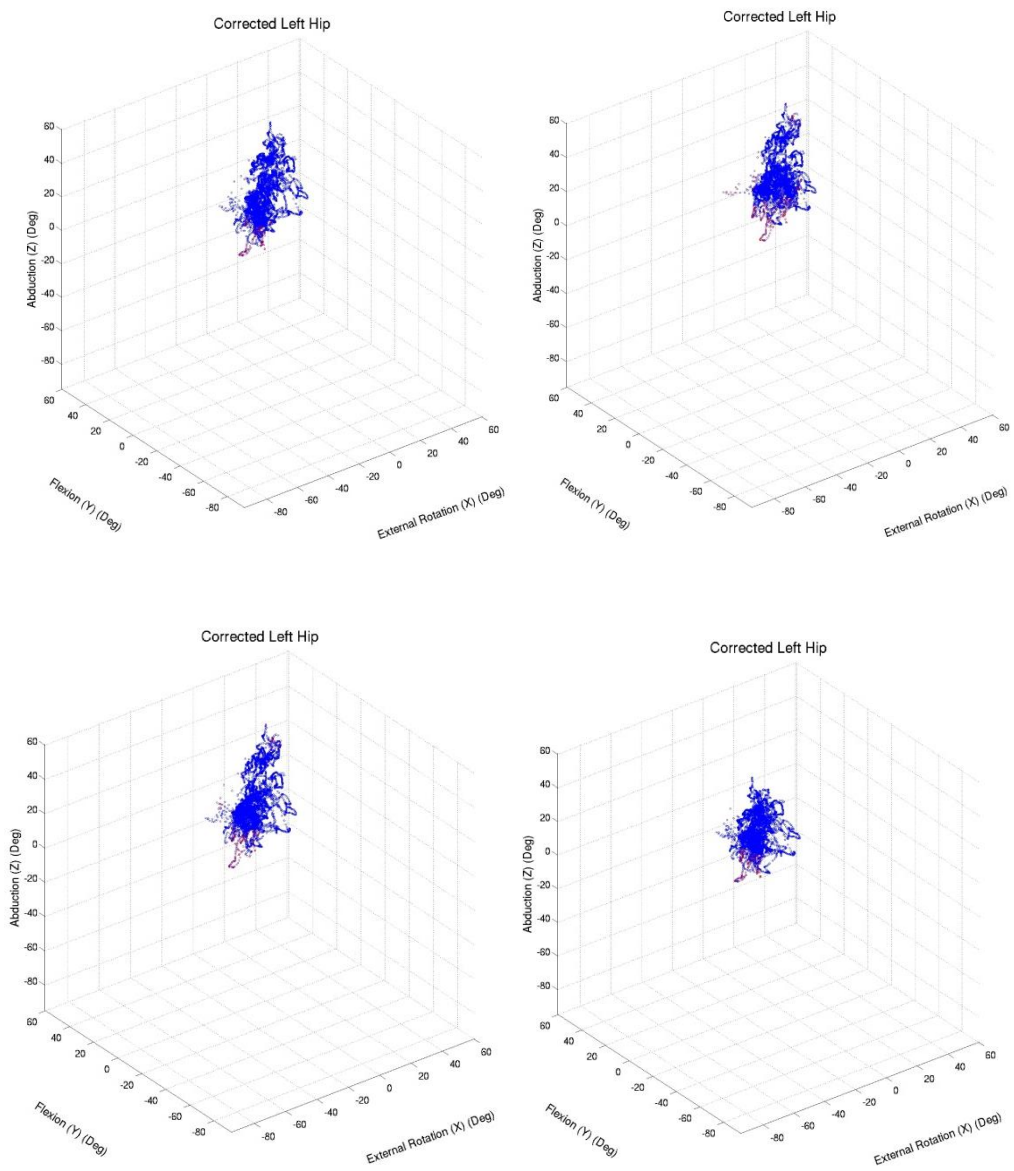

Figure 4-9. 3D scatter plots of left hip joint angles with centroid correction generated using equation 3-17. λ_2 values are 0 (upper left), 10 (upper right), 20 (lower left) and 30 (lower right). Blue indicates samples within limits. Purple indicates samples within 10 degrees of limits.

Figure 4-10 shows a graphical comparison of the corrected joint angles for the left hip. Here, the blue plots show the uncorrected joint angles. The red and green plots show the corrected joint angles with and without the centroid correction. Note that

although both the red and green plots fall almost exclusively within the joint limits, they are substantially different.

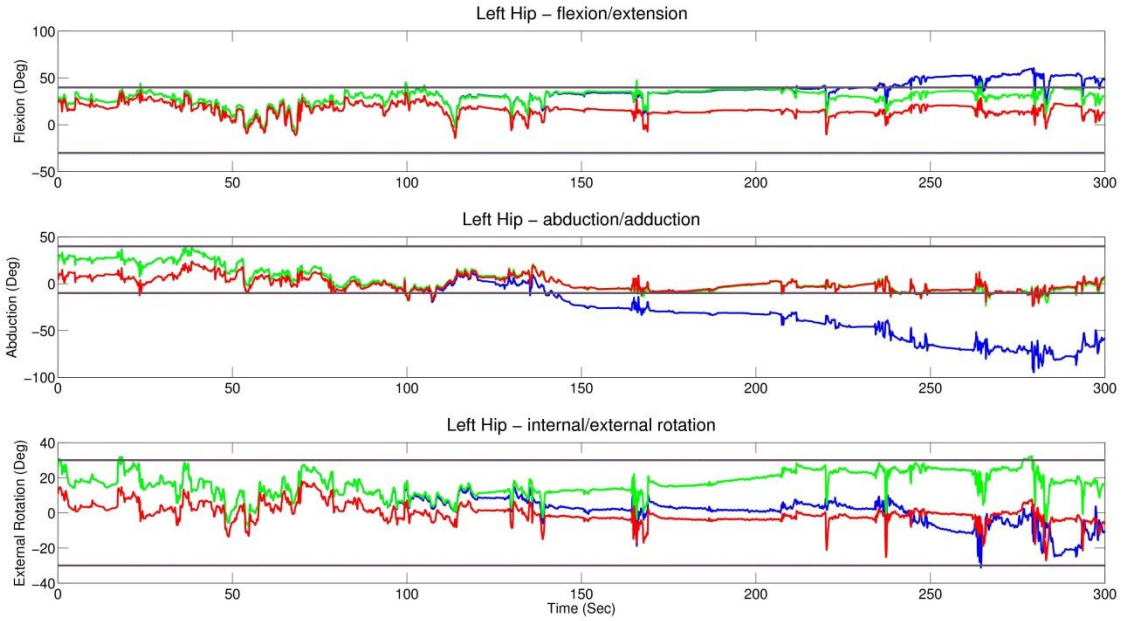

Figure 4-10. Left hip flexion/extension, abduction/adduction, and internal/external rotation showing uncorrected (blue), corrected using ACM with drift correction but without average centroid correction (green), and with average centroid correction with k = 30 (red). Horizontal black lines indicate upper and lower joint limits.

In Figure 4-10, the downward trend in the abduction and external rotation angles during the first 100 seconds of the trial has been eliminated by the centroid correction. During the last 200 seconds, the addition of centroid correction (red) decreases the flexion and external rotation angles relative to the ACM without centroid correction (green), but maintains them within joint limits.

Figures 4-11 through 4-15 show uncorrected (top right), corrected without centroid correction (bottom left), and corrected with centroid correction (bottom right) kinematic figures and right camera video images captured at various times during a trial. The

kinematic figures include an axonometric view (center) as well as side and top projections. The positions of the left arm and leg are not visible in most of the video images.

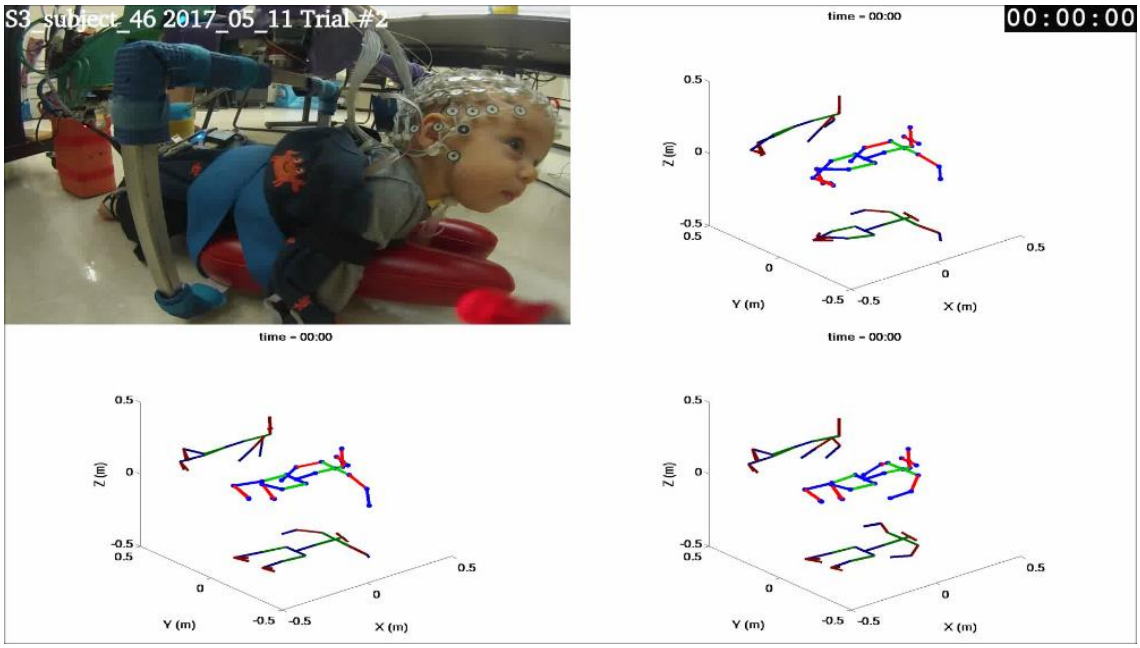

Figure 4-11. Right camera video image (upper left), and uncorrected (upper right), corrected without centroid correction (lower left), and corrected with centroid correction (lower right) kinematic figures at the trial start.

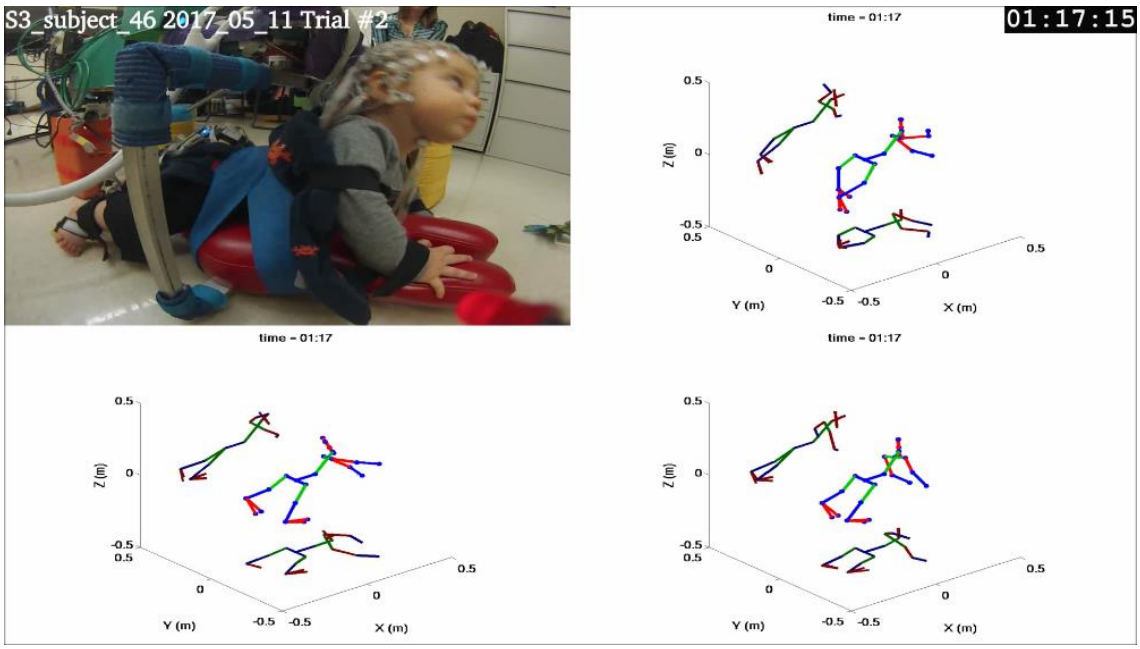

Figure 4-12. Right camera video image (upper left), and uncorrected (upper right), corrected without centroid correction (lower left), and corrected with centroid correction (lower right) kinematic figures at 1 minute 17 seconds into trial.

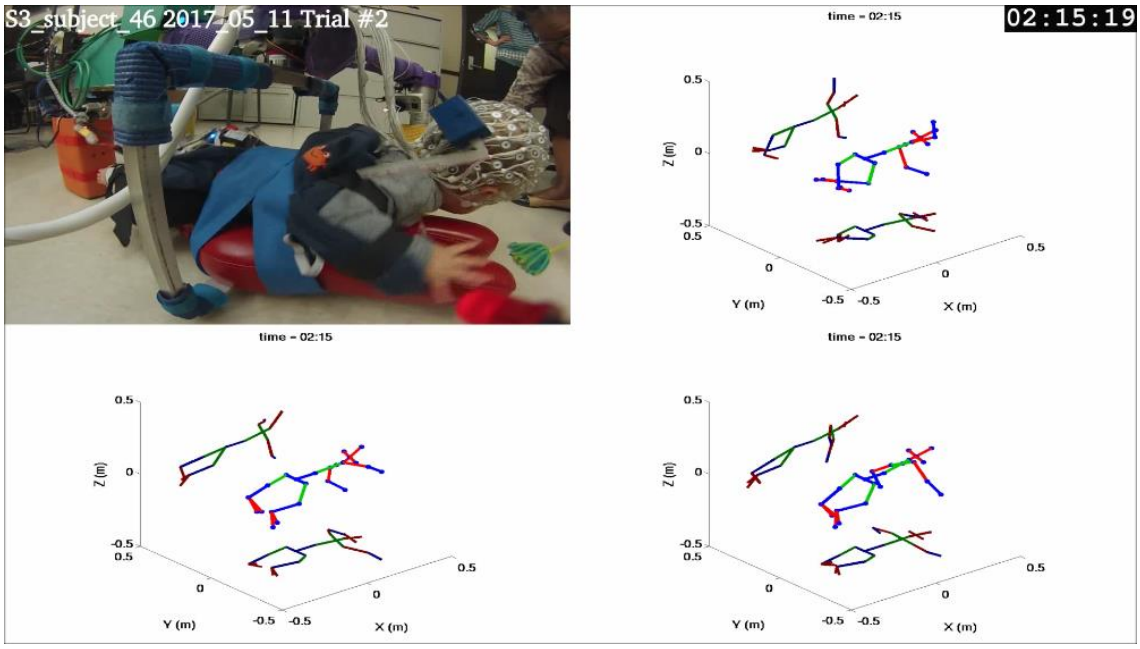

Figure 4-13. Right camera video image (upper left), and uncorrected (upper right), corrected without centroid correction (lower left), and corrected with centroid correction (lower right) kinematic figures at 2 minutes 19 seconds into trial.

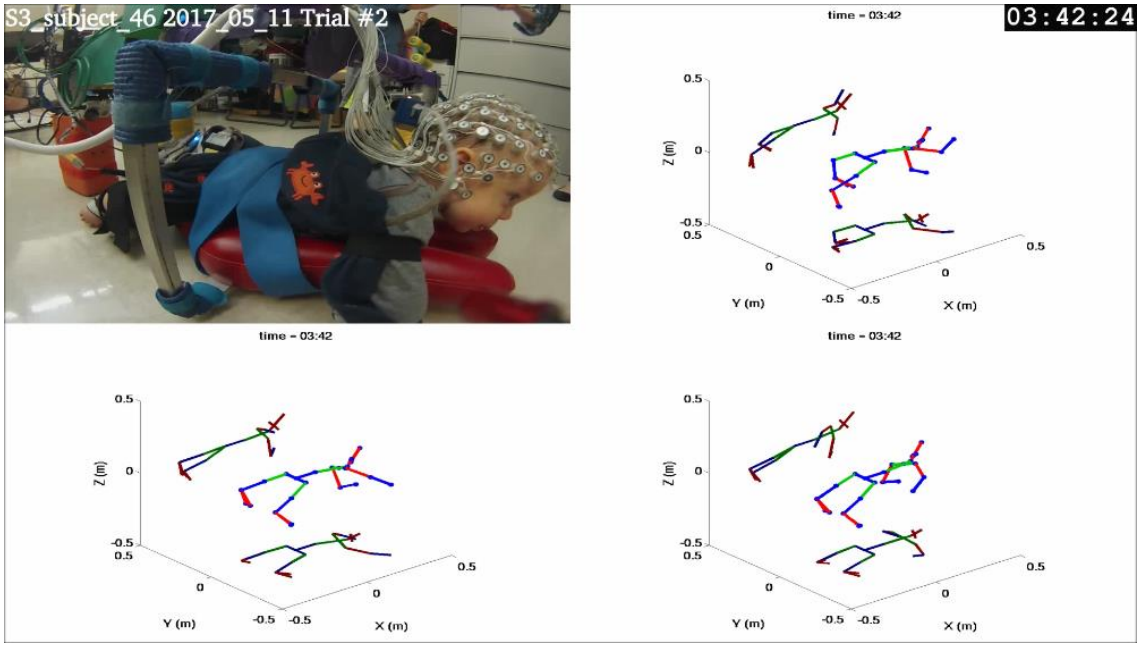

Figure 4-14. Right camera video image (upper left), and uncorrected (upper right), corrected without centroid correction (lower left), and corrected with centroid correction (lower right) kinematic figures at 3 minutes 42 seconds into trial.

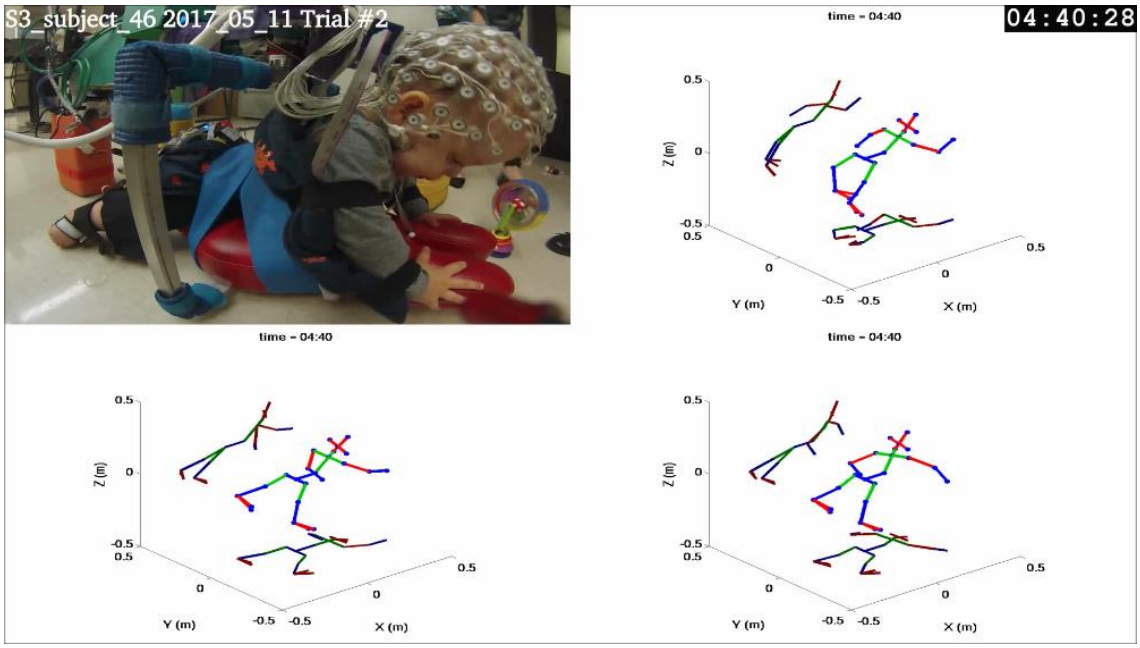

Figure 4-15. Right camera video image (upper left), and uncorrected (upper right), corrected without centroid correction (lower left), and corrected with centroid correction (lower right) kinematic figures at 4 minutes 28 seconds into trial.

In this series, the orientations of the spine and head are the same in the uncorrected and corrected (with and without centroid correction) kinematic figures and appear to match the video images. There is only a limited view of the left arm and leg in the camera video images contained in Figures 4-11 through 4-15. However, it can be seen that the positions of the legs in the corrected kinematic figures do differ from those in the uncorrected kinematic figures and that there is only a slight difference between the figures corrected with and without centroid correction. The rear camera video (not shown) also indicates that the positions of the legs in the corrected kinematic figures are slightly closer to their positions in the videos.

The positions of the arms are markedly different in all three kinematic figures and, although the left arm is partially obscured in the right camera video image, it appears that the positions of the arms in the kinematic figure with centroid correction are closest to their positions in the video image. This can be seen most clearly by examining the positions of the right arm and head in the video compared their positions in the kinematic figure with centroid correction. In Figure 4-11, the infant's right hand is on the floor slightly to the rear of the shoulder and he is looking forward. In Figure 4-12, the infant is pushing off the platform with the right hand and looking upward. In Figure 4-13, the infant has lowered his head but still has his right hand on the platform. In Figure 4-14, his head is lowered and he is looking forward, but he has moved his right hand to the floor under the platform. In Figure 4-15, the infant is again pushing off the platform with his right hand. His head is elevated and he is looking down.

4.4. Overall Performance for a Single Trial with Moderate Drift

Figures 4-16 and 4-17 are snapshots from composite videos created for a single trial, incorporating kinematic figures generated from both uncorrected and ACM with centroid correction data. The first set of snapshots is taken 58 seconds into the trial and shows only slight differences in the positions of the arms and right leg in the uncorrected and corrected kinematic figures. In both figures, the positions of the limbs are reasonably close to those shown in the video.

The snapshots shown in Figure 4-15 are taken 4 minutes and 59 seconds into the trial. By this time, sensor drift has caused the uncorrected kinematic figure (particularly the legs) to appear highly distorted. The positions of the legs and right arm in the corrected kinematic figure accurately reflect their positions in the video images. The position of the left arm is improved in the corrected figure, but appears to be somewhat less forward than in the video image.

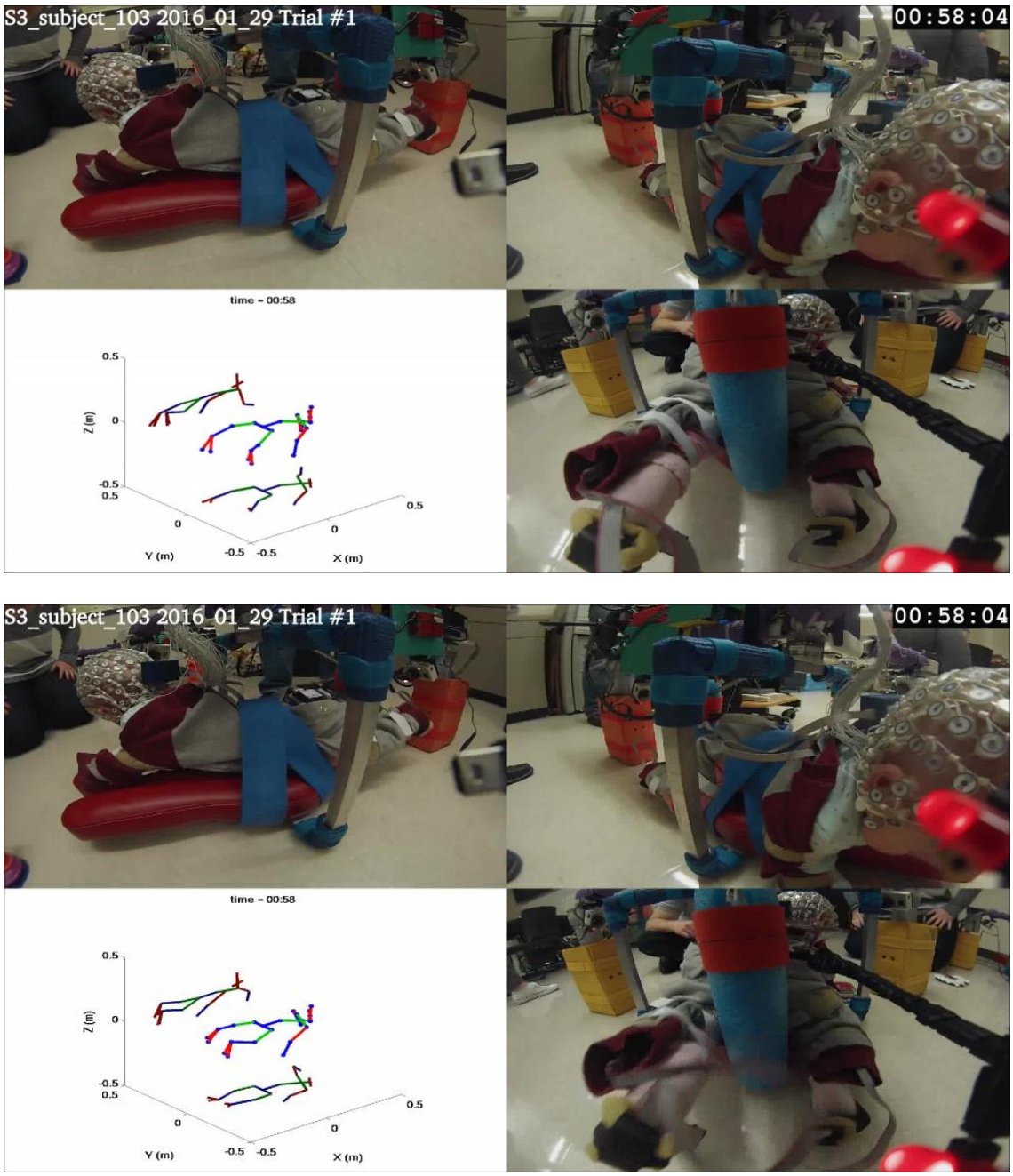

Figure 4-16. Uncorrected (top), and corrected (bottom) composite video image at 58 seconds into trial.

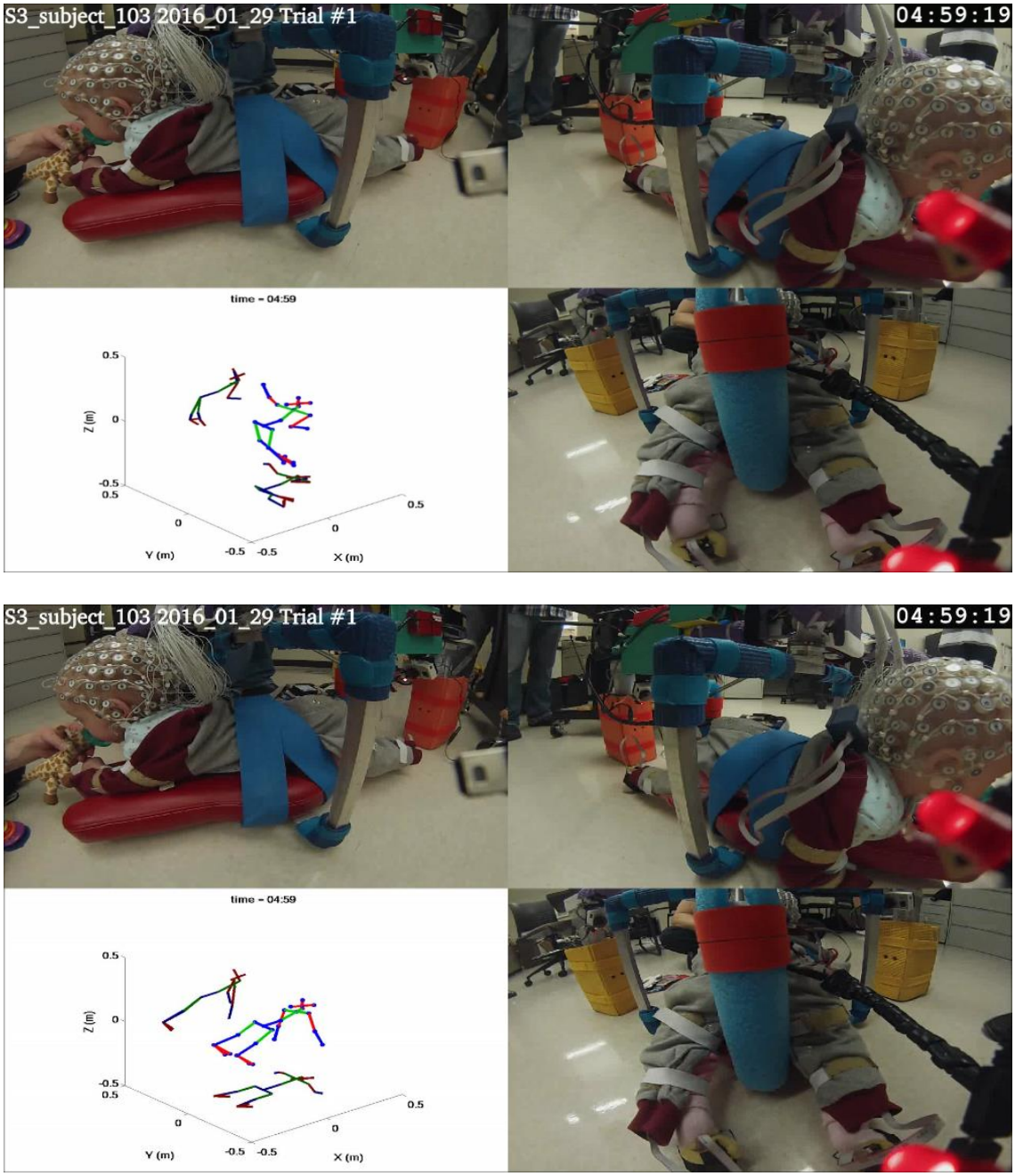

Figure 4-17. Uncorrected (top), and corrected (bottom) composite video image at 4 minutes, 19 seconds into trial.

Joint angle line plots, 3D scatter plots, and globographic plots of the uncorrected and corrected kinematic data for the trial depicted in Figures 4-16 and 4-17 are included in appendixes A – C. These figures show the effectiveness of the algorithm at adjusting

the kinematic data so that the joint angles fall within the normal anatomical range of motion for individual joints. The results show that the majority, but not all, of the joint angles fall within the anatomical limits of Table 3-2. There are two principle reasons for corrected data falling outside the limits: 1) The range of motion around some axes of the knee, elbow, and ankle joints is very limited, and because the IMUs are accurate to only +/- 5 degrees, noise can cause the limits to be exceeded. 2) The limits for the back, neck, shoulders, and hips are more restrictive than the limits described in Luttgens and Hamiltion (1997), to improve the performance of the ACM as described in section 3.1.2. By design, up to 10% of the samples may have joint angles that fall outside the limits specified in Table 3-2.

Table 4-1 shows the percentages of samples falling outside the anatomical limits for each axis of each joint for this trial. Table 4-2 shows the average magnitude of the excursion per sample beyond the joint limits.

Table 4-1. Percentage of samples outside anatomical limits

Joint	Excursion (%)					
	Uncorrected			Corrected		
	X	Y	Z	X	Y	Z
Spine	0.13	0.00	0.00	0.00	0.00	0.00
Neck	1.77	18.06	4.34	0.00	1.25	1.13
Left Shoulder	22.08	87.40	6.83	0.61	0.00	6.89
Right Shoulder	74.05	73.05	21.17	0.03	0.78	0.00
Left Elbow	97.61	19.84	88.42	6.19	11.60	58.50
Right Elbow	8.49	27.27	99.56	2.35	5.31	57.18
Left Hip	0.45	2.28	54.66	0.00	0.00	4.32
Right Hip	24.66	18.76	54.10	0.00	0.00	0.43
Left Knee	92.65	99.12	92.30	41.70	8.03	49.09
Right Knee	93.01	10.84	96.26	60.60	6.87	74.56
Left Ankle	43.86	76.94	99.34	13.96	14.62	59.61
Right Ankle	50.14	12.14	89.05	25.74	7.35	57.04

Table 4-2. Average magnitude of excursion beyond joint limits per sample

Joint	Excursion (Deg)					
	Uncorrected			Corrected		
	X	Y	Z	X	Y	Z
Spine	0.00	0.00	0.00	0.00	0.00	0.00
Neck	0.09	0.51	0.72	0.00	0.06	0.18
Left Shoulder	8.17	15.21	1.25	0.01	0.00	0.70
Right Shoulder	28.97	10.28	1.97	0.01	0.02	0.00
Left Elbow	100.75	2.14	22.04	0.98	1.37	7.71
Right Elbow	1.56	4.15	49.25	0.39	0.49	3.42
Left Hip	0.00	9.12	19.34	0.00	0.00	0.17
Right Hip	2.53	2.10	5.07	0.00	0.00	0.00
Left Knee	24.16	20.62	24.76	1.78	0.18	2.13
Right Knee	29.34	0.56	82.93	3.56	0.43	12.45
Left Ankle	20.12	17.76	87.27	1.87	2.05	10.46
Right Ankle	8.93	1.27	37.98	2.25	0.45	14.07

After correction, both the percentage of joint angles falling outside the normal anatomical limits and the average magnitude of the excursions beyond joint limits are reduced for all joints. Note that because some of the joint limits, particularly for the knee and elbow, are very restrictive, the percentage of samples falling outside the limits is still high, even after correction. However, Table 4-2 shows that the average angular excursions are relatively small. This can be attributed to the fact that the joint limits for some axes of the elbow and knee are the same as the reported +/- 5 degree accuracy of the IMUs.

The large excursions seen in Table 4-2 for the uncorrected left elbow X axis and Z axis of the uncorrected right and left knee are due to the fact that the Euler (Z-Y-X) angle computation approaches a singularity as the flexion angle approaches 90 degrees, as discussed in section 4.1.

Table 4-3 shows the magnitude of the mean shift in the axes over the trial for each joint as a result the correction. The mean shift is the average difference between the joint Euler angles calculated from the uncorrected rotation matrixes for IMU_1 and IMU_2 and those calculated using the corrected rotation matrixes. The axis angle shows magnitude of the shift 3-dimensions.

Table 4-3. Mean shift in joint axes after correction

Joint	Mean Axis Shift (Deg)			Axis Angle (Deg)
	X	Y	Z	
Spine	8.28	3.37	7.68	11.94
Neck	4.07	11.98	15.42	19.60
Left Shoulder	28.83	64.04	6.41	68.36
Right Shoulder	66.28	38.75	71.74	84.45
Left Elbow	83.50	13.80	17.23	83.83
Right Elbow	1.31	7.89	51.85	52.86
Left Hip	5.44	17.71	19.35	26.11
Right Hip	9.15	18.33	33.12	37.12
Left Knee	27.84	21.12	2.07	34.57
Right Knee	31.88	4.82	85.46	88.95
Left Ankle	14.06	32.56	58.09	63.63
Right Ankle	4.05	14.79	21.58	25.99

Execution times in seconds for the ACM algorithm are shown in Table 4-4 for individual joints. The processing times are for the single five minute trial with moderate drift described in this section. This trial includes 15000 data samples.

Table 4-4. Execution times with and without centroid correction

Joint	Execution Time (Sec)	
	Without Centroid Correction	With Centroid Correction
Spine	65.62	260.73
Neck	213.68	242.38
Left Shoulder	132.80	232.62
Right Shoulder	153.31	238.73
Left Elbow	163.08	
Right Elbow	136.27	
Left Hip	176.68	281.12
Right Hip	155.05	246.82
Left Knee	128.77	
Right Knee	120.18	
Left Ankle	127.66	
Right Ankle	147.73	

Total execution time without centroid correction was 1721 seconds (29 minutes) and 2106 seconds (35 minutes) with centroid correction. The increase in execution time when centroid correction is used is due to the additional time required to compute the *RMSq* term in equation 3.27. Total processing time for trials varies somewhat from run to run depending on network loading, but ranges from 30 to 50 minutes for a five minute trial if centroid correction is turned on and graphs are turned off.

4.5. Overall Performance for a Single Trial with Severe Drift

Figures 4-18 and 4-19 are snapshots from a composite video created for a single trial where severe sensor drift was present. In these snapshots, the uncorrected kinematic figure is shown on the bottom left and the corrected figure is shown on the right.

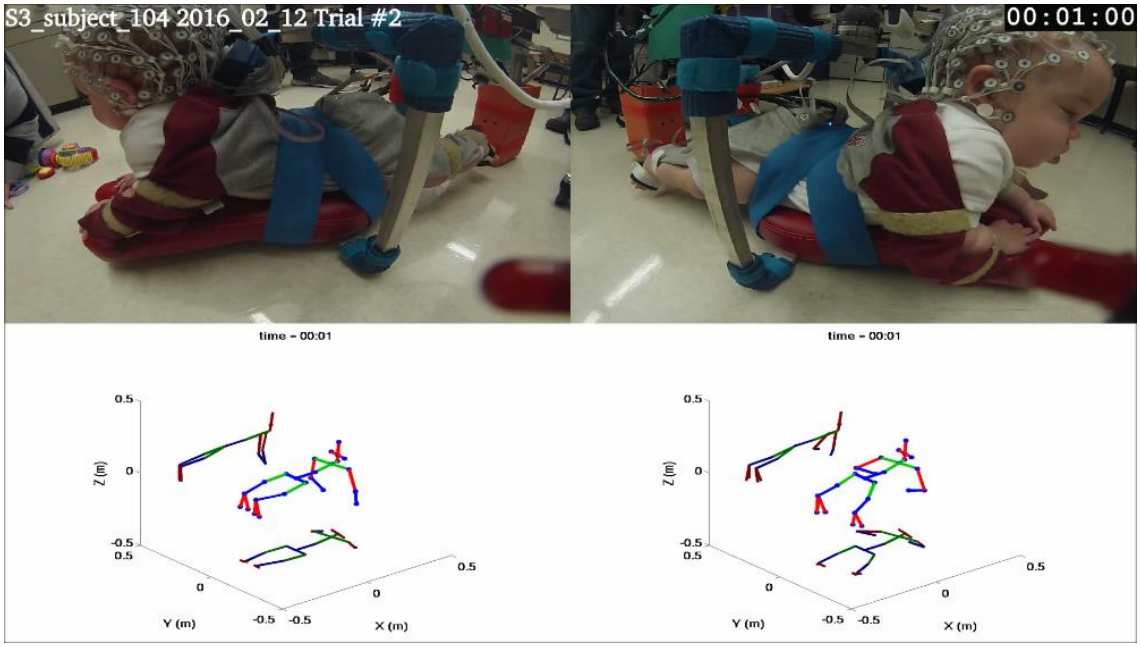

Figure 4-18. Left and right camera images are shown on the upper left and right. Uncorrected and corrected composite kinematic figures are on the lower left and right respectively. Snapshot was taken 1 minute into the trial.

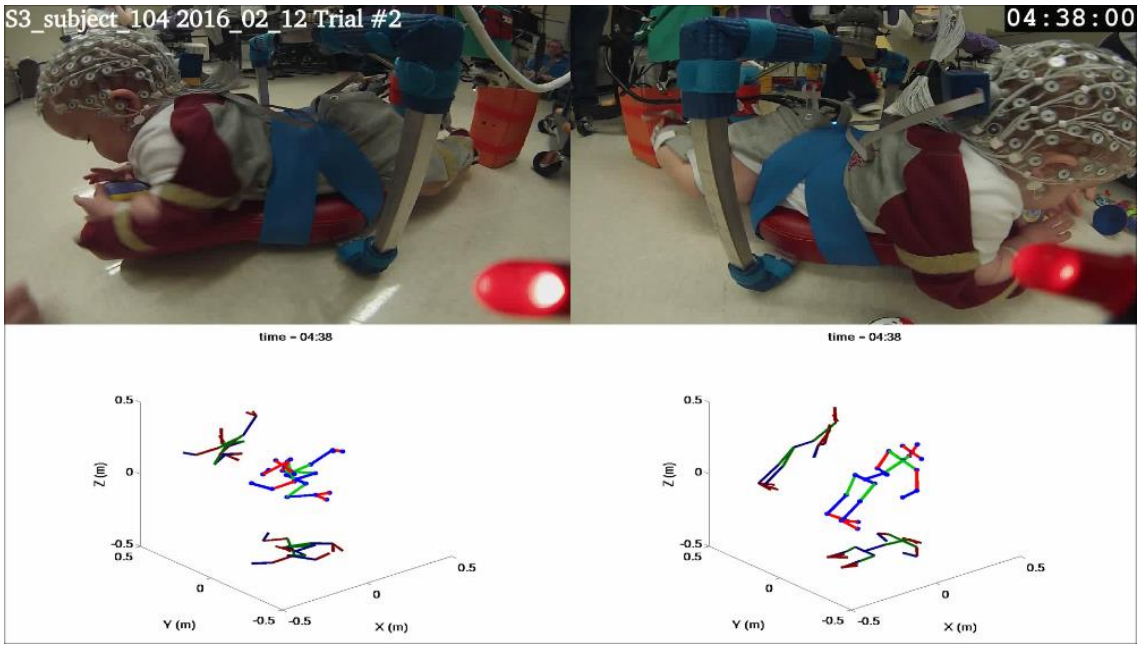

Figure 4-19. Left and right camera images and uncorrected (lower left) and corrected (lower right) kinematic figures at 4 minutes 38 seconds into trial.

The first snapshot was taken 1 minute into the trial, prior to the onset of drift, and shows only slight differences in the positions of the arms and right leg in the uncorrected and corrected kinematic figures. In both figures, the positions of the limbs are reasonably close to those shown in the video, but the positions of the arms in the corrected kinematic figure are closer to their positions in the video. The second snapshot was taken about 3 minutes after the onset of drift and shows the uncorrected kinematic figure to be highly distorted while the corrected kinematic figure still closely matches the video images.

4.6. Performance over Multiple Trials

The average of the angular excursions in three dimensions used in the basic ACM cost function of equation 3.9 can provide a measure of the effectiveness of the algorithm in adjusting the joint angles to be within the anatomical limits of Table 3-2. Figure 4-20 shows the average and worst case cost function values for 20 five-minute trials selected at random from data collected for different infants over a period of 16 months. The average and worst case values for both corrected and uncorrected data are shown for each joint.

$$\frac{1}{3n}\sum_{i=1}^{n}(E_{\theta_i}+E_{\psi_i}+E_{\phi_i})$$

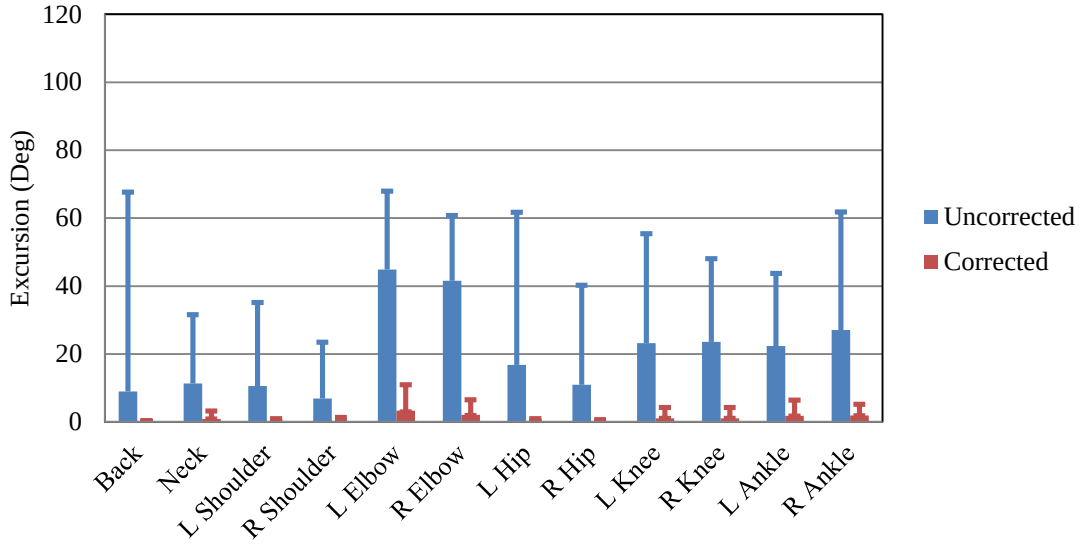

Figure 4-20. Mean (solid bar) and worst trial mean (upper limit marker) excursions for 20 selected trials where: Excursion $= \frac{1}{3n}\sum_{i=1}^{n}(E_{\theta_i}+E_{\psi_i}+E_{\phi_i})$.

By comparing the corrected vs uncorrected average excursion in Figure 5-16, it is apparent that the algorithm is effective at adjusting the IMU axes to reduce the average extent to which the joint angles exceed the joint limits. The elbow, knee, and ankle joints, which have limited ranges of motion, show the most improvement. This is because, for these joints, the range of joint angles outside the joint limits is much greater the range within the limits.

Chapter 5

5. Discussion

The use of IMUs to measure human biomechanical motion has become more common with the advent of small, inexpensive IMUs. The effectiveness of this technique in measuring joint angles is, however, dependent on the ability to correct for IMUs alignment and calibration errors and compensate for IMU sensor drift. Most previous attempts, including the Rivest (2005), and Müller et al. (2017) methods, have focused on individual joints. The Anatomical Constraint Method (ACM), introduced here, is more flexible in that it can be applied to any joint or a system of joints. Although the ACM is tailored to meet the needs of the Self-Initiated Prone Position Crawler (SIPPC), the general approach of using anatomical joint limits may be applied to other IMU based measurements of biomechanical systems.

5.1. Advantages of the ACM

The ACM compares favorably with Rivest's method in reducing the extent of excursions outside the normal range of motion for the knee in all cases where the two methods were compared. The ACM is superior in reducing the abduction/adduction and lateral/medial rotation of the knee and corrects the flexion/extension where the Rivest method does not. In most of the trials, application of the ACM results in an improvement in the alignment of the head, arms, and legs in the kinematic model with their positions in the video recordings. This alignment was usually within 10 - 20 degrees for the head and legs, even when sensor drift was present. Alignment of the position of the shoulder in the kinematic model with the videos was improved, but was not as good as that for the head and legs. This was a result of the large range of motion

of the shoulder joint and difficulty in keeping the upper arm IMU aligned with the major axis of the elbow joint. Correcting the joint angles toward the average angular centroid usually improved the alignment of the shoulder joint.

Applying the ACM over segments rather than the entire trial and then using spherical linear interpolation to generate a time-dependent correction is an effective means for correcting for sensor drift. In general, alignment of the kinematic model with the videos is much better after drift correction.

5.2. Limitations of the ACM

The main limitation of the basic ACM is that the motion about at least one axis of each joint must approach the joint limits at some point during a trial for a correction to occur. This is a particular problem for the shoulders and hips where a wide range of movement is possible around all three axes. Application of the ACM with centroid correction usually helps, but does not always result a kinematic model that closely matches the actual positions of an infant's head, arms, and legs recorded on video. This is because the average orientation of a joint for an individual trial segment may differ from the average orientation over several trials. For example, although the average abduction of the shoulder joint over multiple trials is about -30 degrees, a shoulder joint may be abducted at +30 degrees during most of an individual trial segment. This can result in an incorrect adjustment to the joint angles being applied. For this reason, I made the application of the centroid correction optional, allowing the kinematic model which best matches the video to be selected after visual comparison of the results with and without centroid correction. Generating two sets of corrections does, however,

increase the execution of the algorithm and at present selecting the best match requires manual intervention.

5.3. Future Work

Testing of the SIPPC3 with infants has been ongoing since 2014. During that time, over 2000 trials have been conducted. Evaluation of an infant's crawling ability is assessed, in part, using the Movement Observation Coding System (MOCS) (Rule, 2010). This requires that a physical therapist view the composite videos for each trial and manually log the number of movements of various types made by the infant in 30 second intervals. Since the MOCS includes forty items, this is a time consuming process, taking on average more than an hour per trial. Collection of data is made more difficult by the fact that not all cameras may be operational for the entirety of a trial and camera angles may not always provide a good view of an infant's extremities. Inclusion of a kinematic figure in the composite video, as shown in Figures 4-16 and 4-17, can be an aid by providing another perspective of the infant's limbs. Provided that the kinematic figure is accurate, this should improve the quality of the MOCS data and reduce the time required to collect it.

The recording of many of the items in the MOCS can be automated using the kinematics from the infant sensor suit and the SIPPC itself. For example, the MOCS includes the following items for the upper extremities:

1. "Child moves shoulder horizontally (abducting/adducting) with one hand in contact with floor causing SIPPC to pivot."
2. "Child moves shoulder horizontally (abducting/adducting) with both hands in contact with floor causing SIPPC to pivot."

3. “Child flexes arm while supporting on one hand, SIPPC moves forward.”
4. “Child flexes arm while supporting on both hands, SIPPC moves forward.”
5. “Child alternately moves shoulders horizontally (abducting/adducting) while same hand is in contact with floor, SIPPC pivots.”
6. “Child alternately extends arms while supporting on same hand, moving SIPPC forward.”

These movements and others can be recognized from the kinematic data by a computer algorithm and recorded automatically. This would be a less subjective method for MOCS data collection and could reduce the manual effort required to collect movement statistics.

Although the execution times of the ACM algorithm were about 50 minutes per five minute trial during testing, this may be reduced to approximately ten minutes by using five core processors to calculate corrections for 1) the upper back and head, 2) the upper back, left upper arm, and left forearm, 3) the upper back, right upper arm, and right forearm, 4) the left thigh, left calf, and left foot, and 5) right thigh, right calf, and right foot simultaneously. The ACM algorithm execution time may also be improved by reducing number of kinematic data points used to calculate the correction by a factor of 5 by subsampling the data at an interval of 0.1 seconds. The same correction could then be applied to all samples within the 0.1 second interval.

It is also possible to reduce the range of motion of the hips and shoulders by modeling the interdependency of the 3-dimensional joint limits using quaternions, as described by Liu and Prakash (2003). Expressing the joint limits in terms of quaternions

might also be helpful in reducing large, angular errors that occur when the data approach singularities present in the Euler angle representation.

In its present form, the ACM is to slow to calculate corrections to the kinematics in real-time. If, however, processing time for a 30-second segment could be reduced to something on the order of ten seconds, then a modified algorithm could be developed to apply corrections to the kinematics in near real time. This algorithm would extrapolate IMU corrections for the current segment based on previous segments. This approach would not be as accurate as the interpolative method used in the ACM, but could be used to improve the performance of the SIPPC software that recognizes crawling movements and triggers movement of the SIPPC.

References

Anderson, P., Doyle, L.W., and the Victorian Infant Collaborative Study Group. (2003) Neurobehavioral outcomes of school-age children born extremely low birth weight or very preterm in the 1990s. *The Journal of the American Medical Association* **289(24):**3264–3272.

Baker, M. (1999a). EuclieeanSpace Maths – Conversion to Axis Angle. Retrieved from: http://www.euclideanspace.com/maths/geometry/rotations/conversions/eulerToAngle/index.htm.

Baker, M. (1999b). EuclieeanSpace Maths – Conversion to Quaternion. Retrieved from: http://www.euclideanspace.com/maths/geometry/rotations/conversions/eulerToQuaternion/index.htm.

Baker, R. (2011). Globographic visualization of three dimensional joint angles. *Journal of Biomechanics*, **44:**1885-1891.

Bakhshi, S., Mahoor, M. H., and Davidson, B. S. (2011). Development of a body joint angle measurement system using IMU sensors. *33rd Annual International Conference of the IEEE EMBS*, pp. 6923-6926.

Bertenthal, B. I. and Campos, J. J. (1984). The importance of self-produced locomotion in infancy, Infant Mental Health Journal, **5(5):**160-171.

Clearfield. M. W. (2011). Learning to walk changes infants' social interactions. *Infant Behavior & Development* **34:**14-25.

Cooper, G., Sheret, I., McMillian, L.,Silverdis, K, Ning, S., Hodgins, D., Kenney, L. and Howard, D. (2009). Inertial sensor-based knee flexion/extension angle estimation. *Journal of Biomechanics*, **42:**2678-2685.

Djurić-Jovičić, M. D., Jovičić, N. S., Popović, D. B.,and Djordjević, A. R. (2012). Nonlinear optimization for drift removal in estimation of gait kinematics based on accelerometers. *Journal of Biomechanics*, **45:**2849-2854.

Engin, A. E. and Chen, S. M. (1989). A statistical investigation of the *in vivo* biomechanical properties of the human shoulder complex. *Modelling*, **12(12):**1569-1582.

Favre, J., Jolles, B. M., Aissaoui, R., Aminian, K. (2008). Ambulatory measurement of 3D knee joint angle. *Journal of Biomechanics*, **41:**1029-1035.

Horovitz, M. and Matson, J. L. (2011). Developmental milestones in toddlers with atypical development. *Research in Developmental Disabilities*, **32:**2278-2283.

Kermoian, R. and Campos J. J. (1988). Locomotor experience: a facilitator of spatial cognitive development. *Child Development*, **59(4):**908-17

Kolobe, T. H.-A. and Fagg, A. H. (2014). The effect of sensor robotic technology on the development of prone mobility in infants with or at risk for cerebral palsy. *Journal of Developmental Medicine & Child Neurology* (Special Issue: Abstracts of the American Academy for Cerebral Palsy and Developmental Medicine 68th Annual Meeting), **56(5):**99.

Kolobe, T. H. A., Pidcoe, P., McEwen, I., Pollard, V., and Truesdell, C. (2007). Self-initiated prone progression in infants at risk for cerebral palsy. Pediatric Physical Therapy, **19(1):**93–94.

Kolobe T. H.-A., Fagg A. H. and Ng, Y (2014). Comparison of the effect of robotic reinforced movement learning technology on the development of prone locomotion in infants with and without risk for cerebral palsy. *Proceedings of the Annual Meeting of the Child Neurology Society*, Columbus OH, October p. S223.

Li, Q. and Zhang, J. (2014). Post-trial anatomical frame alignment procedure for comparison of 3D joint angle measurement from magnetic/inertial measurement units and camera-based systems. *Physiological Measurement*, **35:**2255-2268.

Ligorio, G., Zanotto, D., Sabatini, A. M., and Agrawal, S. K. (2017). A novel functional calibration method for real-time elbow joint angles estimation with magnetic-inertial sensors. *Journal of Biomechanics*, **54:**106-110.

Liu, Q. and Prakash, E. (2003). "The Parameterization of Joint Rotation with the Unit Quaternion," Proc. 7th Digital Image Computing: Techniques and Applications, Sydney, December pp. 410-417.

Liu, T., Inoue, Y., and Shibata, K. (2009). Development of a wearable sensor system for quantitive gait analysis. *Measurement*, **42**:978-988.

Luttgens, K. and Hamilton, N. (1997). Kinesiology: Scientific Basses of Human Motion, 9th Ed., Madison, WI: Brown & Benchmark.

Luinge, H. J., Veltink, P. H., and Baten, C. T. M. (2007). Ambulatory measurement of arm orientation. *Journal of Biomechanics* **40:**78-85.

Miller, D. P., Fagg, A. H., Ding, L., Kolobe, T. H.-A., Ghazi, M. A. (2015) Robotic crawling assistance for infants with cerebral palsy. AAAI Workshop on Artificial Intelligence Applied to Assistive Technologies and Smart Environments: pp 36-38.

Müller, P., Bégin, M., Schauer, T., and Seel, T. (2017) Alignment-free, self-calibrating elbow angles measurement using inertial sensors. *IEEE Journal of Biomedical and Health Informatics*, **21(2):**312-319.

Rivest, L. (2005) A correction for axis misalignment in the joint angle curves representing knee movement in gait analysis. *Journal of Biomechanics*, **38:**1604-1611.

Rule, B. A. (2010) Motor strategies implemented by infants using the self-initiated prone progression crawler. Master's thesis. University of Oklahoma Health Sciences Center.

Seel, T., Raisch, J., and Schauer, T. (2014) IMU-based joint angle measurement for gait analysis. *Sensors*, **14:**6891-6909.

Shoemake, K. (1985) Animating Rotation with Quaternion Curves. *Siggraph*, **19(3)**:245-254

Soucie, J. M., Wang, C., Forsyth, A., Funk, S., Demmy, M, Roach, K. E., and Boone, D. (2011) Range of motion measurements: reference values and a database for comparison studies. *Haemophilia*, **17:**500-507.

Southerland, J. B. (2012) Activity recognition and crawling assistance using multiple inexpensive inertial measurement units, Master's thesis, School of Computer Science, University of Oklahoma.

Takeda, R., Lisco, G., Fujisawa, T., Gastaldi, L, Tohyama, H., and Tadano, S. (2014) Drift removal for improving the accuracy of gait parameters using wearable sensor systems. *Sensors*, **14:**23230-23247.

Appendix A: Joint Angle Plots

Joint angle plots for uncorrected (blue) and corrected (red) kinematic data from a single trial. Upper and lower joint angle limits are indicated by black horizontal lines. These plots show the uncorrected and corrected angular positions of the joints with time. The magnitude of the correction applied to each axis at any time is equal to the difference between the blue and red plots.

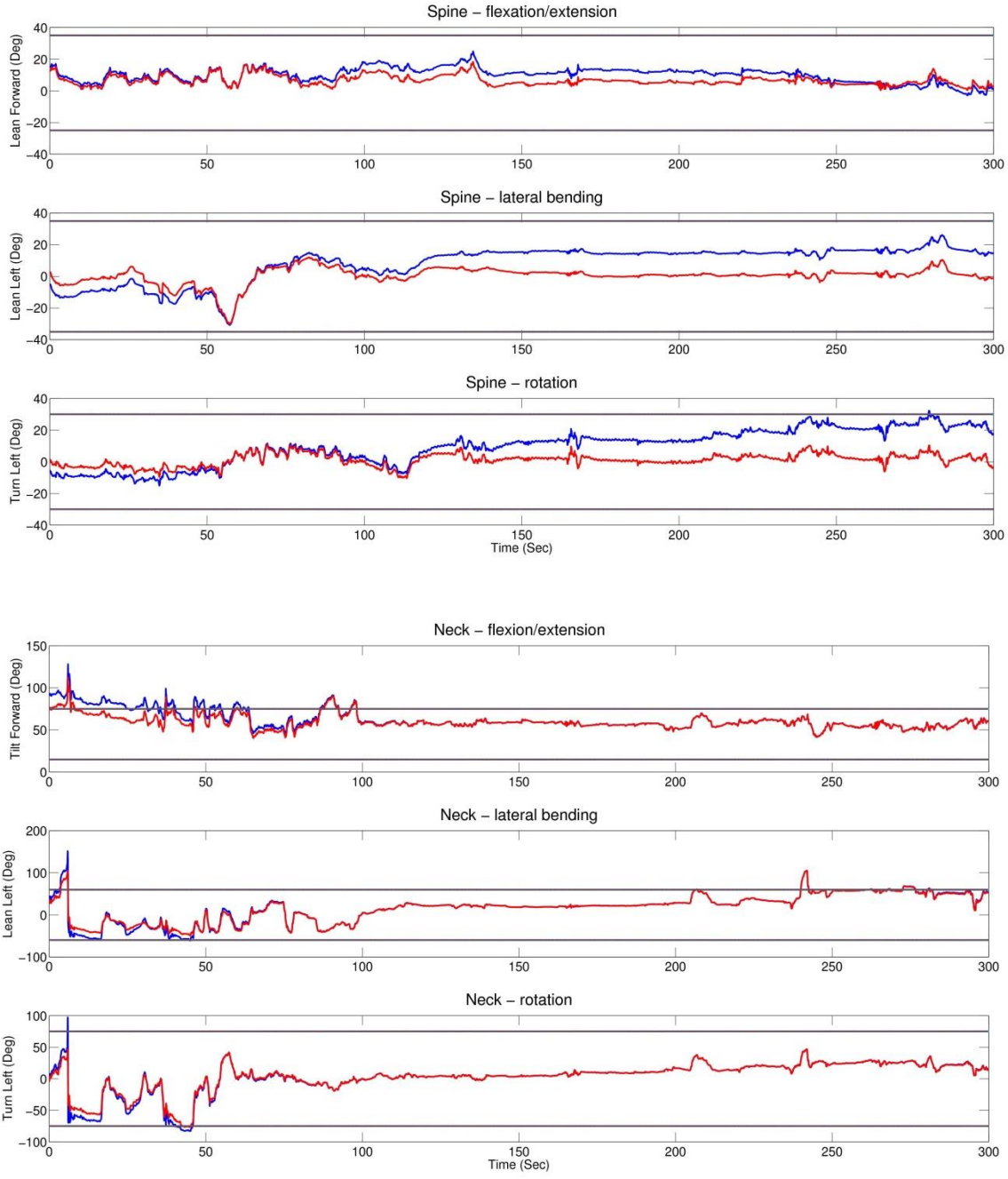
Spine – flexation/extension
Lean Forward (Deg)
Spine – lateral bending
Lean Left (Deg)
Spine – rotation
Turn Left (Deg)
Time (Sec)
Neck – flexion/extension
Tilt Forward (Deg)
Neck – lateral bending
Lean Left (Deg)
Neck – rotation
Turn Left (Deg)
Time (Sec)

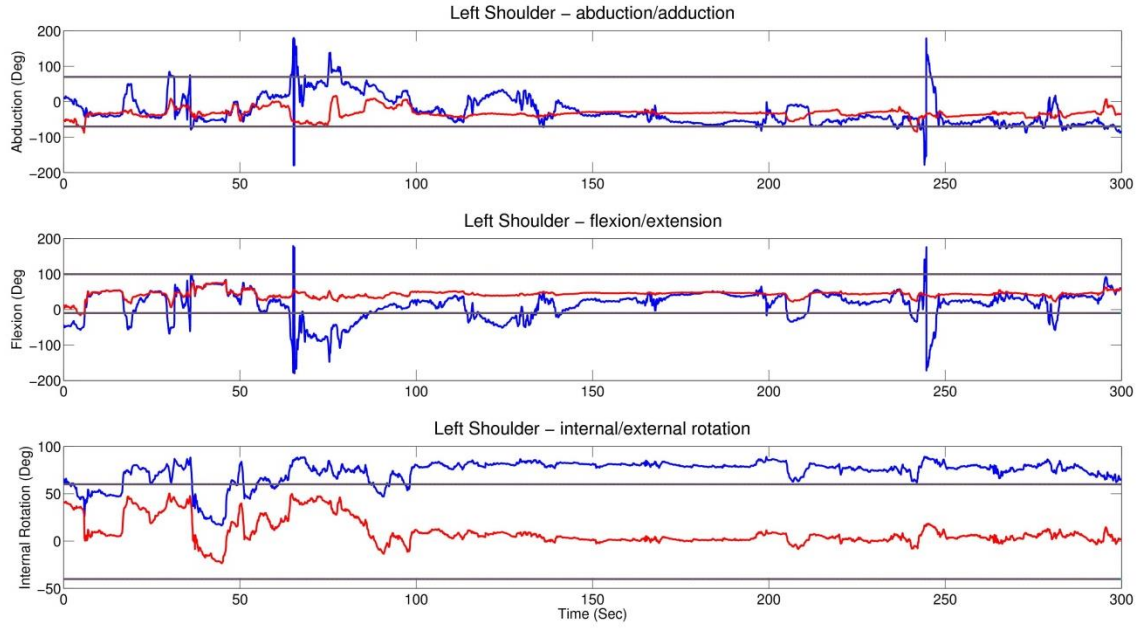
Left Shoulder – abduction/adduction
Abduction (Deg)
Left Shoulder – flexion/extension
Flexion (Deg
Left Shoulder – internal/external rotation
Internal Rotation (Deg)
Time (Sec)

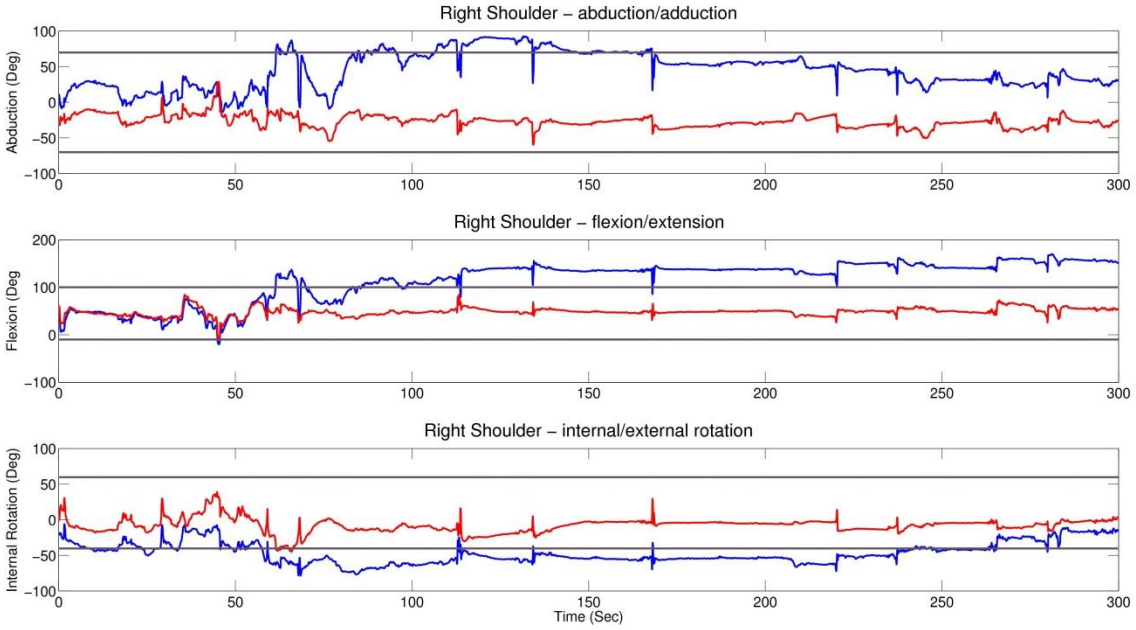
Right Shoulder – abduction/adduction
Abduction (Deg)
Right Shoulder – flexion/extension
Flexion (Deg
Right Shoulder – internal/external rotation
Internal Rotation (Deg)
Time (Sec)

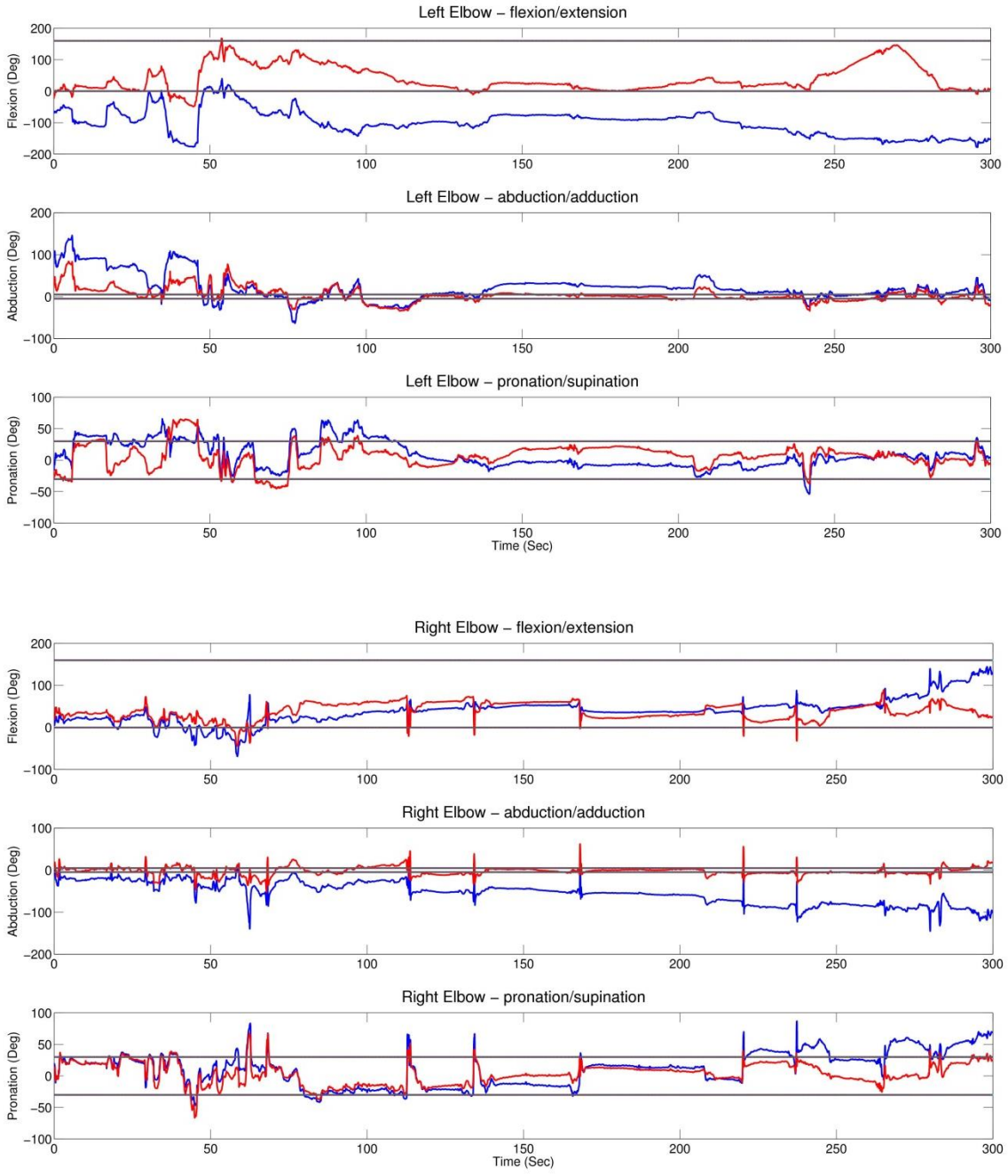
Left Elbow – flexion/extension
Flexion (Deg)
Left Elbow – abduction/adduction
Abduction (Deg)
Left Elbow – pronation/supination
Pronation (Deg)
Time (Sec)
Right Elbow – flexion/extension
Flexion (Deg)
Right Elbow – abduction/adduction
Abduction (Deg)
Right Elbow – pronation/supination
Pronation (Deg)
Time (Sec)

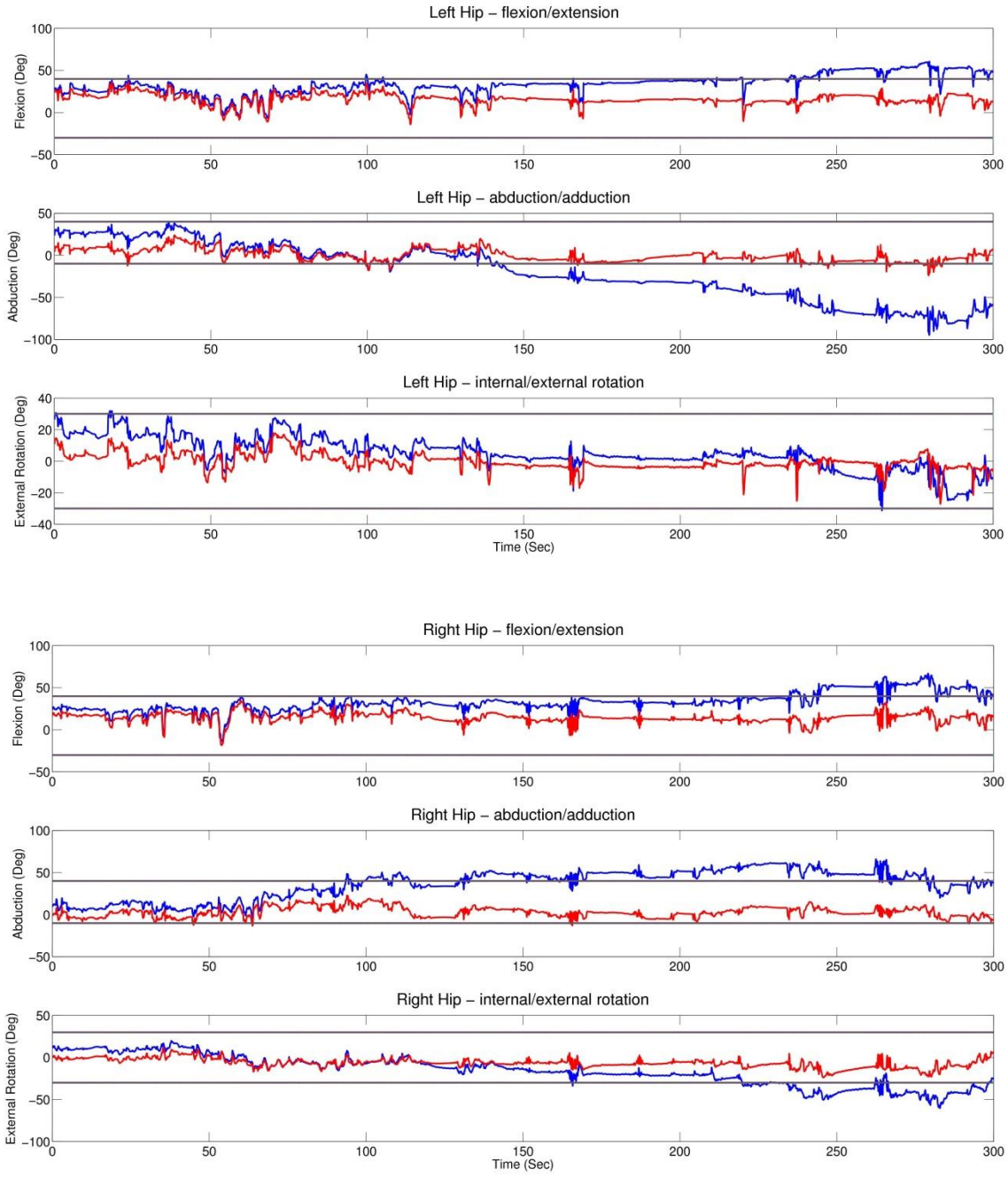
Left Hip – flexion/extension
Flexion (Deg)
Left Hip – abduction/adduction
Abduction (Deg)
Left Hip – internal/external rotation
External Rotation (Deg)
Time (Sec)
Right Hip – flexion/extension
Flexion (Deg)
Right Hip – abduction/adduction
Abduction (Deg)
Right Hip – internal/external rotation
External Rotation (Deg)
Time (Sec)

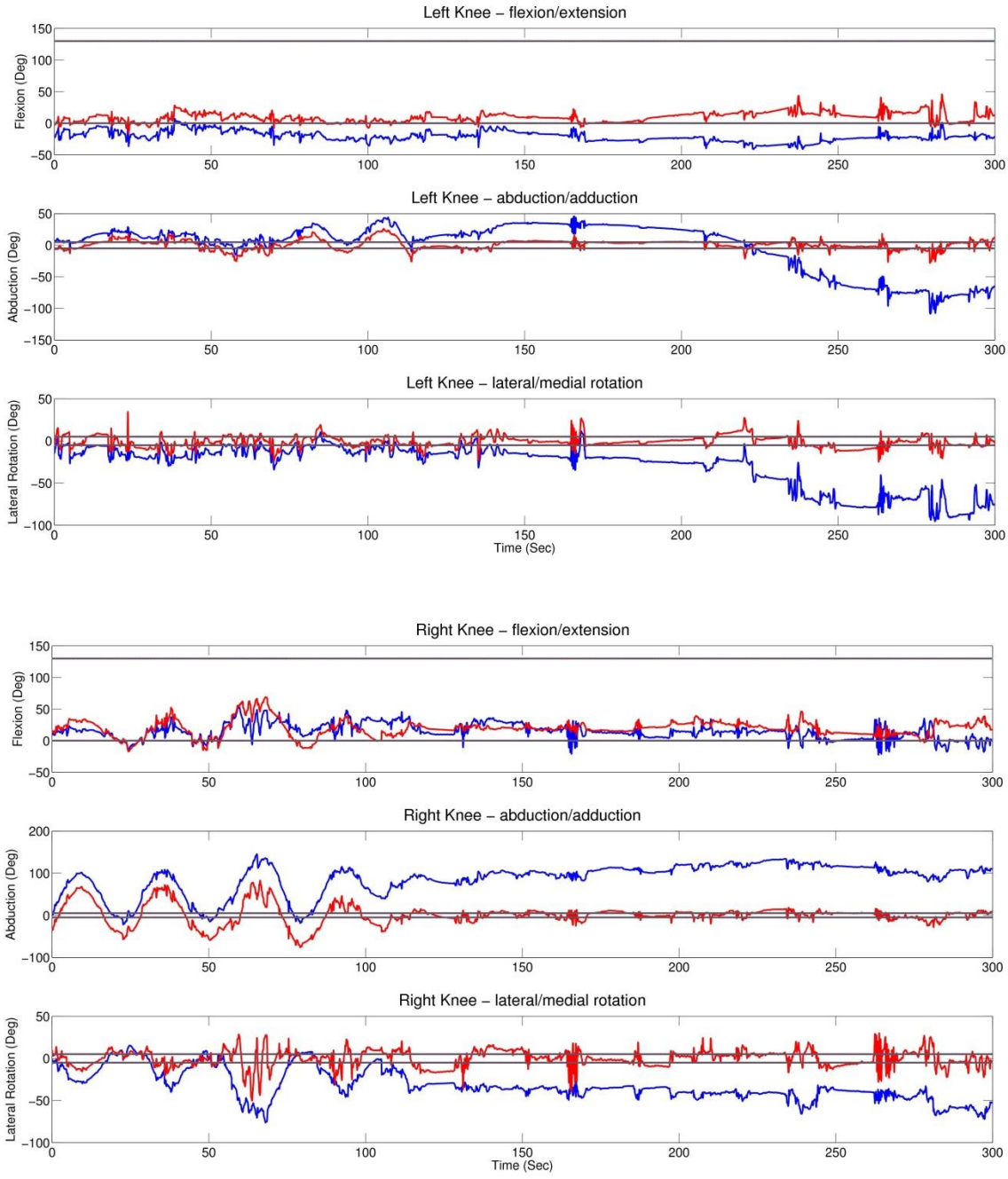
Left Knee – flexion/extension
Flexion (Deg)
Left Knee – abduction/adduction
Abduction (Deg)
Left Knee – lateral/medial rotation
Lateral Rotation (Deg)
Time (Sec)
Right Knee – flexion/extension
Flexion (Deg)
Right Knee – abduction/adduction
Abduction (Deg)
Right Knee – lateral/medial rotation
Lateral Rotation (Deg)
Time (Sec)

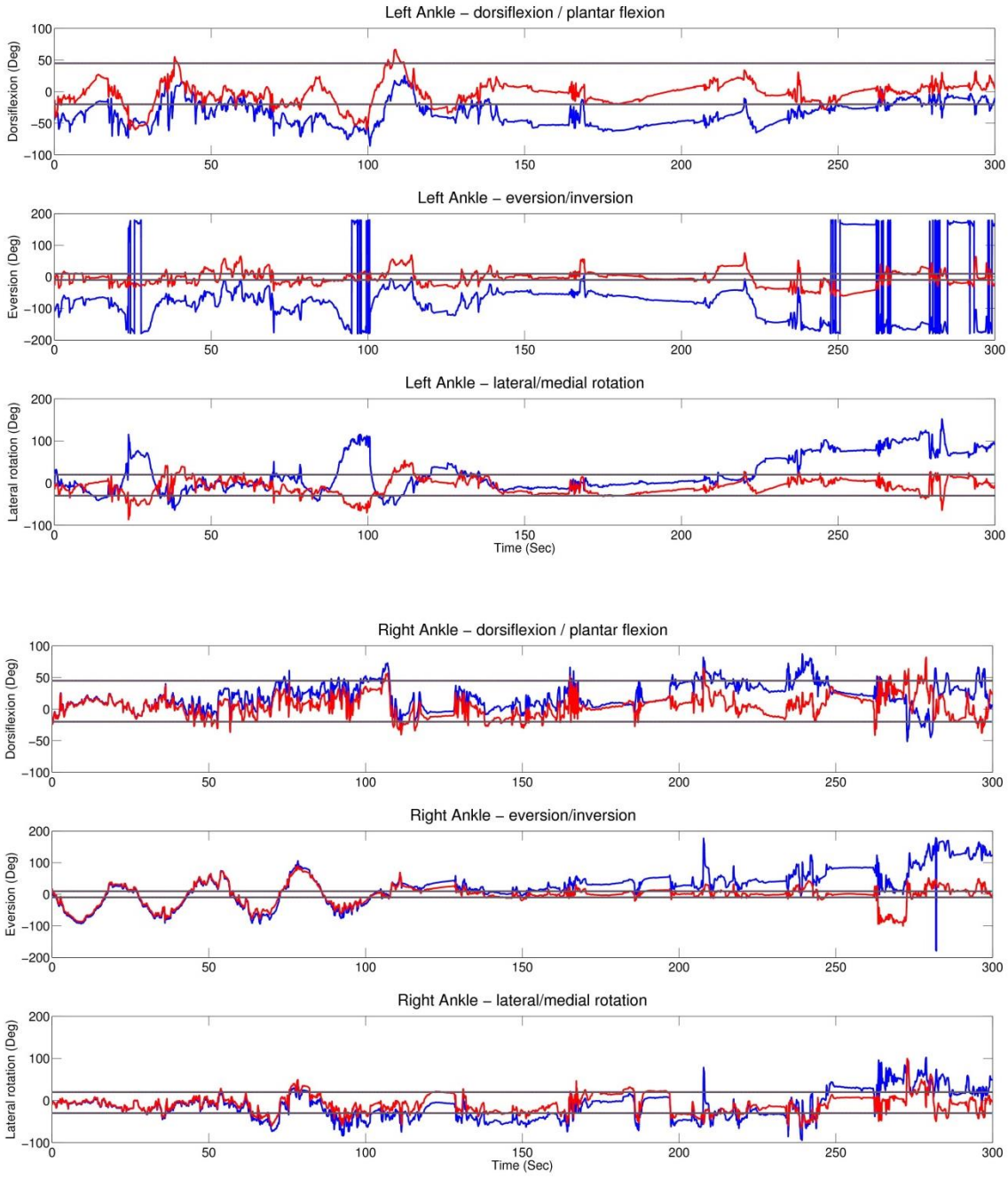
Left Ankle – dorsiflexion / plantar flexion
Dorsiflexion (Deg)
Left Ankle – eversion/inversion
Eversion (Deg)
Left Ankle – lateral/medial rotation
Lateral rotation (Deg)
Time (Sec)
Right Ankle – dorsiflexion / plantar flexion
Dorsiflexion (Deg)
Right Ankle – eversion/inversion
Eversion (Deg)
Right Ankle – lateral/medial rotation
Lateral rotation (Deg)
Time (Sec)

Appendix B: Joint Angle 3D Scatter Plots

3D scatter plots of kinematic joint angle data for a single trial. Blue points are samples within joint limits. Purple indicates samples within 10 degrees of limits. Red indicates samples more than 10 degrees beyond limits. In general, the distributions of points for corrected data is more compact and contains more blue points that are within the joint limits than the uncorrected data.

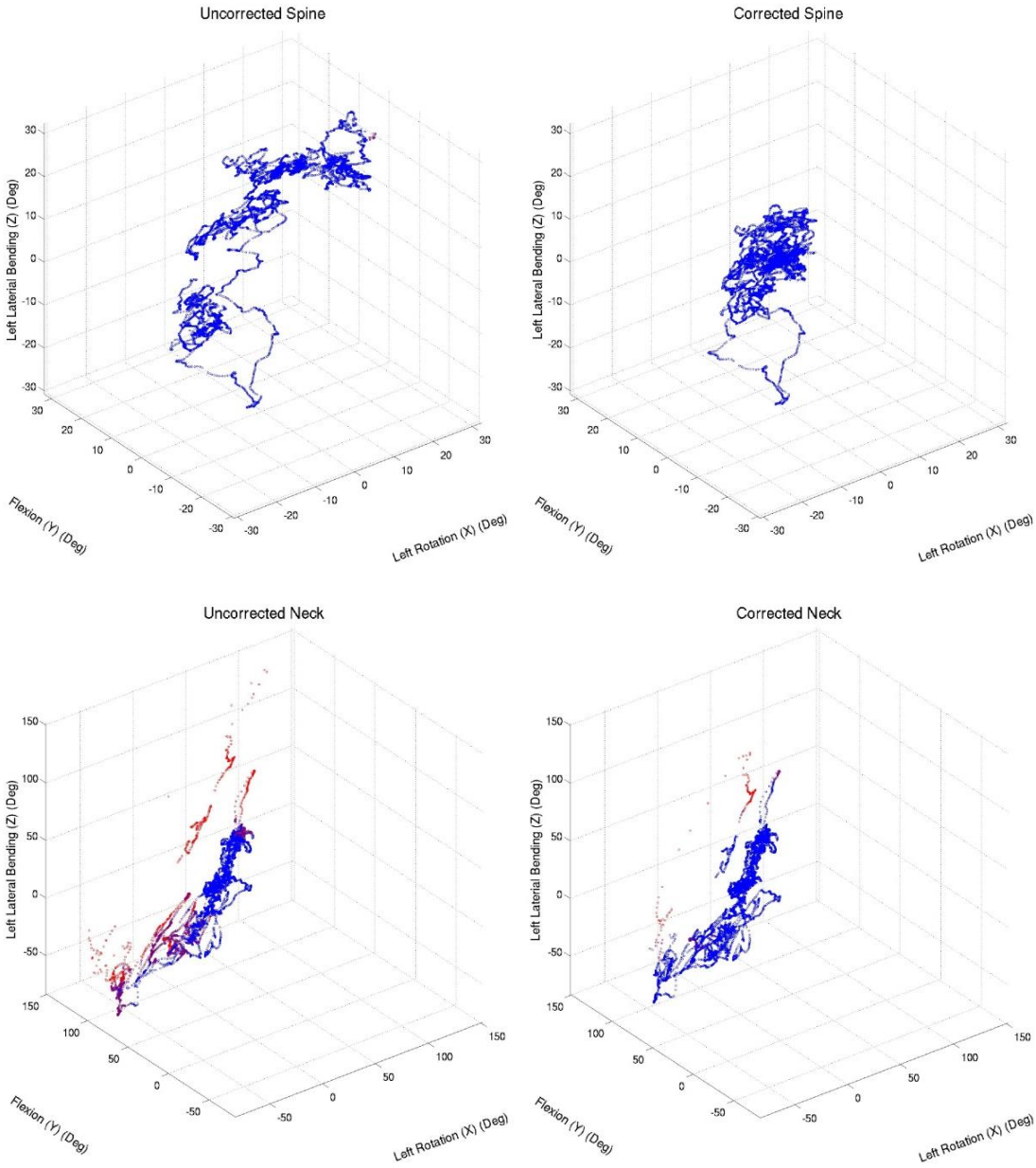

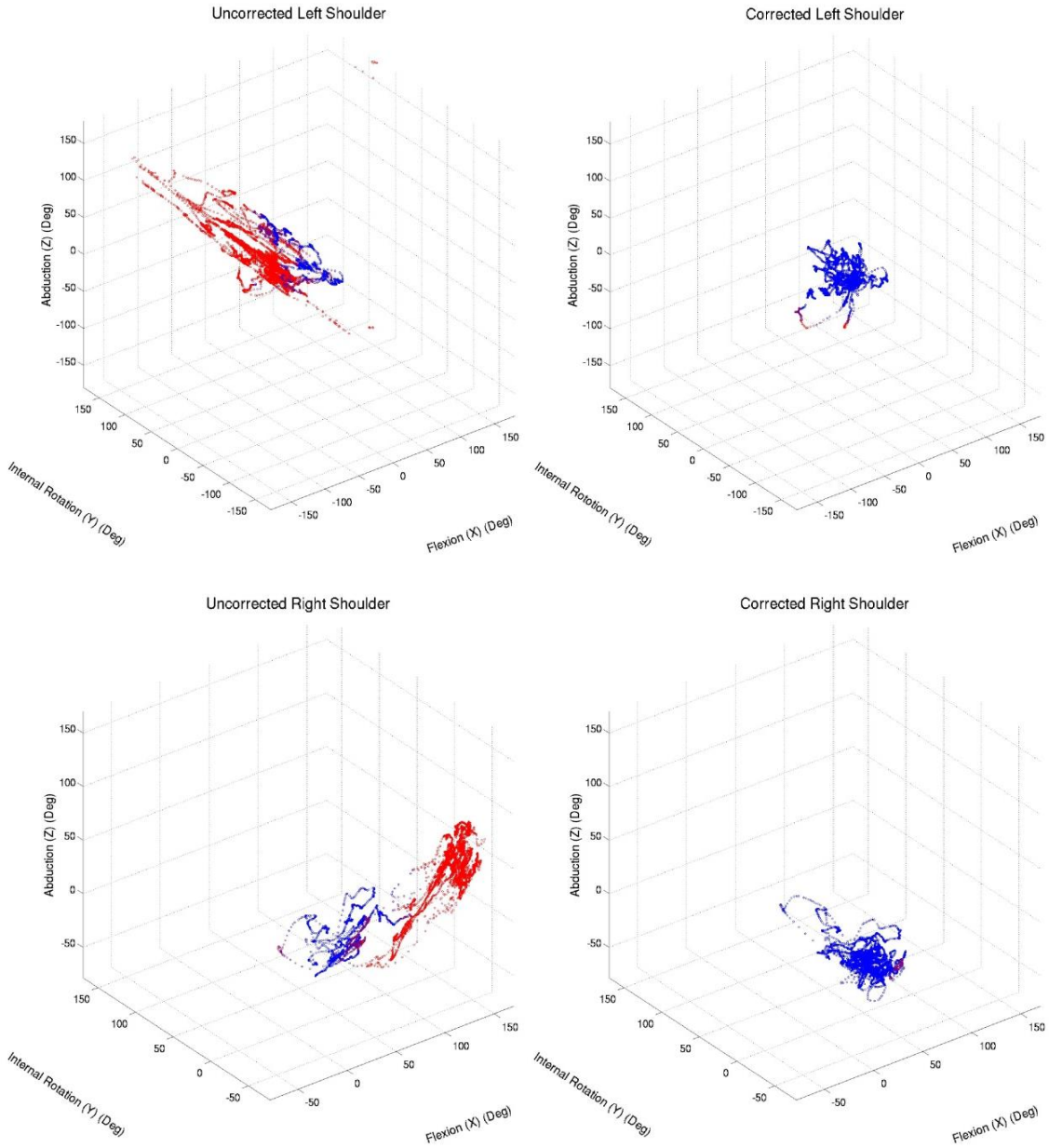
Uncorrected Left Shoulder
Corrected Left Shoulder
Uncorrected Right Shoulder
Corrected Right Shoulder
Abduction (Z) (Deg)
Internal Rotation (Y) (Deg)
Flexion (X) (Deg)

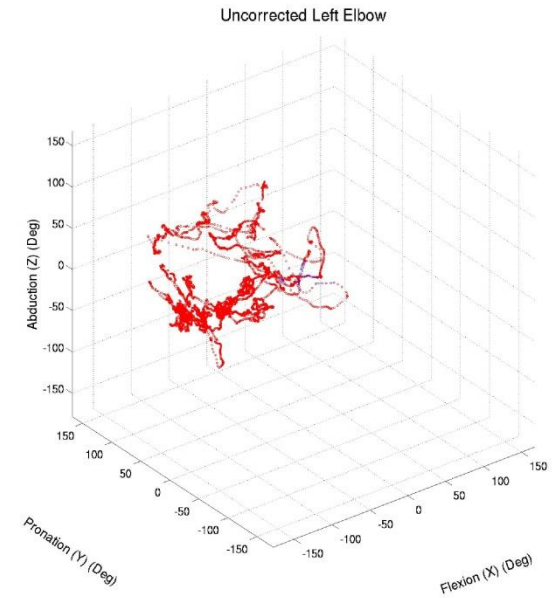
Uncorrected Left Elbow
Abduction (Z) (Deg)
Pronation (Y) (Deg)
Flexion (X) (Deg)

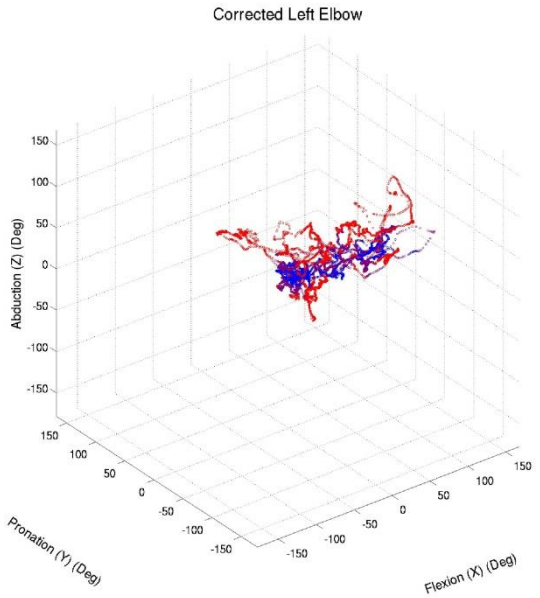
Corrected Left Elbow
Abduction (Z) (Deg)
Pronation (Y) (Deg)
Flexion (X) (Deg)

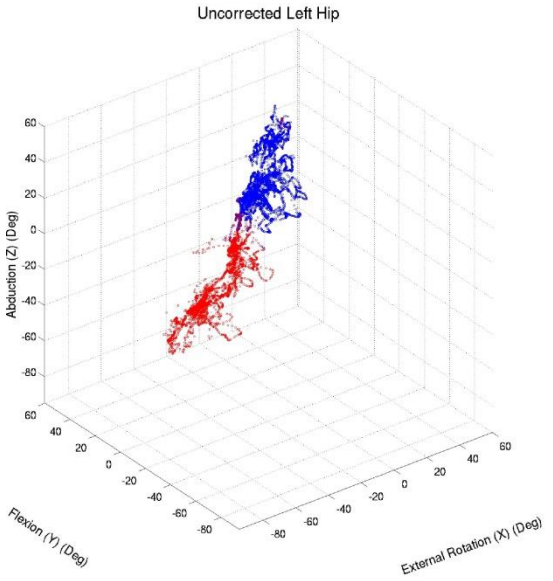
Uncorrected Left Hip
Abduction (Z) (Deg)
Flexion (Y) (Deg)
External Rotation (X) (Deg)

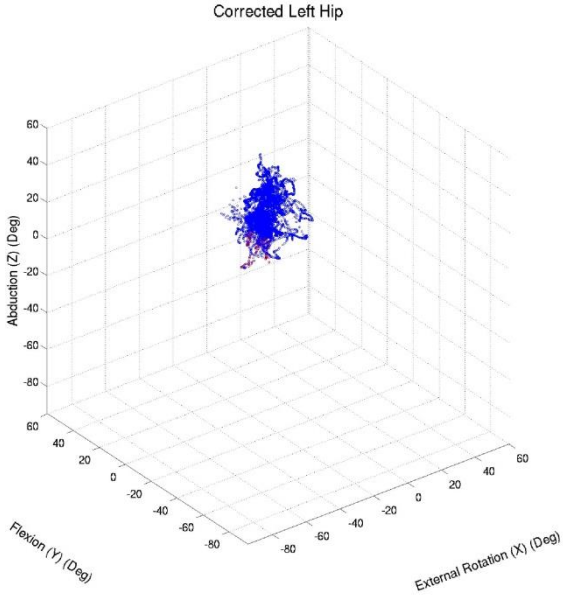
Corrected Left Hip
Abduction (Z) (Deg)
Flexion (Y) (Deg)
External Rotation (X) (Deg)

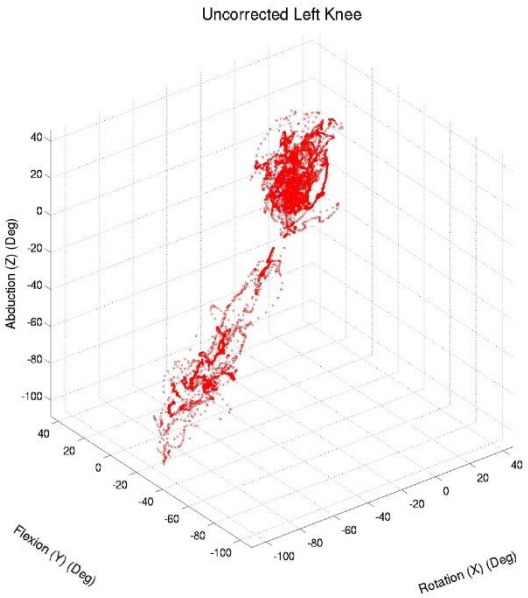
Uncorrected Left Knee
Abduction (Z) (Deg)
Flexion (Y) (Deg)
Rotation (X) (Deg)

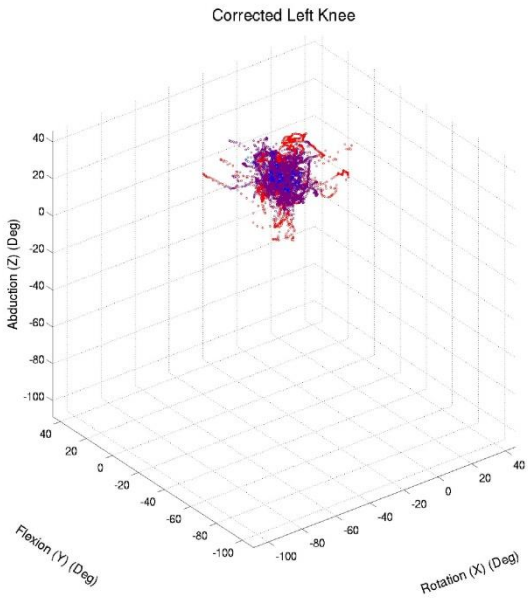
Corrected Left Knee
Abduction (Z) (Deg)
Flexion (Y) (Deg)
Rotation (X) (Deg)

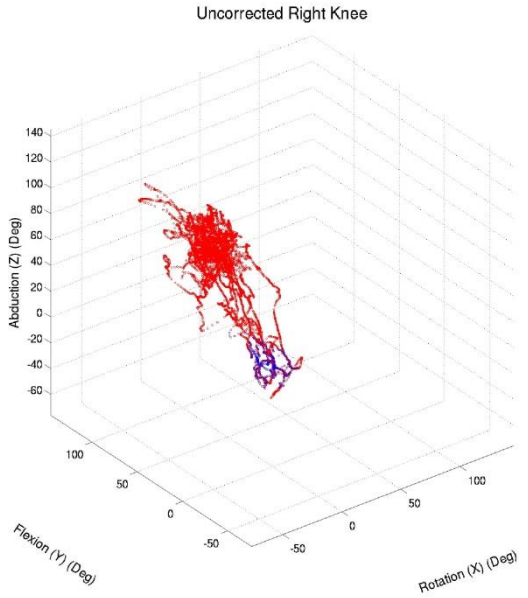
Uncorrected Right Knee
Abduction (Z) (Deg)
Flexion (Y) (Deg)
Rotation (X) (Deg)

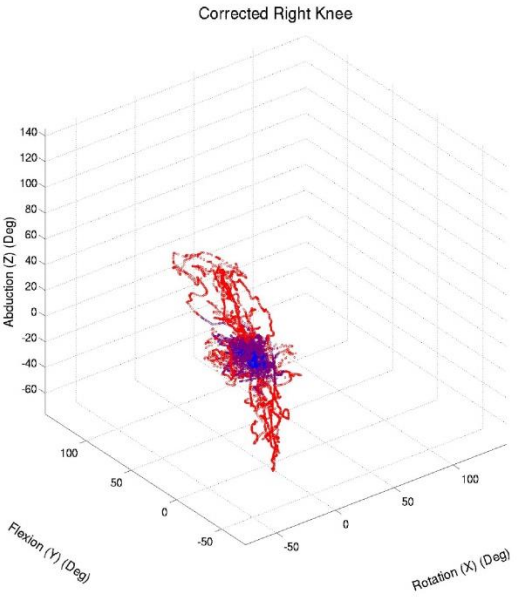
Corrected Right Knee
Abduction (Z) (Deg)
Flexion (Y) (Deg)
Rotation (X) (Deg)

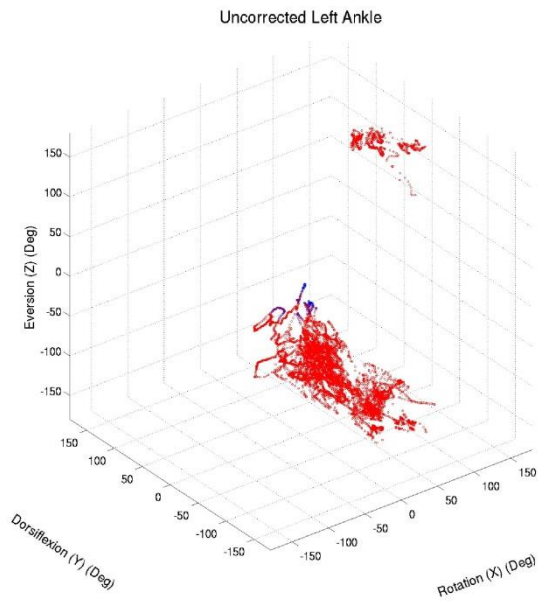
Uncorrected Left Ankle
Eversion (Z) (Deg)
Dorsiflexion (Y) (Deg)
Rotation (X) (Deg)

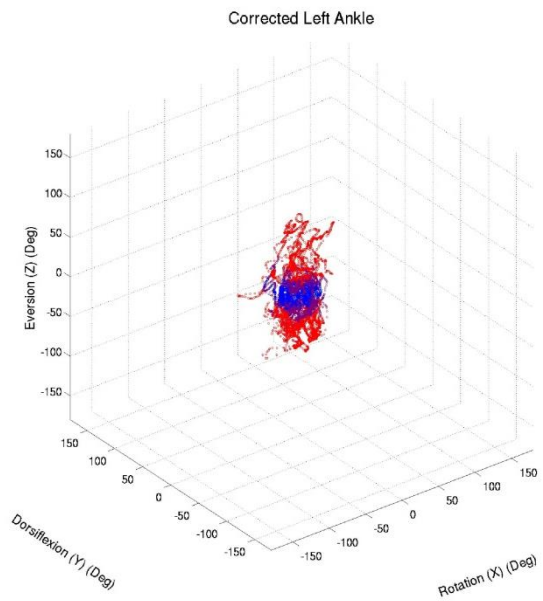
Corrected Left Ankle
Eversion (Z) (Deg)
Dorsiflexion (Y) (Deg)
Rotation (X) (Deg)

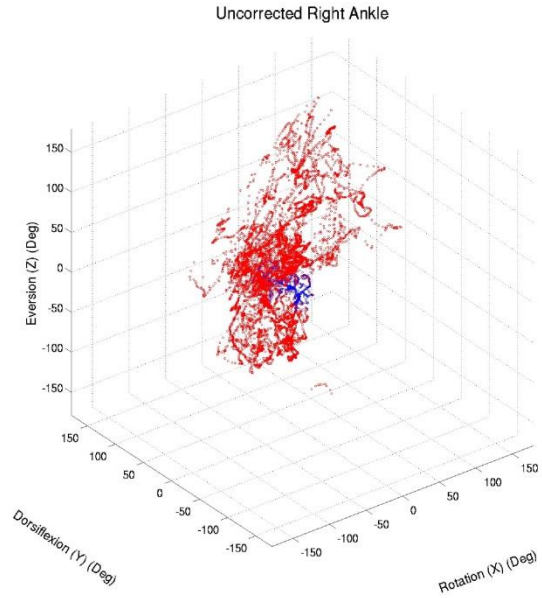
Uncorrected Right Ankle
Eversion (Z) (Deg)
Dorsiflexion (Y) (Deg)
Rotation (X) (Deg)

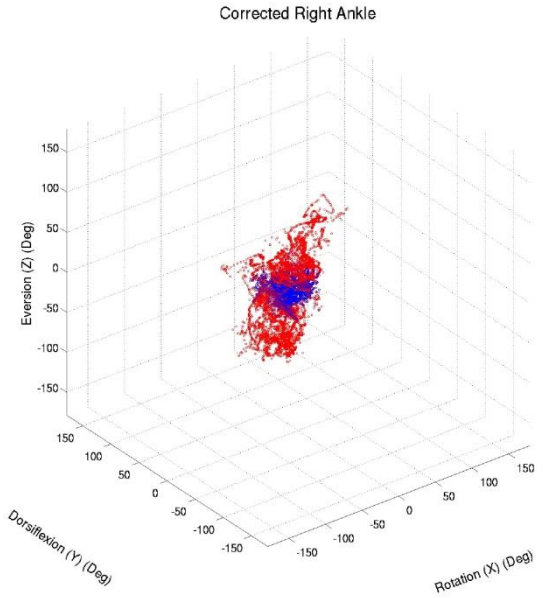
Corrected Right Ankle
Eversion (Z) (Deg)
Dorsiflexion (Y) (Deg)
Rotation (X) (Deg)

Appendix C: Joint Globographic Plots

Globographic plots of kinematic joint angle data for a single trial. Blue points are samples within joint limits. Purple indicates samples within 10 degrees of limits. Red indicates samples more than 10 degrees beyond limits. Yellow areas show joint limits. Grid lines are spaced at 5 and 2.5 degree intervals top to bottom and left to right respectively. These figures show position of a joint on the surface of the sphere relative to the preceding joint at the center of the sphere. Internal/external rotation of the preceding joint does not affect the position of the following joint on the sphere's surface, but is considered in determining the color of the points.

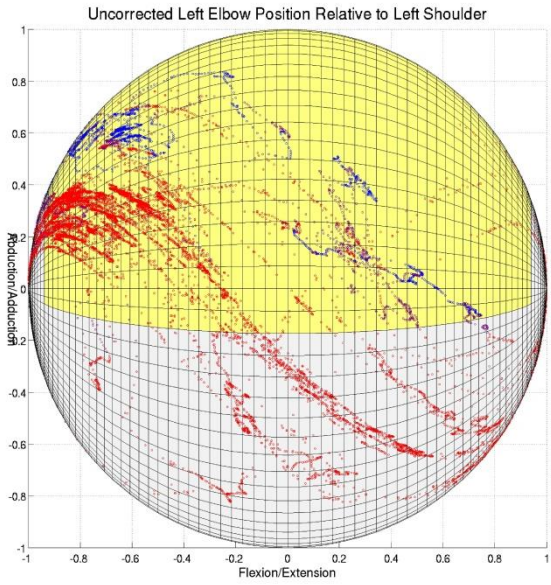
Uncorrected Left Elbow Position Relative to Left Shoulder
Abduction/Adduction
Flexion/Extension

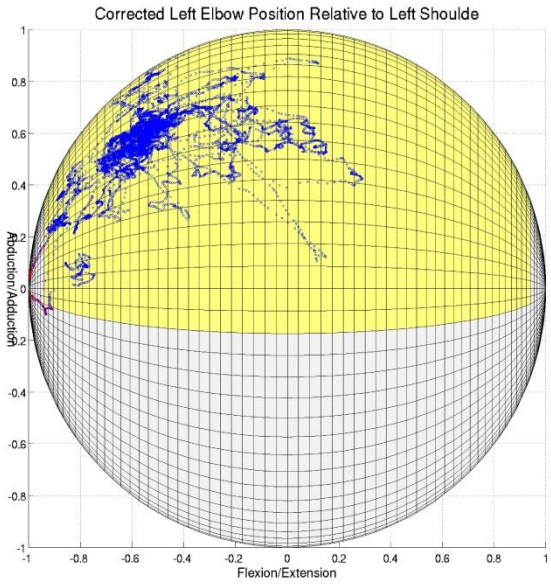
Corrected Left Elbow Position Relative to Left Shoulde
Abduction/Adduction
Flexion/Extension

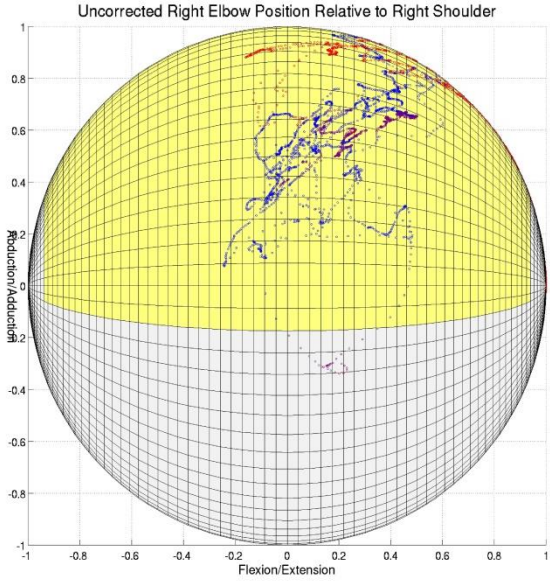
Uncorrected Right Elbow Position Relative to Right Shoulder
Abduction/Adduction
Flexion/Extension

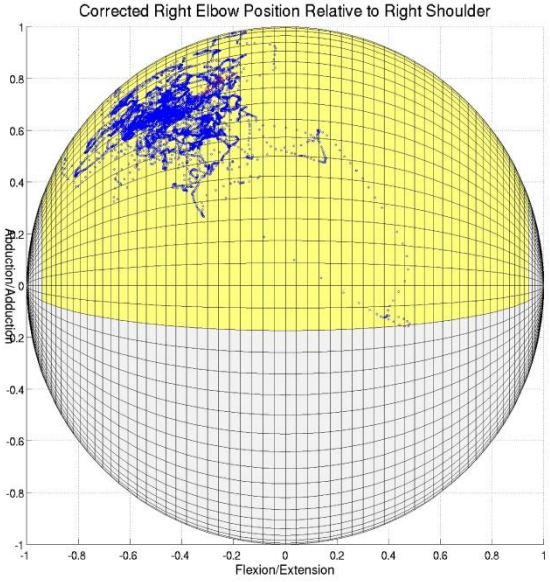
Corrected Right Elbow Position Relative to Right Shoulder
Abduction/Adduction
Flexion/Extension

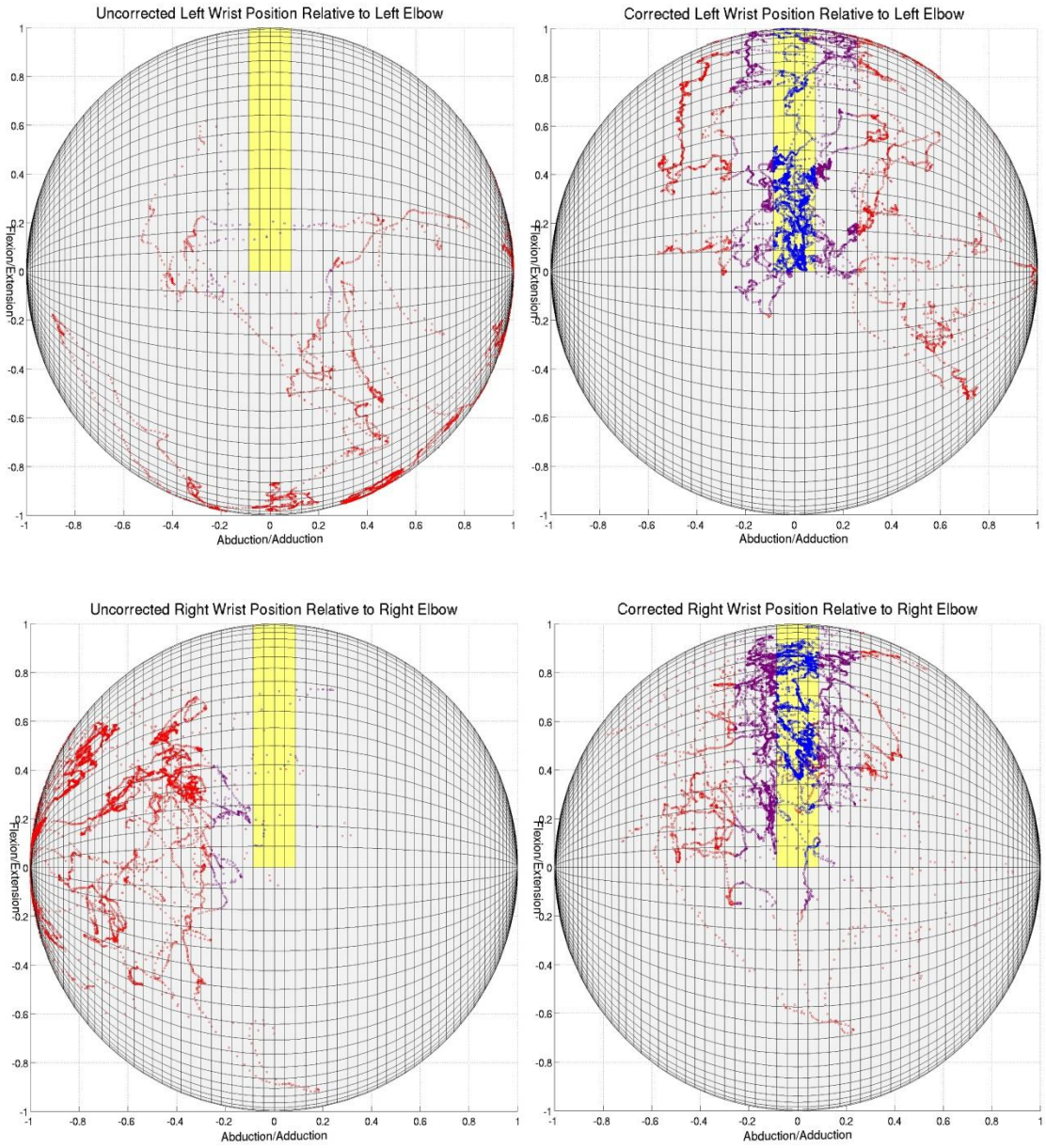
Uncorrected Left Wrist Position Relative to Left Elbow
Corrected Left Wrist Position Relative to Left Elbow
Uncorrected Right Wrist Position Relative to Right Elbow
Corrected Right Wrist Position Relative to Right Elbow
Flexion/Extension
Abduction/Adduction

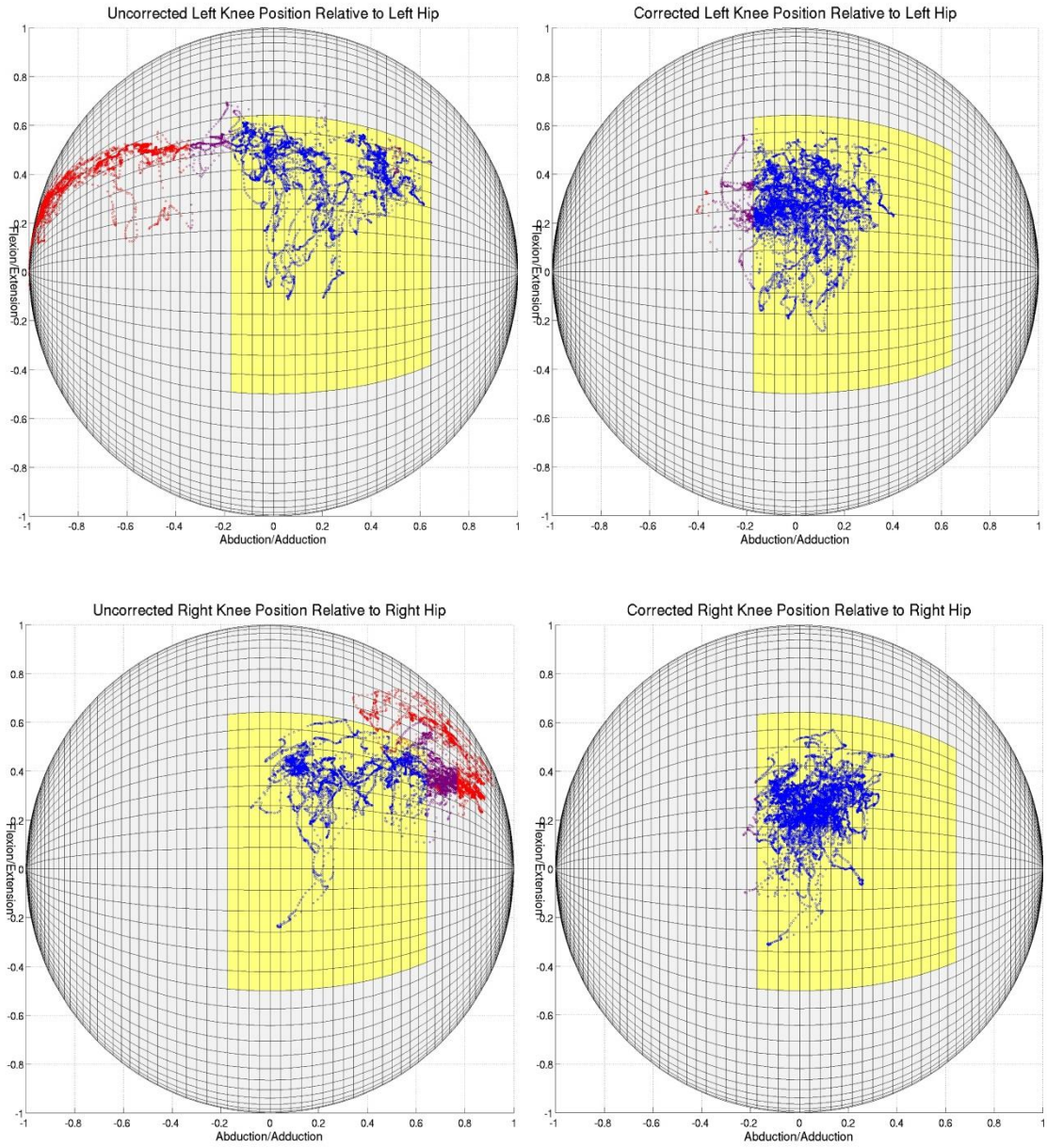
Uncorrected Left Knee Position Relative to Left Hip
Corrected Left Knee Position Relative to Left Hip
Uncorrected Right Knee Position Relative to Right Hip
Corrected Right Knee Position Relative to Right Hip
Flexion/Extension
Abduction/Adduction

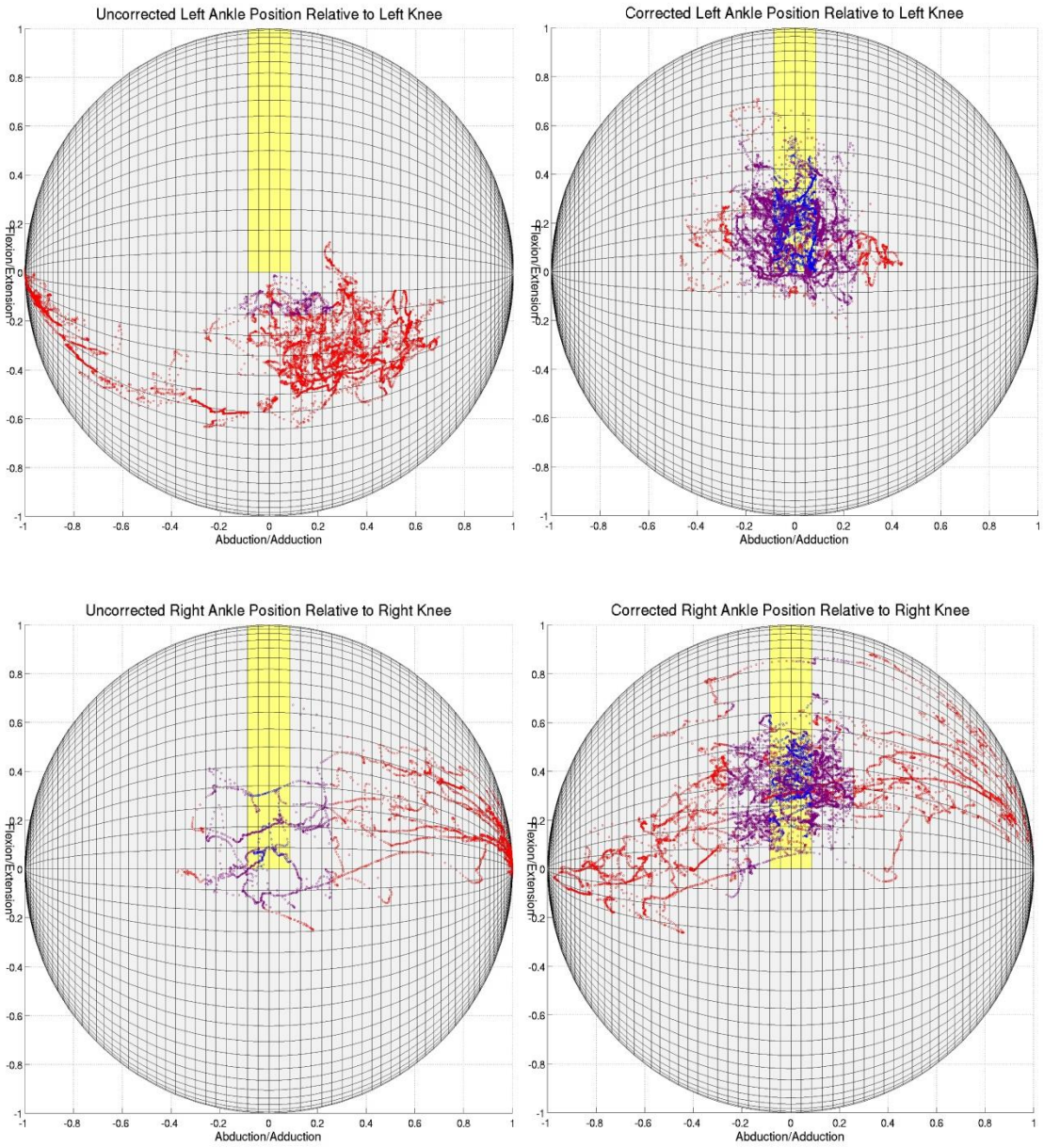
Uncorrected Left Ankle Position Relative to Left Knee
Corrected Left Ankle Position Relative to Left Knee
Uncorrected Right Ankle Position Relative to Right Knee
Corrected Right Ankle Position Relative to Right Knee
Flexion/Extension
Abduction/Adduction